The Casimir force and micro-electromechanical systems at submicron-scale separations

Broer, Wijnand

The Casimir Force and Micro-Electromechanical Systems at Submicron-scale Separations

Wijnand Broer

Zernike Institute PhD series 2014-23
ISSN: 1570-1530

ISBN: 978-90-367-7463-5 (printed version)
ISBN: 978-90-367-7464-2 (electronic version)

The work described in this thesis was performed at the Zernike Institute for Advanced Materials and the Center for Theoretical Physics of the Rijksuniversiteit Groningen.

Printed by Ipskamp Drukkers

rijksuniversiteit
groningen

The Casimir Force and Micro-Electromechanical Systems at Submicron-scale Separations

Proefschrift

ter verkrijging van de graad van doctor aan de
Rijksuniversiteit Groningen
op gezag van de
Rector Magnificus prof. dr. E. Sterken
en volgens besluit van het College voor Promoties.

De openbare verdediging zal plaatsvinden op

vrijdag 28 november 2014 om 11.00 uur

door

Wijnand Hendrik Broer

geboren op 7 oktober 1977
te Groningen

Promotores
Prof. dr. J. Knoester
Prof. dr. G. Palasantzas

Beoordelingscommissie
Prof. dr. ir. C. H. van der Wal
Prof. dr. H. A. de Raedt
Prof. dr. S. Scheel

Contents

Chapter 1

Introduction

1.1 Casimir-Lifshitz forces: some basic concepts

This section will present some of the basic ideas of what has become known as the Lifshitz theory of dispersion forces. This theory was developed in the 1950s [1] and 1960s [2] and later appeared in textbook form [3]. A more detailed chapter 2 is included to make this thesis a self contained document, readable by non experts. The results of the Lifshitz theory will be written in a convenient form for application of the theory.

The van der Waals force[1] between macroscopic bodies at nanometer separations and the Casimir force between parallel ideal metal plates at much larger separations, are intimately related. [1–8] According to the Lifshitz theory, both forces arise from fluctuating currents (or polarizations) at the surfaces of the macroscopic bodies. [1–23] This current gives rise to an electromagnetic field which interacts with the current at the surface of the other body. At short separations (<10 nm) the retardation of the electromagnetic field is negligible, which results in the van der Waals interaction. At large separations ($\gg$ 10 nm) retardation becomes significant, which results in a more general expression than the Casimir formula. The latter is reproduced in the limit of ideal metals.

1.1.1 Van der Waals forces

In 1873 J. D. van der Waals empirically introduced a weak attractive force between molecules in a gas to explain an observed deviation from the ideal gas law. [24] At the time the presence of such an attractive force could be understood in the case of polar molecules (i.e. molecules with a permanent dipole moment such as hydrogen or water vapor). After all, an opposite orientation of the dipole moments would be statistically favorable so that an electrostatic attraction could occur. However, gases of non polar molecules (e.g. helium) were observed to exhibit a similar deviation from the ideal gas law, which could not be explained in this way. The nature of this force remained unclear.

[1] In literature, the name "van der Waals force" can refer to several different things. In this thesis, it specifically refers to the van der Waals London dispersion force, which can occur both between individual polarizable particles and between surfaces.

This problem was resolved only in the 1930s by Fritz London [6, 25]. He showed that quantum mechanical uncertainty of the position and the momentum of the electrons in the gas gives rise to a temporary dipole moment in each molecule which consequently exerts an attractive electrostatic force on the other molecules. Let the distance between two dipoles be R, then the interaction potential V_{int} shows a power law dependence on R: $V_{int} \propto R^{-6}$. Such a potential can reproduce the deviation from the ideal gas law first observed by van der Waals. Such forces are sometimes called London dispersion forces or induced dipole forces.

The macroscopic equivalent of the intermolecular van der Waals force was first described by Hamaker [26] for two spherical bodies. He added the contributions of each individual force between two atoms and assumed that this would constitute the total macroscopic force. This approximation is called "pairwise summation". Later it was discovered that pairwise summation does not always produce the correct result for the macroscopic force, in other words, that dispersion forces are in general non-additive. However, the Lifshitz theory defines the conditions under which this is a valid first approximation [27]. The macroscopic van der Waals force (per unit area) between two parallel slabs was first obtained by de Boer [28]. It depends on the distance between the plates d as follows:

$$F_{vdW}(d) = \frac{A_H}{6\pi d^3}, \tag{1.1}$$

where the coefficient A_H denotes the so called Hamaker constant. This quantity was empirically determined to depend on the properties of the materials of the slabs. The Lifshitz theory [1–3] provides not only the conditions of validity of Eq. (1.1) but it also defines A_H in terms of permittivities of the materials.

1.1.2 Casimir Forces

In 1948 Casimir [4] showed that two perfectly reflecting parallel plates without electric charges attract each other. This force per unit area A depends on the distance between the plates d as follows:

$$\frac{F_{Cas}}{A}(d) = \frac{\pi^2 \hbar c}{240 d^4}. \tag{1.2}$$

This is the famous Casimir formula. One of its peculiarities is that this force depends only on d and the constants $\hbar$ and c.

This type of attraction is attributed to quantum mechanical fluctuations of the electromagnetic (EM) fields in vacuum. The average of the EM fields with respect to these fluctuations is zero, but the standard deviation (the uncertainty) is not. This fact gives rise to a nonzero electromagnetic energy in vacuum called zero point energy (ZPE). This name refers to the fact that it persists even at zero Kelvin. Each EM mode (photon) with frequency ω carries a ZPE of $\hbar\omega/2$. The parallel plates impose boundary conditions on

the EM fields between them: at the position of the plates the values of the fields must be zero. This ensures that only modes with certain frequency are allowed to exist inside the cavity formed by the plates. However, no such restriction applies to the modes outside the cavity. This gives rise to a net attractive force between the plates. So the Casimir energy is the difference between ZPEs of EM modes due to the presence of boundaries.

This ZPE interpretation is the most common way among physicists to describe the Casimir force; it is typically introduced in text books in this way. (See e.g. [29] or [30]). However, the popularity of the ZPE approach ensured that the context in which the result Eq. (1.2) came about is known primarily among experts. In the same year, 1948, Casimir and Polder published a paper [31] in which they calculated the effect of retardation on van der Waals- London forces between induced dipoles. Instead of the usual R^{-6} law they found that in the retarded (long distance) limit the interaction potential decreases one power faster, $V_{int} \propto R^{-7}$. Casimir knew [4] that in this long distance limit, the macroscopic equivalent of this force as a function of the distance should be given by Eq. (1.2). Later Lifshitz clarified this issue by showing that the van der Waals and Casimir forces are respectively the short and long distance limits of the same force [1–3].

1.2 Measuring the Casimir force

The first attempt to directly measure the Casimir force was performed in the 1950s by Marcus Sparnaay [32]. Two parallel metal plates were brought in contact after each measurement to prevent any inadvertent electrostatic contribution from becoming too large. Despite of this, the experimental uncertainty was so large that the resulting Casimir force was neither significantly different from zero nor did it contradict Eq. (1.2). Later, in the 1970s, an experiment involving metal test bodies was similarly inconclusive [33].

It was not until 1997 that Steve Lamoreaux performed the first direct high accuracy measurements of the Casimir force using a torsion pendulum [34]. A major source of uncertainty in e.g. Sparnaay's experiment was the impossibility of keeping two plates parallel at nanometer to micrometer separations. A workaround for this problem is to use a plane-sphere setup, in which the radius of the sphere is much larger than the typical separation distance. In such a case, the curvature of the sphere can be considered gentle enough to be approximated adiabatically: each surface segment dA of the curved body - in this case a sphere - is approximated by a parallel plate configuration, and the contribution of each segment is added to the total force. (See Fig. 1.2). This approximation is called "proximity force approximation" (PFA). In particular, the Casimir force between an ideal metal plate and a sufficiently large ideal metal sphere with radius R is:

$$F_{PS}(d) \approx -2\pi R \frac{E_{pp}}{A}(d) = \frac{\pi^3 \hbar c R}{360 d^3}, \qquad R \gg d \tag{1.3}$$

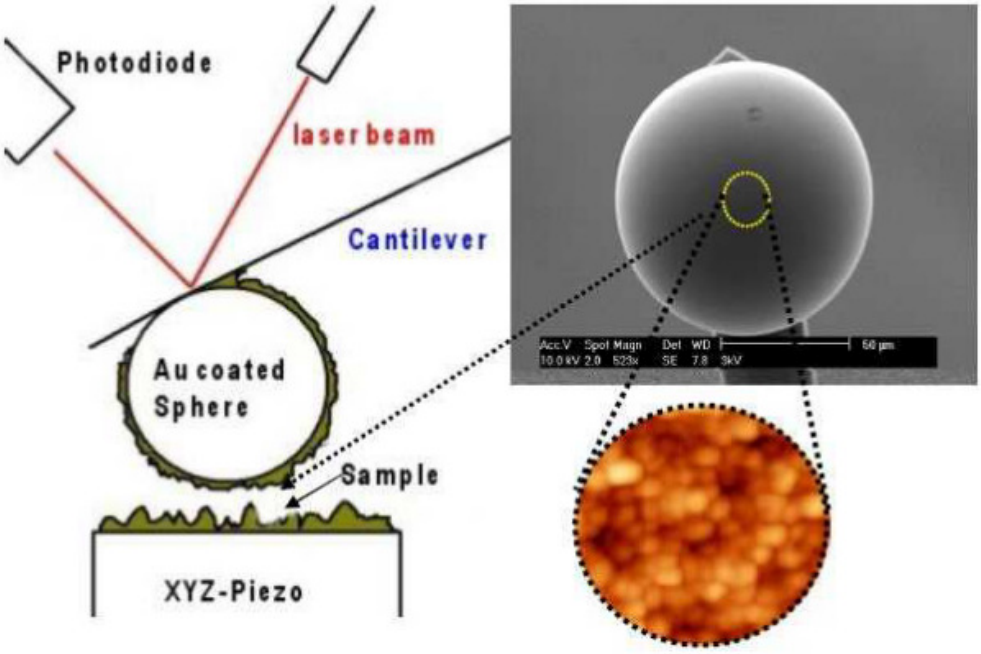

Figure 1.1: *Sketch of an atomic force microscope (AFM)setup*

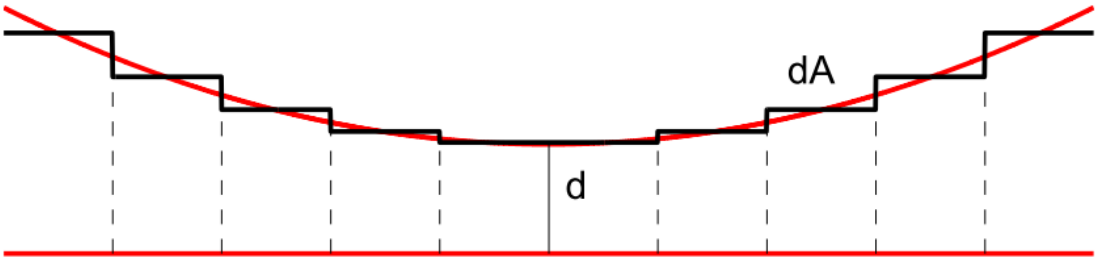

Figure 1.2: *Sketch of the application of the PFA in a plane-sphere geometry.*

where d is the distance of closest approach between the plate and the sphere and E_{pp} denotes the Casimir energy per unity area in a parallel plate setup. Presently experiments are typically performed in such a geometry. One attempt to utilize a parallel plate setup resulted in an uncertainty of about 15 %. [23] Other configurations were also investigated, e.g. crossed cylinders. [35]

One can distinguish between static and dynamic setups to measure the Casimir force. An example of a static setup is a technique called atomic force microscopy (AFM) which was introduced soon after Lamoreaux'experiment [36]. In a static AFM a (large) sphere is rigidly attached to a cantilever. This sphere is brought into proximity to a plate (substrate). The resulting surface force deflects the cantilever by a certain amount. (See fig. 1.1). From

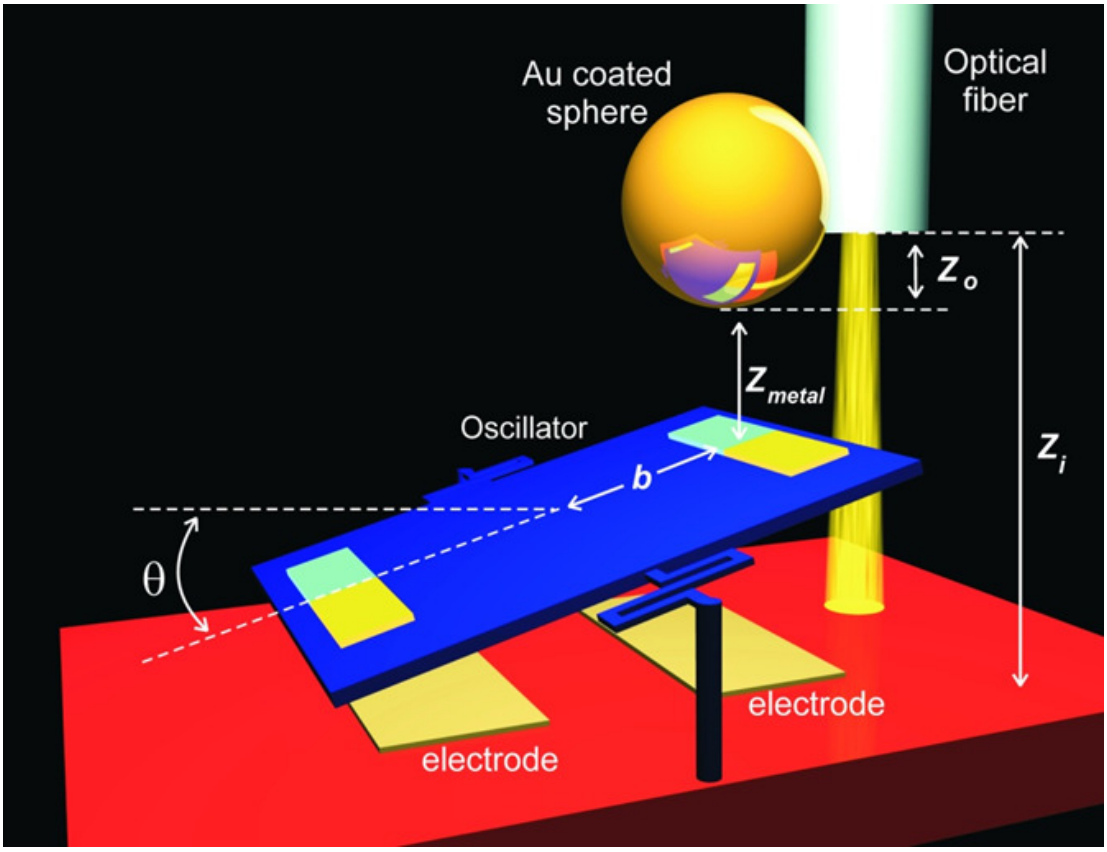

Figure 1.3: *Sketch of a dynamic micromechanical (MEMS) oscillator setup. Image courtesy of R. S. Decca.*

this deflection and Hooke's law the total surface force can be reproduced. This surface force is not equal to the Casimir force: due to charge accumulation there is always a nonzero electrostatic contribution which must be compensated with a reverse bias, even if both surfaces are grounded. In a dynamic setup, one of the surfaces remains immobile whereas the other one moves by means of a seesaw like structure which oscillates around its pivot point. (See Fig. 1.3). Below this seesaw structure some electrodes excite the oscillation and compensate the gravitational force. In this type of setup the frequency of rotation ω_r is shifted compared to the system's natural frequency ω_0. The frequency ω_r is directly determined during the movement using a laser. The frequency shift is related to the Casimir force as follows [37]:

$$\omega_r^2 - \omega_0^2 = \frac{b^2}{I}\frac{\partial F_{Cas}}{\partial z}(z) \tag{1.4}$$

where b is half the length of the seesaw and I denotes the moment of inertia of the system. It is assumed that the oscillator is near a stable fixed point z, near enough for the Casimir force to be approximated linearly, as a first order expansion in the coordinate θ. This assumption is valid at distances of several hundred nm up to a few microns. However, it

will be broken at distances below 100 nm, where the Casimir force extends the amplitude of the oscillator to the nonlinear regime. [38] So in a dynamic setup the derivative of the Casimir force is measured rather than the force itself. In addition a plane-sphere setup is typically used also in this case, which means that typically the pressure (per unit surface) is plotted instead: $F'_{Cas}(z) \approx 2\pi R P_{Cas}(z)$.

1.3 Why investigate Casimir forces?

1.3.1 Fundamental motivations

Since the Casimir force ultimately stems from quantum mechanical uncertainty, it will always contribute to the total force between two surfaces. It becomes particularly significant in ranges of tens of nanometer up to several microns. Therefore it must be accounted for in micron range gravitation measurements, where the Casimir force actually typically dominates the gravitational force. In such Cavendish like experiments it is hoped that a significant deviation from the expected Newtonian gravitation will be observed. This is because of predictions of hypothetical new forces beyond those of the standard model of elementary particles. [17] In section 1.2 it was mentioned that charge accumulation forces experimentalists to compensate this electrostatic force with a reverse bias. However, recently it was pointed out [39] that this is usually not enough, since a real surface is typically not an equipotential plane (e.g. due to the polycrystalline nature of materials). This gives rise to an additional electrostatic contribution known as electrostatic patch potentials. This contribution must also be taken into account in order to obtain conclusive experimental results regarding hypothetical new forces.

Additionally, the ZPE interpretation of the Casimir force plays a role in the discussion about the cosmological constant. [40] The Casimir force is considered a directly observable manifestation of the ZPE. Naively extending this argument to cosmological scales results in a discrepancy with the measured value of the cosmological constant of 120 orders of magnitude. However, Quantum electrodynamics is a gauge invariant theory, which means that it calculates only *differences* between energies, in this case ZPEs. As a side note: Casimir forces can be theoretically described without referring to the ZPE [41]. Hence experimental observation of the Casimir force does not establish the "reality" of vacuum fluctuations [42]. On the other hand, how the value of the cosmological constant can be theoretically reproduced and the role of the electromagnetic ZPE in this, is an open problem that is still under investigation. [13]

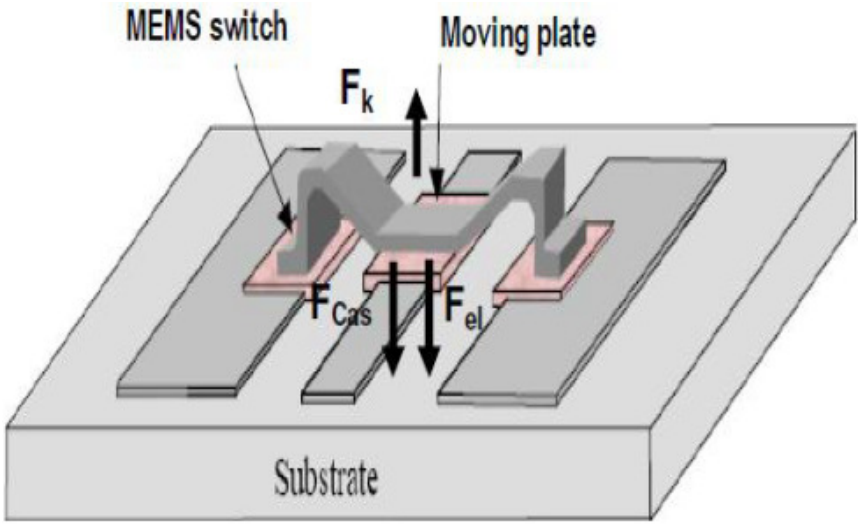

Figure 1.4: *Schematic picture of a micromechanical (MEM) switch. If the electrostatic and Casimir forces (F_{Cas} and F_{el}, respectively) exceed the elastic force F_k, the moving plate will get stuck to the substrate and the plate can no longer move up. This is called stiction.*

1.3.2 Practical motivations

An important practical reason to study Casimir interactions is their role in so called micro and nano electromechanical systems (MEMS/NEMS). These are devices with moving components that operate at the nanometer to micron scales. Note that the term "MEMS/NEMS" does not indicate any particular functionality; this ranges from (micro) switches to accelarometers and cantilevers. (See Fig. 1.5) This thesis specifically concerns the dynamics of these moving parts, which are subject to several different forces including the Casimir force. This type of dynamics is called the actuation dynamics.

The small scales at which Micro electromechanical engineering is now conducted have revitalized interest in the Casimir force. Devices such as vibration sensors and switches are made with parts that are just a few micrometers in size. This is the right size for the Casimir force to play a role: the surface areas are large enough, but the gaps are small enough for the force to draw components together and lock them tight. [43] This effect is called stiction. Permanent adhesion is a common cause of malfunction in MEMS devices. Casimir forces, in synergy with electrostatic actuating forces, can further augment this phenomenon. [44–60] Additionally, as the development of MEMS evolves toward nano electromechanical systems, attention will also be drawn to scaling issues. It is inevitable that the Casimir interactions between metallic and/or dielectric surfaces in nanometer proximity of each other will occur, and stiction phenomena require specific attention.

The Casimir force is responsible for stiction in dry conditions. [51] After all, capillary and hydrodynamic forces are absent in such circumstances. Therefore the Casimir

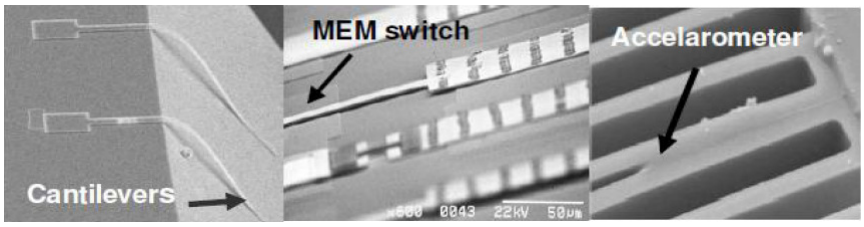

Figure 1.5: *Examples of Micromechanical systems (MEMS), where stiction can occur as the arrows indicate.*

force profoundly influences the actuation dynamics. It supplements the electrostatic force in countering the elastic restoring force to determine the beam's actuation behavior, for example in microswitches. The latter is typically constructed from two conducting electrodes one of which is fixed and the other is suspended by a mechanical spring governed by Hooke's law. [61]

On the other hand, the irreversible adhesion of moving parts resulting from Casimir and electrostatic forces, [44–60] can also be exploited to add new functionalities to micromechanical architectures. Depending on the application the Casimir force can actually be beneficial: in some cases the attraction between the surfaces is a desirable effect. Examples include direct bonding [62] and the creation of an artificial gecko. [63] In such applications the distance between surfaces is typically of the order of 10 nm, i.e. well in the van der Waals regime, where the capillary force is also expected to contribute considerably in wet environments.

1.4 Aim and Outline of the thesis

1.4.1 The Casimir force, surface roughness and MEMS

In an experiment, the Casimir formula Eq. (1.2), including its plane-sphere equivalent Eq. (1.3), fails in several respects: Firstly, there is no such thing as perfect reflectors, (i.e. a material with infinite permittivity at all frequencies). This idealization is valid only in the case of metallic surfaces at separations of several microns, which can be demonstrated as a limiting case of the Lifshitz formula. Secondly, Eq. (1.2) ignores the temperature dependence. This is also accounted for by the Lifshitz formula: it turns out thermal modes contribute significantly only at separations comparable to the thermal wavelength, which at room temperature is about 7 μm. In general, there is a correlation between the effects of the temperature and that of the optical response, e.g. the permittivity can depend on temperature. An example of that can be found in Ref. [64].

This thesis aims at describing the Casimir force at separations below 100 nm, where it is expected to be large enough to have some practical relevance for MEMS applications.

This brings us to the third reason the Casimir formula is not applicable in an experiment: real surfaces are often rough. This means that there is incomplete information about the distance between the bodies. Such deviations from the ideal plane-sphere geometry are typically a few nm in height, i.e. the root-mean-square (rms) roughness $w \sim 1$ nm. However they can affect the Casimir force at separations of up to 100 nm. Unlike the other two effects, this is *not* accounted for by the Lifshitz theory.

Advances made in the measurement and theoretical understanding of Casimir forces over the last 10 years allow today a more detailed study of MEMS made from real material surfaces. [65] In particular, a realistic way to include the effect of surface roughness on Casimir and electrostatic forces enables a careful analysis of stiction in MEM systems at separations where the Casimir force can become appreciable. Note that although electrostatic forces can be switched off if no potential is applied, Casimir forces will always be present and will influence the actuation dynamics. This is because the Casimir force stems from quantum mechanical uncertainty, a fundamental property of nature which cannot be shut down at our convenience. With the exception of a few cases, [58, 66] it is in general impossible to assign a continuous parameter to the Casimir force.

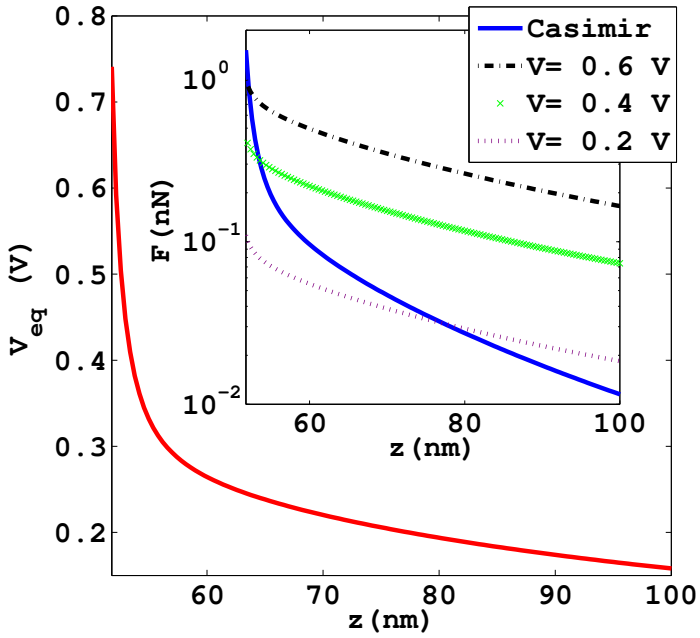

Figure 1.6: *The main panel shows the voltage to which the Casimir force corresponds at distances below 100 nm. This was done for a rough gold surface. In the inset the Casimir force is compared to the electrostatic force for different values of the applied voltage.*

Whether the Casimir force can exceed the electrostatic force at separations below 100 nm depends on the applied voltage between the two surfaces. Equating Casimir and

electrostatic forces produces a function of distance. This function is the square of the voltage to which the Casimir force corresponds: $V_{eq}(z) = \sqrt{F_{Cas}(z)/F_{V=1V}(z)}$, where $F_{V=1V}(z)$ denotes the electrostatic force for a voltage of 1 V. This equivalent voltage has been plotted as function of distance for a rough gold surface in Fig. 1.6. It turns out that V_{eq} varies between 0.2 V and 0.6 V in this case. This will be discussed in detail in chapter 4.

1.4.2 Outline

The Lifshitz formula is an important basic result that deserves to be presented in more detail. This will be done in chapter 2.

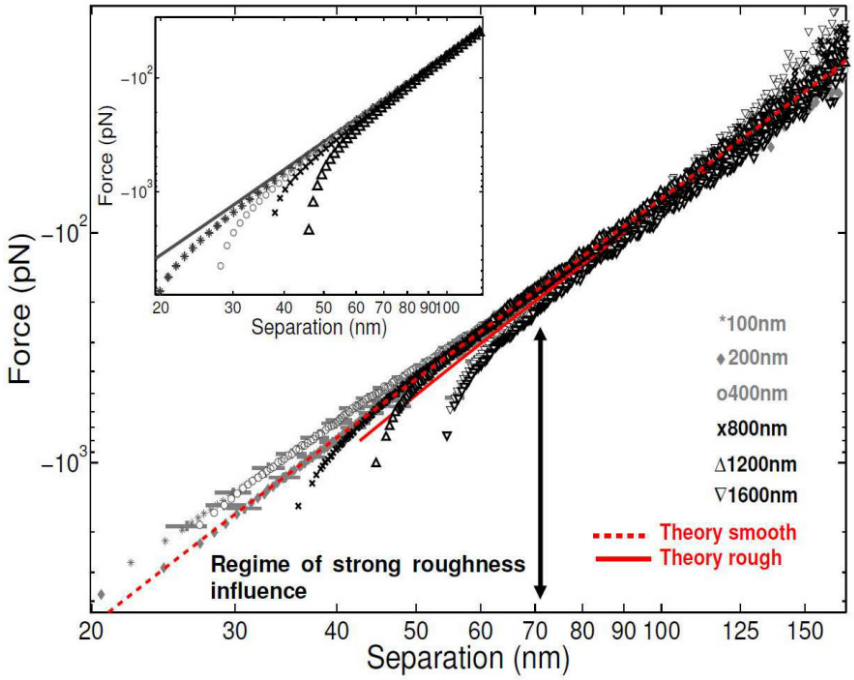

Figure 1.7: *Measurements of the Casimir force between gold samples with varying degrees of roughness, associated with their thicknesses, indicated in nm. This picture appeared earlier in Ref. [67]. The dashed theoretical curve is based on Refs. [1, 2], and the solid one is based on Refs. [68, 69].*

One way to theoretically describe the effect of surface roughness on the Casimir force is an expansion for "weakly rough" surfaces: [68, 69] this assumes that deviations from an ideal geometry are small on the scale of the separation distance; it is an expansion of w/d. This is a very useful approximation since not only is it easy to estimate, but also it relies only on the assumption of the ratio w/d being small. It takes the non-additive nature of the Casimir force into account, and it does not have to rely on a pairwise additive summation

by taking the statistical average. However, by itself it has turned out to be insufficient to reproduce experimental data. [67] At separations below 70 nm the experimental data significantly deviate from the results of this approximation. (See Fig. 1.7). Chapter 3 presents a simple model to solve this discrepancy. This model is based on a statistical analysis of AFM topography data.

The rest of the thesis concerns the Casimir force for MEMS applications. Chapter 4 presents a bifurcation analysis for MEMS actuated by both electrostatic and Casimir forces in the case of a conservative system. This means that roughness must be taken into account for the electrostatic force as well. The applied voltage between the surfaces is a continuous parameter, whereas the dependence on roughness is discrete. The reason for the latter is that there is information about only a limited number of samples. In chapter 5 this will be generalized to the non-conservative case, where energy loss and gain are allowed through damping and driving, respectively. Since this forcing constitutes explicit time dependence it will introduce another degree of freedom to the system. Such a system, while still relatively simple, is complicated enough to become chaotic for certain parameter values. Roughness is again treated as a discrete parameter in this case.

Chapter 2
Introduction to the Lifshitz theory

The Lifshitz theory of dispersive forces between macroscopic bodies [1] was based on Rytov's theory on fluctuating EM fields [70]. This theory is valid for arbitrary macroscopic bodies regardless of their chemical composition. It includes retardation effects and its only limitation is that the distances between the bodies must be much larger than the interatomic distances. A notable property is that it expresses the force in terms of the macroscopic dielectric functions of the bodies. A different approach based on the thermal Green function tensor [2] appeared later in textbook form [3].

The Lifshitz theory can be applied to bodies of any shape. However it can produce a closed analytical expression for the dispersion forces only in the case of parallel plates. This is the main limitation of the Lifshitz formula, which has only recently been overcome by the development of a numerical procedure. [71]

2.1 A macroscopic approach

It is not possible to derive the the Casimir force starting from interactions between individual polarizable particles. Approximations like pairwise additive summation are valid for tenuous bodies such as gases. In a condensed body, the atoms significantly affect each others' electronic shells, and the presence of a medium between the atoms gives rise to a change in the electromagnetic field through which this interaction is established. [2] This non-additivity not only occurs for dispersion forces. For example, if charges can redistribute in response to the applied electric field, the electrostatic interaction can also demonstrate non-additive properties.

So rather than a "microscopic" description a macroscopic viewpoint is preferred, in which the bodies are considered continuous media. This is a valid assumption as long as the distance between the bodies is much larger than the typical distances between atoms.

The basic idea of the theory is that the interaction between the bodies is carried by a fluctuating electromagnetic field. Such fields are always present inside the bodies, and they can extend beyond the boundaries of the materials. An obvious example would be thermal radiation, but it should be kept in mind that electromagnetic fluctuations persist even at zero Kelvin as purely quantum zero point fluctuations. The source of

these fluctuations is the electric polarization $\mathbf{P}(\omega, \mathbf{r})$ or equivalently the electric current density $\mathbf{J}(\omega, \mathbf{r}) = -i\omega\mathbf{P}(\omega, \mathbf{r})$, where a temporal Fourier transform has been performed. The presence of these fluctuations is easiest to understand in the case of metallic surfaces. The density of the "free" electrons fluctuates as the density of any gas. A point $\mathbf{r}$ where the density of electrons is smaller than that of its surrounding will attract electrons - and hence give rise to a current - to increase the density at $\mathbf{r}$.

2.2 The Fluctuation-dissipation Theorem

The Fluctuation dissipation theorem [70, 72, 73] (FDT) relates the correlations of the fluctuating currents to the dissipation in the medium as follows:

$$\left\langle J_\alpha(\omega, \mathbf{r}) J^*_\beta(\omega', \mathbf{r}') \right\rangle = \omega \mathrm{Im}[\varepsilon(\omega)] \left(\frac{\hbar\omega}{2} + \frac{\hbar\omega}{e^{\hbar\omega/k_bT} - 1} \right) \delta(\omega - \omega')\delta(\mathbf{r} - \mathbf{r}')\delta_{\alpha\beta}, \tag{2.1}$$

where $\alpha, \beta = x, y, z$ denote the vector components. The imaginary part of the permittivity $\varepsilon(\omega)$ is associated with the dissipation of the EM fields in the interacting bodies. Note that if $\mathrm{Im}\varepsilon(\omega) = 0$ the fluctuations will be uncorrelated and the variance with respect to these fluctuations will be zero. The existence of this current requires energy, which is "borrowed" - or rather dissipated - from the (fluctuating charges in the) medium. The existence of the dispersion forces arising from these fluctuations is therefore closely related to this dissipation. The relation (2.1) is valid in thermal equilibrium. A description of dispersion forces for systems out of thermal equilibrium has been established only recently. [74] Some more information about the FDT can be found in Refs. [75, 76].

The first and second term on the right hand side of Eq. (2.1) represent ZPE and thermal contributions, respectively. The fluctuating currents are sources of EM fields, which are solutions of Maxwell's equations. It is convenient to represent these solutions in terms of the so called Green function tensor (GFT). The electric field components $E_\alpha(\omega, \mathbf{r})$ are

$$E_\alpha(\omega, \mathbf{r}) = \frac{i}{\omega} \int d\mathbf{r}' G_{\alpha\beta}(\omega, \mathbf{r}, \mathbf{r}') J_\beta(\omega, \mathbf{r}), \tag{2.2}$$

where $G_{\alpha\beta}$ denotes the components of the GFT. The GFT fulfills the role of the response in linear response theory. [73]

Combining the relations (2.1), (2.2) with some general properties of the GFT [3] yields the following expression for the correlation function of the electric field:

$$\left\langle E_\alpha(\omega, \mathbf{r}) E^*_\beta(\omega', \mathbf{r}') \right\rangle = \coth\left(\frac{\hbar\omega}{k_bT} \right) \mathrm{Im} G_{\alpha\beta}(\omega, \mathbf{r}, \mathbf{r}')\delta(\omega - \omega') \tag{2.3}$$

The electric field is related to the magnetic field through Maxwell's equations, which allows a similar correlator to be derived for the magnetic field components $H_\alpha(\omega, \mathbf{r})$. By the same

token it follows that the components of the electric and magnetic fields are not correlated to each other: [3] $\left\langle E_\alpha(\omega,\mathbf{r})H^*_\beta(\omega',\mathbf{r}')\right\rangle = 0$.

The Green function tensor is the solution of the Maxwell equations for a point charge:

$$\left[\partial_\alpha\partial_\beta - \delta_{\alpha\beta}\left(\nabla^2 + \tfrac{\omega^2}{c^2}\varepsilon(\omega,\mathbf{r})\right)\right]G_{\alpha\beta}(\omega,\mathbf{r},\mathbf{r}') = 4\pi\tfrac{\omega^2}{c^2}\delta_{\alpha\beta}\delta(\mathbf{r}-\mathbf{r}') \tag{2.4}$$

where $\varepsilon(\omega,\mathbf{r})$ is the inhomogeneous dielectric function of the interacting bodies. The quantity $G_{\alpha\beta}$ contains information about the interaction of the EM fields with the bodies. Its real part diverges at $\mathbf{r}=\mathbf{r}'$ since this equates the location of the point charge to that of the observer. Its imaginary part, however, does not diverge at $\mathbf{r}=\mathbf{r}'$: this quantity represents the local density of states (LDOS) which is related to spontaneous emission phenomena. For example, for a point dipole in vacuum $\mathrm{Im}[G_{\alpha\beta}(\mathbf{r}=\mathbf{r}',\omega)]\propto\omega^3$ which is proportional to the Einstein A coefficient. Equation (2.4) must be solved taking the proper boundary conditions into account. The GFT components $G_{\alpha\beta}(\omega,\mathbf{r},\mathbf{r}')$ must meet the same boundary conditions as the electric field components $E_\alpha(\omega,\mathbf{r})$.

2.3 The Maxwell Stress Tensor

Now that the correlation functions of the components of the EM fields have been established via the fluctuation-dissipation theorem, another quantity must be introduced to relate the EM fields to a force they induce on a medium. This quantity is known as the Maxwell stress tensor (MST), sometimes also referred to as electromagnetic energy-momentum tensor. There are several ways to define this quantity, each stemming from different physical approaches. (See Ref. [77] an overview.) The form of the MST discussed here is known in literature as the Minkowski version.

This form of the Maxwell stress tensor can be derived from an expression for a point charge subjected to an external electric and magnetic field. [78] An electric and a magnetic contribution can be distinguished:

$$T_{\alpha\beta}(\mathbf{r},t) = \varepsilon_0 M^E_{\alpha\beta}(\mathbf{r},t) + M^H_{\alpha\beta}(\mathbf{r},t), \tag{2.5}$$

where

$$M^E_{\alpha\beta}(\mathbf{r},t) = \tfrac{1}{4\pi}[E_\alpha(\mathbf{r},t)E_\beta(\mathbf{r},t) - \delta_{\alpha\beta}\mathbf{E}^2]. \tag{2.6}$$

The magnetic contribution $M^H_{\alpha\beta}(\mathbf{r},t)$ can be obtained by replacing E by H in Eq. (2.6).

To obtain the Casimir-Lifshitz force the tensor (2.5) must be averaged with respect the fluctuations that give rise to the force. These averages of quadratic combinations of the EM field components can be expressed in terms of their correlation functions. In this way, the averaged tensor $< T_{\alpha\beta}(\mathbf{r},t) >$ can be obtained via the GFT at $\mathbf{r}=\mathbf{r}'$, where the GFT is singular. This singularity is associated with EM fields of short wavelength for which the

theory is invalid. The singular contribution at $\mathbf{r}$ can be excluded by subtracting the stress tensor for a homogeneous medium with $\varepsilon = \varepsilon(\mathbf{r})$ in this point. The GFT at $\mathbf{r} = \mathbf{r}'$ should be understood as

$$G_{\alpha\beta}(\omega, \mathbf{r}, \mathbf{r}) = \lim_{\mathbf{r}\to\mathbf{r}'}[G_{\alpha\beta}(\omega, \mathbf{r}, \mathbf{r}') - \widehat{G}_{\alpha\beta}(\omega, \mathbf{r}, \mathbf{r}')] \tag{2.7}$$

where $\widehat{G}_{\alpha\beta}(\omega, \mathbf{r}, \mathbf{r}')$ denotes the GFT for a homogeneous medium with $\varepsilon = \varepsilon(\mathbf{r})$. Indeed, as mentioned before, the correlation function Eq. (2.3) is regular at $\mathbf{r} = \mathbf{r}'$ as it should be.

A complication arises in the case where the bodies are immersed in a liquid. This is because there is no general expression for the stress tensor for a nonstationary EM field in an absorptive medium. This case has been analyzed in detail in Refs. [2, 3]. It was shown that the forces corresponding to long wavelength fluctuations can be obtained from an effective stress tensor which is identical to $T_{\alpha\beta}(\mathbf{r}, t)$ in Eq. (2.5), where ε_0 should be replaced by the dielectric function of the liquid. In other words, the generalization to an absorptive liquid gap is technically very straightforward, but conceptually it is far from obvious. Recently this issue was addressed again by Pitaevskii. [79]

2.4 The Lifshitz formula

An analytical expression for the GFT can be found for two parallel plates in the range of long wavelength fluctuations. The simplest configuration consists of two semispaces made from different materials characterized by the dielectric functions $\varepsilon_{1,2}(\omega)$ separated by a gap of width d, filled with a material characterized by the dielectric function ε_0. (See Fig. 2.1). The Casimir-Lifshitz force can still be obtained analytically for a stratified multilayered medium, in which the semipaces in Fig. 2.1 are replaced by parallel slabs of different materials, [80] and in a plane-sphere geometry beyond the proximity force approximation, [81] but these cases will not be discussed in this thesis.

2.4.1 Real frequency representation

Due to the symmetry around the x and y axes, only the component of the MST perpendicular to the surfaces needs to be considered: $< T_{zz} >$. The GFT must be evaluated at $z = z' \to -d/2$. It is worth emphasizing that this limit must be taken from inside the gap where the MST is well defined. The solution of Eq. (2.4) is very similar to the one for the optical problem of a cavity. The final result for the force is

$$F(d, T) = \tfrac{\hbar}{2\pi^2} \int_0^\infty d\omega \coth(\tfrac{\hbar\omega}{2k_bT}) \mathrm{Re}\Big[\int_0^\infty dQ Q k_0 g(Q, \omega) \Big], \tag{2.8}$$

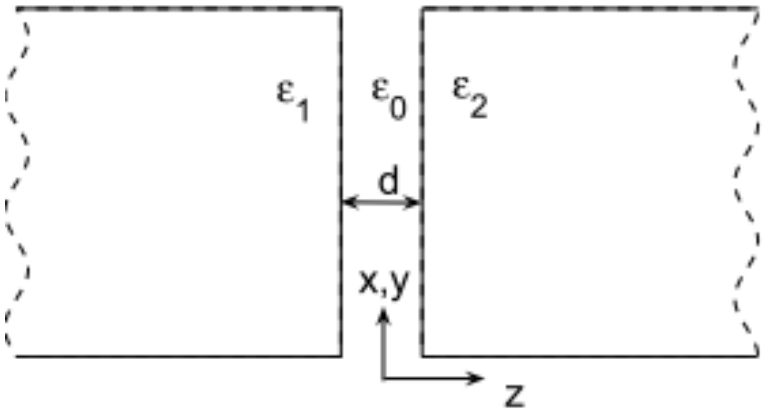

Figure 2.1: *Two semispaces separated by a distance d*

where the wave vector in he gap is $\mathbf{K} = (\mathbf{Q}, k_0)$ with the z-component $k_0 = \sqrt{\varepsilon_0\omega^2/c^2 - Q^2}$. The function $g(Q,\omega)$ is a short hand notation for

$$g(Q,\omega) = \sum_{\nu=s,p} \frac{1 - D_\nu}{D_\nu} \tag{2.9}$$

where

$$D_\nu(Q,\omega) = 1 - r_1^\nu r_2^\nu e^{2ik_0 d}. \tag{2.10}$$

The functions $r_{1,2}^\nu$ denote the reflection coefficients of the inner surfaces of the plates (labeled as 1 and 2) for two different polarizations: $\nu = p$ denotes transverse magnetic (TM) polarization and $\nu = s$ denotes transverse electric (TE) polarization. (The letters s and p originate from the German words 'senkrecht' and 'parallel'). Strictly speaking, there should be a cutoff at large frequencies, where the wavelengths are comparable to the distances between atoms. This is why it can be assumed that the integrand tends to zero as $\omega \to \infty$. The function $g(Q,\omega)$ can be written as

$$g(Q,\omega) = \sum_{\nu=s,p} \sum_{m=1}^{\infty} (r_1^\nu r_2^\nu)^m e^{2imk_0 d}, \tag{2.11}$$

which signifies that multiple reflections occur within the cavity formed by the surfaces of the bodies 1 and 2. The frequency dependent factor $\coth(\hbar\omega/2k_bT)$ originates from the fluctuation dissipation theorem.

The quantities $r_{1,2}^\nu$ are known as the Fresnel reflection coefficients. In the simple geometry with the two half spaces in Fig. 2.1 they can be expressed in terms of the z-components of the wave vector k_0 between the bodies and k_i in the i^{th} body as follows:

$$r_i^s = \frac{k_0 - k_i}{k_0 + k_i} \qquad r_i^p = \frac{\varepsilon_i k_0 - \varepsilon_0 k_i}{\varepsilon_i k_0 + \varepsilon_0 k_i}, \tag{2.12}$$

where

$$k_0 = \sqrt{\varepsilon_0(\omega)\omega^2/c^2 - Q^2} \qquad k_i = \sqrt{\varepsilon_i(\omega)\omega^2/c^2 - Q^2} \qquad i = 1, 2. \tag{2.13}$$

The formulas (2.12) and (2.13) have to be inserted into the real frequency representation Eq. (2.8). Note that the components of the wave vectors in Eq. (2.13) can be imaginary: this case corresponds to evanescent modes, whereas real wave vector components correspond to propagating modes.

The Lifshitz formula Eq. (2.8) is an integral over real frequencies. For numerical force calculations this is a very unpractical expression because of the rapidly oscillating factor $e^{ik_0 d}$. [3] Nonetheless, the real frequency representation should be considered the main one. This is because in some cases the result can only be written as an integral over real frequencies, e.g. systems out of thermal equilibrium. [74]

2.4.2 Imaginary frequencies representation

The problem of a rapidly oscillating integrand can be resolved by a rotation of the integration contour in the complex frequency plane, from the real to the imaginary axis. (See Fig. 2.2). This is possible because this integrand is a meromorphic[1] function of frequency. This rotation from real to imaginary frequencies is an example of a Wick rotation. After

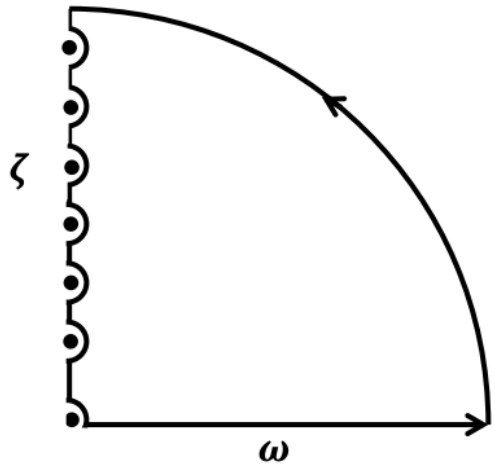

Figure 2.2: *Schematic of the contour in the complex frequency plane. The dots indicate the singularities which are the Matsubara frequencies of Eq.* (2.14).

this rotation the force can be written as an integral over imaginary frequencies. Only the poles of the function $\coth(\hbar\omega/2k_bT)$ contribute to this integral. These poles are located at the following frequencies

$$\omega_n = i\zeta_n = i\frac{2\pi k_b T}{\hbar}n, \qquad n = 0, 1, 2..., \tag{2.14}$$

[1] Analytic except for a discrete set of poles.

where ζ denotes the imaginary part of the frequency. After this transformation the Lifshitz formula (2.8) takes the following form:

$$F(T,d) = \frac{k_b T}{\pi} {\sum_{n=0}^{\infty}}' \int_0^{\infty} dQQ|k_0|g(Q,i\zeta_n), \tag{2.15}$$

where the 'prime' indicates that the term corresponding to $n = 0$ should be multiplied with a factor 1/2. The quantities $g(Q,i\zeta_n)$ and $|k_0| = \sqrt{\varepsilon_0(i\zeta_n)\zeta_n^2/c^2 + Q^2}$ no longer oscillate as a function of frequency. The result Eq. (2.15) was also obtained in Ref. [3] from a thermal GFT approach, where the frequencies of Eq. (2.14) are recognized as Matsubara frequencies. Note that in the imaginary frequency representation of Eq. (2.15) the EM modes can no longer be separated into propagating and evanescent ones.

To obtain the transformed Fresnel reflection coefficients, an analytic continuation must be performed on Eqs. (2.12) and (2.13). For instance the z-component of the wave vector inside the cavity at a frequency $i\zeta$ becomes

$$k_0 = i\sqrt{\varepsilon_0(i\zeta)\frac{\zeta^2}{c^2} + Q^2}, \tag{2.16}$$

where the sign of the square root is adjusted in such a way that it meets the Sommerfeld radiation condition: only decaying waves are allowed to exist within the material, i.e. $\mathrm{Im}k_0 > 0$. Hence it has become clear that the reflection coefficients depend on the permittivities at imaginary frequencies $\varepsilon(i\zeta)$. These quantities cannot be measured directly, but they can be expressed in terms of the directly observable quantity $\mathrm{Im}[\varepsilon(\omega)]$ via the Kramers-Kronig relation [73, 78]:

$$\varepsilon(i\zeta) = 1 + \frac{2}{\pi}\int_0^{\infty} d\omega \frac{\omega \mathrm{Im}[\varepsilon(\omega)]}{\omega^2 + \zeta^2}. \tag{2.17}$$

The main idea behind this expression is that the media involved obey causality in the sense of classical electrodynamics. The permittivities are considered in the frequency domain, and it is required that the interaction between the EM waves and the medium occurs after entering said medium in the time domain. Mathematically it is stated that the permittivity must be a meromorphic function of frequency, so that it satisfies the Kramers-Kronig relation (2.17). Since the quantity $\mathrm{Im}[\varepsilon(\omega)]$ is associated with the amount of dissipation of EM energy into a medium, it must always be positive. Hence from Eq. (2.17) it can be concluded that $\varepsilon(i\zeta)$ must also be positive and monotonically decreasing with ζ.

Eq. (2.17) also shows that, for a medium without dissipation $\mathrm{Im}[\varepsilon(\omega)] = 0$, the force would also be zero. So the very existence of the dispersion forces is closely related to EM dissipation. This relation is a consequence of the fluctuation-dissipation theorem. Moreover, Eq. (2.17) implies that the force depends on $\mathrm{Im}[\varepsilon(\omega)]$ in the sense of a functional.

2.5 Basic properties of the Lifshitz formula

2.5.1 Zero point and thermal contributions to the force

In the real frequency representation (2.8) it is not very difficult to separate the thermal and the zero point energy contributions to the total dispersion force. The equality

$$\coth(\tfrac{\hbar\omega}{2k_bT}) = 1 + \frac{2}{\exp(\tfrac{\hbar\omega}{k_bT}) - 1} \tag{2.18}$$

can be used for this purpose: the first term on the right hand side persists in the limit $T \to 0$, which means that it is associated with the zero point energy. The second term can be identified with thermal modes. Both contributions are difficult to evaluate numerically due to the aforementioned rapidly oscillating integrands.

Therefore it is reasonable to proceed to the imaginary frequency representation Eq. (2.15), where the thermal contribution is separated by taking the limit $T \to 0$. In this limit the Matsubara sum in Eq. (2.15) becomes a Riemann sum for an integral with respect to the continuous variable ζ. The zero point contribution becomes

$$F(d) = \frac{\hbar}{\pi^2} \int_0^\infty d\zeta \int_0^\infty dQ |k_0| g(Q, i\zeta). \tag{2.19}$$

The thermal contribution is the difference between Eqs. (2.15) and (2.19): $\Delta_T F \equiv F(d,T) - F(d)$.

The typical wavelength of this thermal contribution is the thermal wavelength $\lambda_T = \hbar c/k_bT$, which at room temperature is about 7.6 μm. At separation distances much shorter than λ_T, $d \ll \lambda_T$, the thermal contribution becomes negligible and Eq. (2.19) can be used to calculate the force. at much larger separations, $d \gg \lambda_T$, the thermal contribution dominates, and only the $n = 0$ term contributes significantly to the sum (2.15). As $n = 0$ implies that $\zeta \to 0$, only the static permittivities, $\varepsilon_{00} \equiv \varepsilon_0(0)$ and $\varepsilon_{0i} \equiv \varepsilon_i(0)$ need to be considered in this case. This simplifies Eq. (2.15) to [3]:

$$\Delta_T F(T,d) = \frac{k_bT}{16\pi d^3} \int_0^\infty \frac{dx x^2}{\frac{(\varepsilon_{01}+\varepsilon_{00})(\varepsilon_{02}+\varepsilon_{00})}{(\varepsilon_{01}-\varepsilon_{00})(\varepsilon_{02}-\varepsilon_{00})} - 1}. \tag{2.20}$$

Note that this large distance limit gives rise to a purely classical force: $\hbar$ does not occur in Eq. (2.20), because only large wavelengths (or low frequencies) contribute significantly. Moreover, only p-polarizations contribute to Eq. (2.20). This is because the reflection coefficient for s-polarization in Eq. (2.12) vanishes at $\zeta \to 0$. This property can be interpreted as follows: [82–84] In the static limit the s-polarized field becomes purely magnetic, which freely penetrates non-magnetic materials, implying that $r_i^s = 0$. On the

other hand, the p-polarized field becomes purely electric, which is reflected by a material with $r_i^p = (\varepsilon_{0i} - \varepsilon_{00})/(\varepsilon_{0i} + \varepsilon_{00})$.

The thermal force of Eq. (2.20) becomes significant at very large separations where the force itself is extremely weak. For example at a separation of d =10μm and at a temperature of $T = 300$ K, the the force between ideal metal plates in vacuum ($\varepsilon_{0i} \to \infty$, $\varepsilon_{00} = 1$) is:

$$\Delta_T F(d,T) = \frac{k_b T \zeta(3)}{8\pi d^3} = 2 \cdot 10^{-7} \mathrm{N/m}^2. \tag{2.21}$$

The thermal force has been observed only recently [85] by measuring the frequency shift of the motion of the center of mass of atomic cloud at a distance of a few microns from a dielectric substrate. [86,87] Later it has been measured at room temperature with a torsion pendulum. [88] The weakness of the thermal force makes it of limited interest for MEMS and NEMS applications, since at separations where dispersion forces become appreciable the thermal contribution can typically be neglected.

2.5.2 Limiting cases of the Lifshitz formula

Since this thesis focuses on MEMS/NEMS applications, the thermal force does not hold our main interest. Therefore Eq. (2.19) will in this subsection be considered the main formula for the dispersion force. Here it will be shown that the van Waals (1.1) and Casimir (1.2) forces are limiting cases of Eq. (2.19), as it was claimed before.

Let us first introduce a so called characteristic frequency, which is purely imaginary with imaginary part:

$$\zeta_c \equiv \frac{c}{2d}, \tag{2.22}$$

which plays a considerable role in the evaluation of the force: the main contributions to the force are at imaginary frequencies $\sim \zeta_{ch}$. On the other hand, the real frequency $\omega = c/2d$ has no such physical significance, once again due to the rapidly oscillating integrand in (2.8) on the real frequency axis. The range of real frequencies contributing to the force depends on the materials involved.

Let ω_{0i} be the typical resonance frequency in the absorption spectrum of the material inside the gap (i.e. $i = 0$). Then the large frequencies $\omega \gg \omega_{0i}$ will not contribute significantly to the permittivity at imaginary frequencies $\varepsilon(i\zeta)$ in Eq. (2.15). The van der Waals regime corresponds to separations small enough for ζ_c to be the largest frequency that still contributes: $\omega_{0i} \ll \zeta_c$. This condition must hold for all media involved. (Equivalently one can think of this as the limit $c \to \infty$ where retardation is neglected). Because of the factor $e^{-2|k_0|d}$ in the function $g(Q, i\zeta)$, the important values of k_0 are $|k_0| \sim 1/2d$, and the condition $\zeta_c \gg \omega_{0i}$ implies:

$$[\varepsilon_i(i\zeta) - \varepsilon_0(i\zeta)]\frac{\zeta^2}{c^2} \ll |k_0|^2. \tag{2.23}$$

Under this condition the reflection coefficients become

$$r_i^s \approx 0 \qquad r_i^p \approx \frac{\varepsilon_i(i\zeta) - \varepsilon_0(i\zeta)}{\varepsilon_i(i\zeta) + \varepsilon_0(i\zeta)}. \tag{2.24}$$

Note that the s-polarization does not contribute like in the case of very large separations $d \gg \lambda_T$. The physical reason is the same: in the limit $\zeta \ll \zeta_c$ the field becomes quasi-static (as retardation is ignored), and for this field the s-polarization (i.e. the magnetic field) is not reflected.

It is convenient to introduce a new integration variable $x \equiv 2d|k_0|$. Inserting the reflection coefficients from (2.24) into Eq. (2.19) yields:

$$F(d) = \frac{\hbar}{16\pi^2 d^3} \int_0^\infty d\zeta \int_0^\infty \frac{dx x^2}{\frac{(\varepsilon_1+\varepsilon_0)(\varepsilon_2+\varepsilon_0)}{(\varepsilon_1-\varepsilon_0)(\varepsilon_2-\varepsilon_0)} e^x - 1}, \quad \zeta_c \ll \omega_{0i}, \tag{2.25}$$

where, contrary to (2.20), the permittivities $\varepsilon_{1,2}$ depend on ζ. Note that the double integral in (2.25) does not depend on distance. Equating (1.1) to (2.25) yields the following expression for the Hamaker coefficient:

$$A_H = \frac{3\hbar}{8\pi} \int_0^\infty d\zeta \int_0^\infty \frac{dx x^2}{\frac{(\varepsilon_1+\varepsilon_0)(\varepsilon_2+\varepsilon_0)}{(\varepsilon_1-\varepsilon_0)(\varepsilon_2-\varepsilon_0)} e^x - 1}. \tag{2.26}$$

In the opposite limit, the separation d is large enough so that $\zeta_c \ll \omega_{0i}$, but not large enough for the thermal contribution to become significant i.e. $d \ll \lambda_T$, we introduce a new variable $p \equiv x\zeta_c/\zeta$ in (2.19) (where $x = 2d|k_0|$). By definition $p \geqslant 1$ and typically $x \sim 1$ due to the exponential dependence. This implies that $\zeta < \zeta_c$, and because ζ_c is small, we can equate the permittivities to the static ones: $\varepsilon_i(\zeta) \approx \varepsilon_i(0)$. This simplification changes Eq. (2.19) to

$$F(d) = \frac{\hbar c}{32\pi^2 d^4} \int_1^\infty \frac{dp}{p^2} \int_0^\infty dx x^3 g(x,p)|_{\varepsilon_i=\varepsilon_{0i}}, \qquad \zeta_c \ll \omega_{0i} \tag{2.27}$$

The double integral depends also in this case on the permittivities of the materials. However, now both polarizations contribute to the force, and the force decreases faster with d due to the retardation effect. This effect is also apparent because of the factor ζ_c difference with the van der Waals force in (2.25). Now if the materials in (2.27) are ideal metals, i.e. $\varepsilon_{0i} \to \infty$ $(i = 1, 2)$, and the gap consists of vacuum ($\varepsilon_{00} = 1$), then the reflection coefficients equal unity: $r_i^p = 1 = r_i^s$ and the Casimir formula (1.2) is reproduced.

The formulas (2.25) and (2.27) are valid only in limiting cases and can be used only for approximate guesses in typical separation ranges for MEMS and NEMS. For $d \sim 1$nm Eq. (2.25) holds to reasonable accuracy [89] and Eq. (2.27) applies at $d \sim 1\mu$m [90] (at larger distances the thermal contribution must be included). However, in the ranges from 1 nm up to 1 μm calculating the force numerically via Eq. (2.19) is preferable.

2.5.3 Concluding remarks

The Lifshitz formula (2.8), (sometimes known as Dzyaloshinskii-Lifshitz-Pitaveskii (DLP) formula [2]), is an important basic result, not just for this thesis but also for the field of Casimir physics as a whole. Presently many efforts are directed toward generalizing it. [9] For example, in this chapter only nonmagnetic materials have been discussed, where the magnetic permeability equals unity: $\mu = 1$. However, materials with $\mu \neq 1$ also exist. The theoretical description of dispersion forces between slabs of magnetic materials has been established only relatively recently. [91] Not much later, theoretical lower and upper limits have been derived [92] for the Casimir force at $T = 0$:

$$-\frac{7}{8}F_C(d) \leqslant F_{Cas}(d) \leqslant F_C(d) \tag{2.28}$$

where $F_C(d)$ denotes the Casimir force between perfect reflectors given by Eq. (1.2). The minus sign on the left hand side of Eq. (2.28) indicates that the force is repulsive. This lower limit corresponds to the case where a perfectly reflecting mirror faces a perfectly permeable one: $\varepsilon_1 \to \infty$, $\mu_2 \to \infty$. The upper limit corresponds to two perfect mirrors: $\varepsilon_{1,2} \to \infty$. The repulsive lower limit to the Casimir force instigated investigation of the possibility of repulsive Casimir forces between metamaterial [93] or topological insulator [94] slabs. It is hoped that such a repulsive force can help prevent stiction in MEMS with moving components separated by an air or vacuum gap.

Chapter 3

Roughness correction to the Casimir force[1]

3.1 Introduction

There are three effects that must be accounted for when calculating the Casimir force between real interacting surfaces: The influence of optical properties of the materials, surface roughness, and temperature contributions. Temperature has been shown to have a significant effect only at separations larger than 1 μm, because at shorter separations the thermal modes do not fit between the surfaces at room temperature. [16] However, at separations less than 1 μm, especially in the range below 100 nm, the influence of optical properties and surface roughness should be carefully taken into consideration.

Scattering on rough surfaces is a stochastic process: in general there is insufficient information to derive an exact roughness correction to the Casimir force. A possible way to cope with this is a perturbative approach: [68,69,95] it is assumed that a rough surface is a small deviation from a smooth surface. Moreover, the slopes of the surface profiles must be small. Such assumptions provide enough constraints to come to an analytical expression for the Casimir force between rough bodies. This approximation is valid at separations d much larger than the root-mean-square (rms) roughness w: $d \gg w$. For $d \sim w$ there is no analytical solution to the problem. This is why there is no (analytical) method beyond perturbation theory. Another method to estimate dispersion forces is the so called proximity force approximation (PFA). [96] When applied to rough surfaces [97] it assumes that the force between rough surfaces can be presented as the sum of forces between opposing flat surfaces. This method is valid in the case of small separations in comparison to the correlation length ξ of the roughness: $\xi \gg d$, because it assumes the contribution of different patches to be independent of each other.

Statistical analysis of rough gold samples has demonstrated the presence of peaks considerably higher than w. [98] In this chapter, we will show that the contribution of these peaks can be calculated with the PFA, and that the contribution of the height values closer

[1]This chapter is based on W Broer, G Palasantzas, J Knoester, and V B Svetovoy *Roughness correction to the Casimir force beyond perturbation theory.* Euro Phys. Lett. **95,** 30001 (2011) and on W Broer, G Palasantzas, J Knoester, and V B Svetovoy *Roughness correction to the Casimir force at short separations: Contact distance and extreme value statistics.* Phys. Rev. B **85,** 155410 (2012)

to the average can be evaluated perturbatively. This distinction gives a reliable estimate of the Casimir force at short separations. In the present chapter, this method will be discussed in detail, and results for multiple gold samples will be shown. Moreover, this chapter includes an estimate of the influence of the shapes of the peaks, and a prediction of the Casimir force in a technologically relevant situation.

This chapter is organized as follows: after the introduction it will provide the starting points of this approach: Lifshitz theory and the statistics of rough surfaces. This is followed by an outline of the model with derivations of the main formulas. Section 3.4 will specifically address the role of the shape of the peaks. In section 3.5, we will present a prediction for a relatively smooth sample. In such a case, force measurements are hindered by jump to contact, but force predictions are useful for applications in direct bonding technology. [62] Just before the final section with the conclusions, we will evaluate the results and compare them to experimental data from Ref. [67].

It will be shown that these experimental results can be reproduced with this simple model, that distinguishes statistically rare high asperities from asperities with heights typically within w of the average. The statistical description of these high asperities require extreme value statistics - in particular Gumbel distributions -, whereas more common (typical) asperities can be fitted to a normal distribution. One of the consequences of this principle is that the Casimir force can become two orders of magnitude larger for relatively smooth surfaces (with $w < 2$ nm) than for very rough surfaces (with $w \approx 10$ nm). The influence of the shapes of the peaks turns out to be negligible. This is due to the lack of sharp asperities on gold surfaces and the statistical rarity of the relatively high asperities.

3.2 Starting points and assumptions for force calculations

3.2.1 Lifshitz theory

Since this chapter focuses on the calculation of the Casimir force at separations below 100 nm, where surface roughness and optical properties play important roles, its temperature dependence can be ignored. [16] (See also chapter 2). The starting point of our calculations is the macroscopic Casimir-Lifshitz energy per unit area between parallel dielectric plates separated by a vacuum gap of width d in the low temperature limit where $k_bT \ll \hbar c/2d$: [2]

$$E(d) = -\frac{\hbar}{16\pi^2 d^2} \sum_{\mu=s,p} \int_0^\infty \mathrm{d}\zeta \int_{\zeta/\zeta_c}^\infty x^2 \mathrm{d}x \ln(1 - R_\mu e^{-x}), \tag{3.1}$$

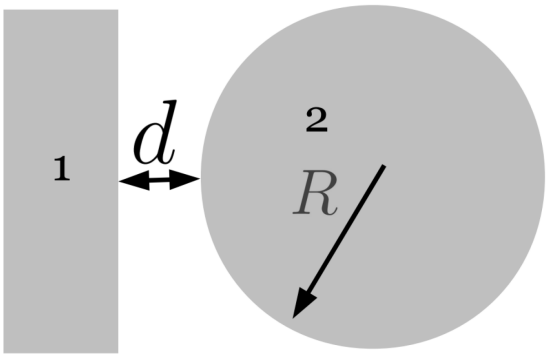

Figure 3.1: *Sketch of the plate-sphere setup considered here (not to scale). R denotes the radius of the sphere and d the distance of closest approach between the sphere and the plate. In this case $R \gg d$ so that the PFA can be used to neglect the curvature of the sphere.*

where $x = 2k_0 d$, $k_0 = \sqrt{\zeta^2/c^2 + q^2}$, q denotes the radial wavenumber, ζ the imaginary part of the frequency, and $\zeta_c \equiv c/2d$ the characteristic frequency. Finally, $R_\mu = r_{1\mu} r_{2\mu}$ denotes the product of the Fresnel reflection coefficients for plate 1 ($r_{1\mu}$) and plate 2 ($r_{2\mu}$), given by:

$$\begin{aligned} r_{js} &= \frac{k_0 - k_j}{k_0 + k_j} \\ r_{jp} &= \frac{\varepsilon_j(i\zeta)k_0 - k_j}{\varepsilon_j(i\zeta)k_0 + k_j}, \end{aligned} \tag{3.2}$$

where the subscript $\mu = s, p$ denotes the polarization and the index $j = 1, 2$ labels the bodies. The permittivities at imaginary frequencies can be obtained from the ones at real frequencies via the Kramers-Kronig relations, Eq. (2.17).

Calculation of the Casimir force requires knowledge of the imaginary parts of the permittivities in a broad frequency range. For this purpose we used ellipsometry data for the frequency dependent permittivities of Au surfaces measured in the range of 0.038 to 9.85 eV (see Fig. 3.2). We have extrapolated to frequencies below 0.038 eV with the Drude model:

$$\varepsilon(\omega) = 1 - \frac{\omega_p^2}{\omega(\omega + i\omega_\tau)}, \tag{3.3}$$

where the values of the plasma frequency ω_p and the relaxation parameter ω_τ were: [99] $\omega_p = 7.8$ eV, $\omega_\tau = 49$ meV. The Drude model of Eq. (3.3) is applicable to metals. All metals have a finite conductivity. This implies that $\varepsilon(\omega) \to 4\pi\sigma/\omega$, where σ denotes the conductivity. This behavior is a direct consequence of Ohm's law and it as a fundamental character related to causality in the sense of classical electrodynamics. Because of the pole at zero frequency, low frequencies contribute considerably to $\varepsilon(\zeta)$ even for relatively large values of ζ (e.g. in the visible range). (See the Kramers-Kronig relation Eq. (2.17)). [100]

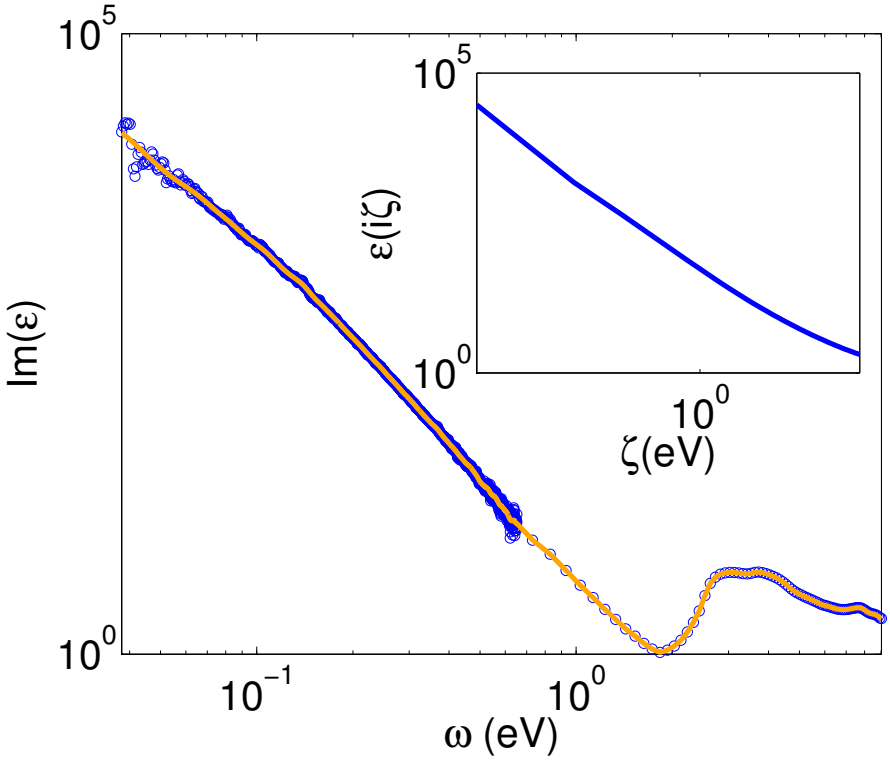

Figure 3.2: *Ellipsometry data of a gold sample. The main panel shows the imaginary part of the dielectric function. The (blue) circles represent ellipsometry measurements, and the continuous (orange) line is a smoothed fit, which was used in the calculations. The inset is a plot of the permittivity at imaginary frequencies $\varepsilon(i\zeta)$ as obtained from the Kramers-Kronig relations. The latter function enters the Lifshitz formula for the Casimir force calculations between smooth surfaces.*

Finally, in order to compare to experimental results, we give the corresponding expression for the force. Experiments are commonly performed in a sphere-plate configuration to avoid problems with the alignment between parallel plates (Fig. 3.1). If the radius of the sphere R is much larger than the separation d, the PFA can be used to neglect the effect of the sphere's curvature on the Casimir force via

$$F(d) = 2\pi R E(d) \qquad R \gg d, \tag{3.4}$$

where $E(d)$ is given by Eq. (3.1). In a plate-plate configuration this approximation is not necessary and the Lifshitz formula [2] provides an explicit expression for the force: $F(d) = -E'(d)A$, where A is the surface of each plate.

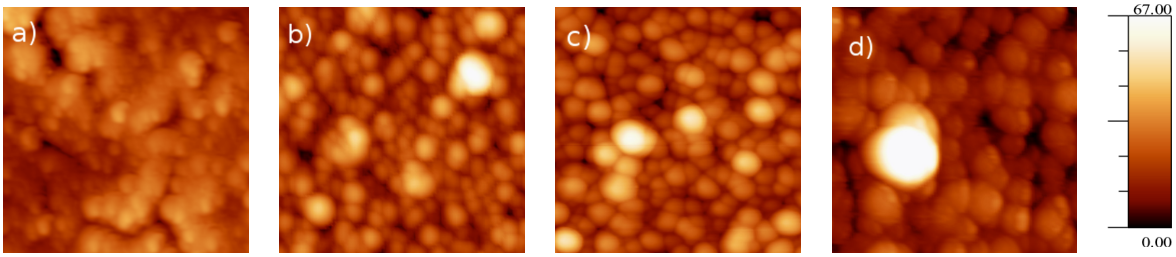

Figure 3.3: *AFM scans of the samples used in the calculations. An area of 1μm×1μm is shown in each picture. The parameters for the actual calculations were: For the sphere (shown in (a)) an area of 8μm×8μm was scanned at a resolution of 2048×2048 pixels. For the 1600 nm sample (shown in (b) this area was 40μm×40μm at a 2944×2944 resolution. The scan size for the 1200 nm sample (Fig. (c)) was 10μm×10μm at a 2048×2048 resolution. The area and resolution used for the 800 nm sample (Fig. (d)). are respectively 40×40μm^2 and 4096×4096 pixels. The color bar indicates the vertical scale in nm.*

3.2.2 Extreme value statistics and contact distance

Assessing the influence of random surface roughness on the Casimir force requires knowledge of the proper probability distributions of the height fluctuations of the surfaces. These were obtained from AFM scans of each film with lateral resolutions varying from 4 to 10 nm, for areas up to $40 \times 40\mu m^2$. (See Fig. 3.3 for detailed parameters.) This information enables us to perform a detailed roughness analysis of the samples. By counting the number of features smaller than some value z and normalizing this number, the cumulative probability $P(z)$ to find a feature smaller than z is obtained. It turns out that this probability approaches 1 very fast at $z \to \infty$ and 0 $z \to -\infty$. This is why, for a proper analysis of the AFM data, it is convenient to write $P(z)$ as:

$$P(z) = 1 - e^{-\phi(z)}, \tag{3.5}$$

where the "phase" $\phi(z)$ is a positive, monotonically increasing function of z, defined as

$$\phi(z) \equiv -\ln(1 - P(z)). \tag{3.6}$$

The derivative of $P(z)$,

$$f(z) \equiv P'(z) = (1 - P(z))\phi'(z), \tag{3.7}$$

is the probability density function. It was established [98] that $\phi(z)$ could not be fitted to any known distribution for all z and that for large $|z|$ a generalized extreme value distribution is needed. Figure 3.4 shows the natural logarithm of the phase $\phi(z)$, collected from the AFM images. It is clear that this function behaves linearly in the asymptotic regimes:

$$\ln \phi(z) = A_+ z + B_+, \tag{3.8}$$

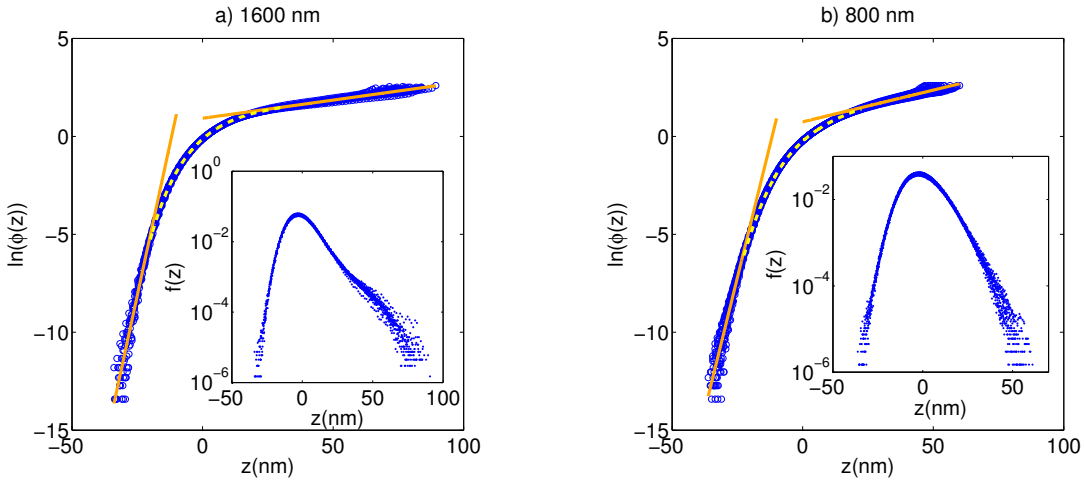

Figure 3.4: *Statistics of the topography of the surfaces. The logarithm of the "phase" is plotted as a function of the height with respect to the mean plane $z = 0$. The open circles represent the data from AFM topography scans: (a) is for the 1600 thick film and (b) the 800 nm thick one. The solid (orange) lines represent linear fits for $|z| \gg 1$. This implies that the probability to find a large feature behaves as a Gumbel distribution. For intermediate values of z the data are fit with polynomials, indicated by the dashed (yellow) curves. The inset is a semilogarithmic plot of the probability density function $f(z)$. It shows significant deviation from a normal distribution for the 1600 nm sample. The distribution of the 800 nm sample deviates less from a normal distribution, but it is still clearly not symmetric.*

for large positive z and similarly,

$$\ln \phi(z) = A_- z + B_- \tag{3.9}$$

for large negative z. The values of the coefficients $A_\pm$ and $B_\pm$ are listed in table 3.1. This linear behavior in the asymptotic regimes implies that the probability to find a feature larger than z behaves as a 'double exponential':

$$1 - P(z) \sim \exp(-\exp(\tfrac{z-\mu}{\beta})), \tag{3.10}$$

where β is the scale parameter and μ is the location parameter. This type of behavior is a characteristic of Gumbel distributions, which is an example of extreme value statistics. [101] We will see that this strong dependence will have a considerable impact on the roughness correction to the Casimir force. In this chapter we have analyzed only gold samples and we cannot draw conclusions for other materials. However, the generality of the Gumbel distribution allows us to hope that similar behavior can be found in the roughness statistics of other materials.

The distance upon contact for gold films was discussed in detail in Ref. [98]. The thicknesses of the investigated gold films are associated with different rms roughnesses due

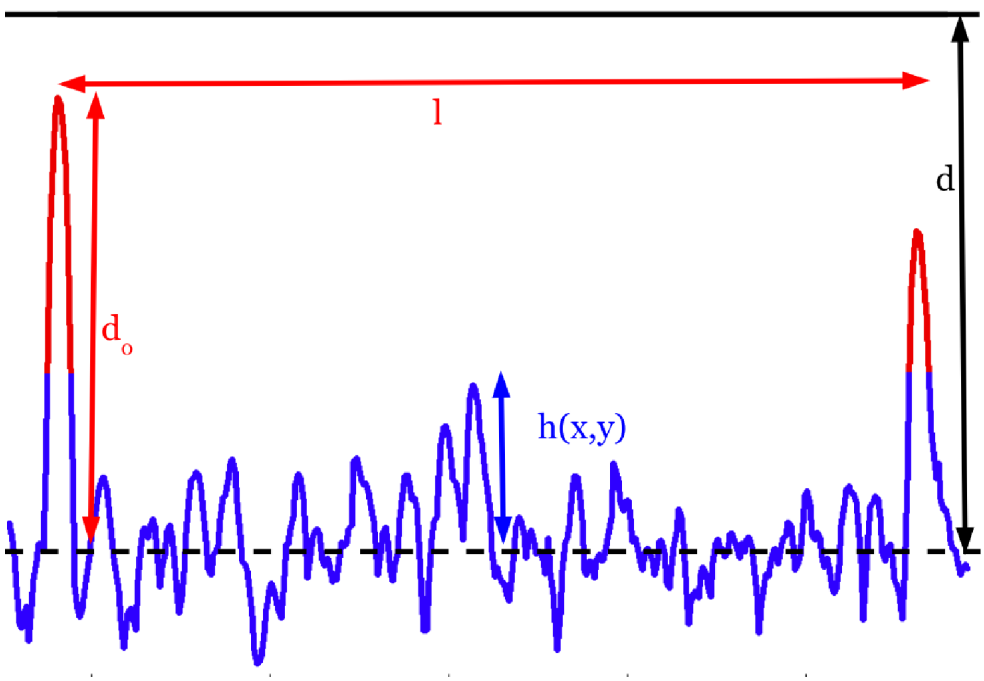

Figure 3.5: *Schematic of a rough surface to clarify the meaning of the parameters l and d_0. Similar to l, l' represents the distance between the deep troughs, and d_0' represents the depth of the deepest pit. $h(x,y) = h_1(x,y) + h_2(x,y)$ is the combined surface profile, so that effectively only one rough surface is considered.*

to the kinetic roughening process. We denote the height fluctuations from the mean surface level by $h_j(x,y)$ for each body ($j = 1, 2$). The local separation distance is $d_{\text{local}}(x,y) = d - h_1(,x,y) - h_2(x,y)$. The averages over a large surface of each profile is zero by definition: $< h_j(x,y)) >= 0$. Another assumption is that the surfaces are statistically independent, i.e. the surface heights are uncorrelated:

$$\langle h_1(x_1,y_1) h_2(x_2,y_2) \rangle = 0 \tag{3.11}$$

which is a condition for a perturbative treatment. [68,69] Consequently, the profiles can be combined so that effectively one rough body with topography $h(x,y) = h_1(x,y) + h_2(x,y)$ is considered, interacting with a flat surface (see Fig. 3.5). In the plate-sphere configuration, the contact distance is defined as [98] the maximum average separation d for which the local distance becomes zero, so that

$$d_0(L) \equiv \max_{x,y} \left[h(x,y) - (x^2 + y^2)/2R \right], \tag{3.12}$$

where L denotes the size of the effective interaction area. The contact distance is the local maximum within the horizontal scale L. In a plate-plate geometry $R \to \infty$ and

Table 3.1: *Values of the relevant parameters for the investigated gold samples. The parameters $A_\pm$ and $B_\pm$ are defined by Eqs.* (3.8) *and* (3.9)*. The subscripts + and − refer to the positive and negative asymptote, respectively. The other parameters are: the rms roughness w of the sample, the correlation length ξ, the size of the effective interaction area L, the contact distance d_0, and the average distance between the high peaks l.*

Width (nm)	A_+ (nm^{-1})	B_+	A_- (nm^{-1})	B_-	w (nm)	ξ (nm)	L (nm)	d_0 (nm)	l (nm)
800	0.0333	0.704	0.542	6.34	7.5	30.6	1560	34.5 ± 1.7	238
1200	0.0188	0.888	0.648	8.34	9.0	38	1980	41.0 ± 1.7	256
1600	0.0192	0.885	0.62	7.32	10.1	42.0	2100	50.8 ± 1.3	380

$d_0 = \max\,[h(x, y)]$. Throughout this chapter it is assumed that the sphere is fixed laterally with respect to the plate and that it does not rotate during force measurements (in reality it is rigidly attached to a cantilever). In other words, we distinguish the *experimental* uncertainty in d_0 from its *statistical* uncertainty. Indeed, if the sphere is allowed to move laterally, the uncertainty in the value of d_0, and therefore in the Casimir force will be considerably larger. [98]

In this chapter it is assumed that the size of the effective interaction area between the sphere and the plate L is much larger than the correlation length: $L \gg \xi$. This ensures that one interaction area contains many independent realizations of a rough surface and hence spatial averages are equivalent to statistical averages. Our approach requires a large size of the plate also on the scale of the separation d: the condition $L \gg d$ ensures that edge effects can be ignored. These conditions for L are realistic: L is in the order of a few microns, while d and ξ are a few tens of nm. (See table 3.1.)

3.3 Model outline

A rough surface can be regarded as a large number of asperities of different heights typically $\sim w$ and lateral sizes ξ with a few occasional high peaks.Here w is the total root mean square roughness defined as $\sqrt{w_{\mathrm{sphere}}^2 + w_{\mathrm{sample}}^2}$. The asperities with the heights $\sim w$ can be well described by a normal distribution. This is clear from the insets in Fig. 3.4: the function $\ln f(z)$ can be approximated by a parabola nearby its maximum. However, the tails of the distribution, which correspond to high peaks or deep troughs, cannot be

described by the normal law. Let us define the parameter d_1 in such a way that asperities with normal heights are smaller than d_1, $h < d_1$, but the high peaks are larger than d_1, $h > d_1$. The value of d_1 belongs to the interval $w < d_1 < d_0$. Its precise value is somewhat up to convention but it can be chosen around $d_1 \sim 3w$. An additional condition on d_1 will be discussed later in this section.

The number of high peaks with the lateral size ξ and the height $h > d_1$ on the area L^2 can be expressed via the "phase" $\phi(z)$ determined from the roughness topography as

$$N = \frac{L^2}{\xi^2} e^{-\phi(d_1)}. \tag{3.13}$$

The average distance between these peaks (Fig. 3.5) is

$$l = \frac{L}{\sqrt{N}} = \xi e^{\phi(d_1)/2}. \tag{3.14}$$

Similarly we say that the deep troughs are those having depths larger than d_1', $h < -d_1'$. The number of these troughs on the area L^2 is

$$N' = \frac{L^2}{\xi^2} \phi(-d_1') \tag{3.15}$$

and the average distance between them is

$$l' = \frac{L}{\sqrt{N'}} = \frac{\xi}{\sqrt{\phi(-d_1)}}. \tag{3.16}$$

Consider first the roughness contribution to the Casimir force in the case of large correlation length $\xi \gg d$. In this limit PFA is a good approximation [68] in the sense that each asperity can be taken into account independently (additively). Then we can calculate the Casimir force $F_{Cas}(d)$ via the standard definition of the statistically averaged function

$$F_{Cas}(d) = \int_{-\infty}^{\infty} \mathrm{d}z f(z) F(d - z). \tag{3.17}$$

Here we defined $f(z) = 0$ outside the interval $-d_0' < z < d_0$. Writing the force as an integral over the entire real axis is useful to obtain a result in terms of statistical parameters, such as w. If additionally the distance between bodies is large in comparison with the roughness, $d \gg w$, we can expand the force between flat plates around $z = 0$ as $F(d - z) = F(d) - F'(d)z + F''(d)z^2/2 + \ldots$ and find the roughness correction:

$$F_{Cas}(d) = F(d) + \frac{F''(d)}{2!} w^2 + \ldots, \quad w \ll d. \tag{3.18}$$

which is the second term in (3.18). The error due to omitted terms can be estimated via the approximate power law dependence of $F(d)$ on d in Eq. (3.4). [100]

Let us separate three different integration intervals in Eq. (3.17):

$$F_{Cas}(d) = \int\limits_{-\infty}^{-d_1'} \mathrm{d}z f(z) F(d-z) + \int\limits_{-d_1'}^{d_1} \ldots + \int\limits_{d_1}^{\infty} \ldots, \tag{3.19}$$

where $\ldots$ stands for $\mathrm{d}z f(z) F(d-z)$. The first term here represents the contribution of deep troughs, the second one is responsible for the contribution of normal peaks, and the third term is the contribution of high peaks. An important observation of this work is that the contribution of normal peaks with the height $\sim w$ can be taken into account perturbatively even if the bodies are already in contact. It follows from the fact [98] that upon the contact the bodies are still separated by the distance d_0, which increases with the area of nominal contact and is in the range $3w \leqslant d_0 \leqslant 5w$. In this case the Taylor expansion for $F(d-z)$ in the second term is justified [102].

Now let us relax the condition $\xi \gg d$. In this case we cannot consider different asperities as independent. The method to calculate the roughness correction beyond the PFA was proposed in the series of chapters [68, 69]. In this approach the roughness is treated perturbatively. We can apply this method only to the second term in (3.19)

$$\int\limits_{-d_1'}^{d_1} \mathrm{d}z f(z) F(d-z) = \int\limits_{-\infty}^{\infty} \ldots + \int\limits_{-\infty}^{-d_1'} \ldots + \int\limits_{d_1}^{\infty} \ldots, \tag{3.20}$$

where we have to understand the function $F(d-z)$ as the Taylor expansion. According to [68, 69] the first term on the right has to be generalized in the following way

$$\begin{aligned} F_{PT}(d) \;\equiv\; & \int\limits_{-\infty}^{\infty} \mathrm{d}z f(z) \left[F(d) - F'(d) z + \frac{F''(d)}{2!} z^2 \right] \\ & \to F(d) + \frac{F''(d)}{2!} \int \frac{\mathrm{d}^2 k}{(2\pi)^2}\, \rho(kd) \sigma(k), \end{aligned} \tag{3.21}$$

where $\sigma(k) = \langle h(k) h(0) \rangle$ is the correlator of the surface profile in k-space. The sensitivity function, $\rho(kd)$, is defined as the ratio between the response functions at arbitrary and at zero wavenumber: $\rho(k) \equiv G(k)/G(0)$. It measures the deviation from the PFA. The proximity force approximation is restored when small wavenumbers $kd \ll 1$ are important (large ξ). In this case the sensitivity function is $\rho(kd) \to 1$ and we reproduce Eq. (3.18). The expression for the function $\rho(kd)$ is given in [68, 69]. It has to be noted that $\rho \geqslant 1$, thus, the PFA underestimates the Casimir force.

When the condition $\xi \gg d$ is broken we are able to calculate the second term in (3.19) by using the perturbation theory but we definitely cannot use the perturbation theory for the third term. This is because at $z = d_0$ the integrand diverges (for $z > d_0$ we defined $f(z) = 0$). This is a physical divergence appearing due to the contact between the highest asperity and the opposite body. However, it can be noted that the high peaks accounted for by the third term in (3.19) are rare and the average distance between them (3.14) is large. If this distance is large in comparison with the separation between bodies, $l \gg d$, we can calculate the contribution of each peak independently of each other (additively). We can always choose d_1 to fulfill the condition $l \gg d$ but in reality $d_1 = 3w$ is an appropriate value in all respects. As one can see from Table 3.1 for all the investigated films the values of l are sufficiently large and the values of d_1 are always smaller than d_0. It is also important that our results are not sensitive to the precise value of d_1 as long as d_1 is around $3w$. This is clear from the insets in Fig. 3.4: there is no sharp point in the function $f(z)$ where the normal distribution becomes inapplicable.

The precise value d_1' for the deep troughs is not important at all. Any value in the interval $w < d_1' < d_0'$ is equally good. This is mainly because the contribution of the deep troughs is small and never dominates but also due to the fact that $\ln \phi(z)$ decreases more sharply at large negative z than it increases at large positive z.

The discussion above shows that the high peaks and deep troughs can be calculated additively even in the case when applicability of the PFA is unjustified. In this case instead of (3.19) we can write

$$F_{Cas}(d) = F_{PT}(d) + \int_{d_1}^{\infty} \mathrm{d}z f(z)\Big[F(d-z) - F(d) + F'(d)z - \frac{F''(d)}{2!}z^2\Big] + \int_{-\infty}^{-d_1'} \mathrm{d}z f(z)\Big[F(d-z) - F(d) + F'(d)z - \frac{F''(d)}{2!}z^2\Big].$$

where the remnants from $F_{PT}(d)$ in Eq. (3.20) are included in the terms responsible for high peaks and deep troughs. The final expression for the force is split into three terms:

$$F_{Cas}(d) = F_{PT}(d) + F_{PFA}(d) + F'_{PFA}(d). \tag{3.22}$$

The first term,

$$F_{PT}(d) = F(d) + \frac{F''(d)}{2!}\int \frac{\mathrm{d}^2k}{(2\pi)^2}\rho(kd)\sigma(k), \tag{3.23}$$

does not rely on the PFA but is instead based on the perturbation theory [68, 69] as indicated by the index PT. It represents the contribution of asperities with typical heights

$\sim w$. The second term,

$$F_{PFA}(d) = \int_{d_1}^{d_0} \mathrm{d}z f(z)\Big[F(d-z) - F(d) + F'(d)z - \frac{F''(d)}{2!}z^2\Big], \tag{3.24}$$

is the contribution of high peaks. In this term the perturbation theory cannot be used to calculate $F(d-z)$ because d and z are comparable. $F_{PFA}(d)$ diverges at $d = d_0$. As was already mentioned this is because the local separation distance becomes zero at $d = d_0$. In this way the model accounts for the case of contact between the bodies. This will turn out to be an important aspect of our approach. The condition $L \gg \xi$ ensures that the interaction area contains enough realizations of a rough surface to approximate an ensemble. *Since the high peaks are statistically rare events they should be far apart, $l \gg \xi$, so that they can be calculated independently of each other.* Previously we assumed [102] that the high peaks have flat tips, so that one can use the PFA to calculate the interaction between an individual peak and a flat surface. This approximation is reasonable (see [102]) but it is not necessary and we relax it in section 3.4.

Finally, the term

$$F'_{PFA}(d) = \int_{-d'_0}^{-d'_1} \mathrm{d}z f(z)\Big[F(d-z) - F(d) + F'(d)z - \frac{F''(d)}{2!}z^2\Big] \tag{3.25}$$

represents the contribution of the deep troughs. By the same token, the distance between them is large, so that their contributions are also independent of each other. These troughs do not dominate the force, because they correspond to negative z, where the leading term $F(d-z)$ is much smaller than the other contributions.

3.4 The influence of the shape of the peaks

In order determine the effect of the shape of the peaks one must first establish what geometry approximates the shape of the real peaks best. We note that the rough surface in the schematic of Fig. 3.5 is a cross section of a real rough gold surface based on an AFM scan of the 1600 nm sample. At present it does not seem feasible to determine the shape of the peaks directly from this image since the size of the tip of the AFM cantilever beam is comparable to the size of the tips of the peaks.

The information in Fig. 3.5 shows that the peaks can be modeled in at least two different ways:

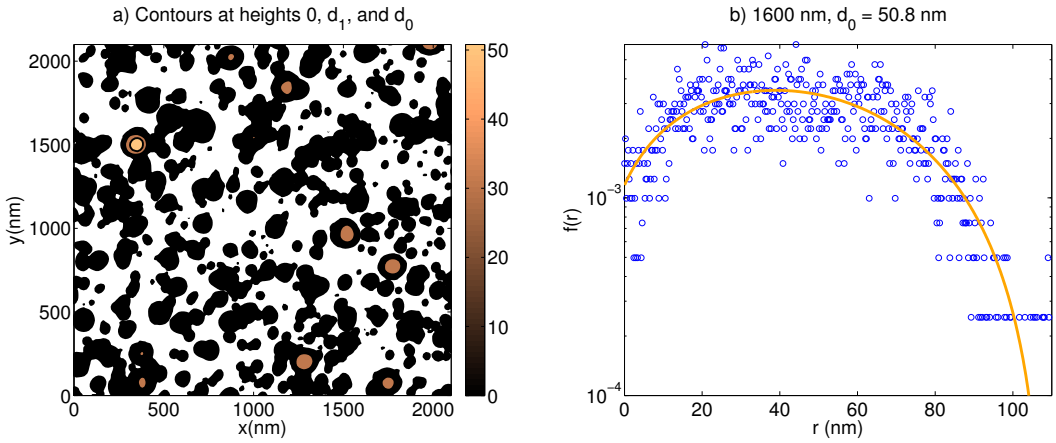

Figure 3.6: *(a) Contour plot of subsurface of size L^2 for the 1600 nm sample, extracted from AFM data. The colorbar indicates the vertical scale in nm. At height $z = d_1 = 30.3$ nm, the polygons can be considered circular by approximation. (b) Semilogarithmic plot of probability density function $f(r)$ of the radii of the peaks. The open circles represent data from the AFM topography scan, the (orange) line is a polynomial fit. This information is used to estimate the range of the horizontal sizes of the peaks.*

1. As half ellipsoids with height d_0, or more specifically, as spheroids: ellipses revolved around the axis perpendicular to the plate .

2. As cones with height d_0.

These geometries could produce significantly different results but they are still consistent with Fig. 3.5. Strictly speaking, one should account for the shape of the troughs as well, but since their contribution is negligible this can be ignored.

First we should obtain an estimate of the lateral sizes of the peaks to make a consistency check: in the model of section 3.3 each asperity is considered to have a lateral size ξ. In the next two paragraphs we will determine which choice of geometry is most consistent with this assumption. The information about the lateral sizes of the peaks can be extracted from the AFM scans. We have computed the contour of each surface sample at height d_1, defined as $d_1 \equiv 3w$, which is 30.3 nm for the 1600 nm sample. See Fig. 3.6a . From the polygon segments of each closed contour the circumferences of the peaks were determined. The associated radii were obtained by assuming circularly shaped bases of the peaks. Typically, high peaks are surrounded by lower peaks, which makes it difficult to distinguish what belongs to the 'peak', and what can be considered 'normal' roughness. Fig. 3.6a shows that the contours at height $z = 0$ cannot be considered circles, whereas the ones at height $z = d_1$ *can*. For the spheroidal case we can reconstruct their radii at

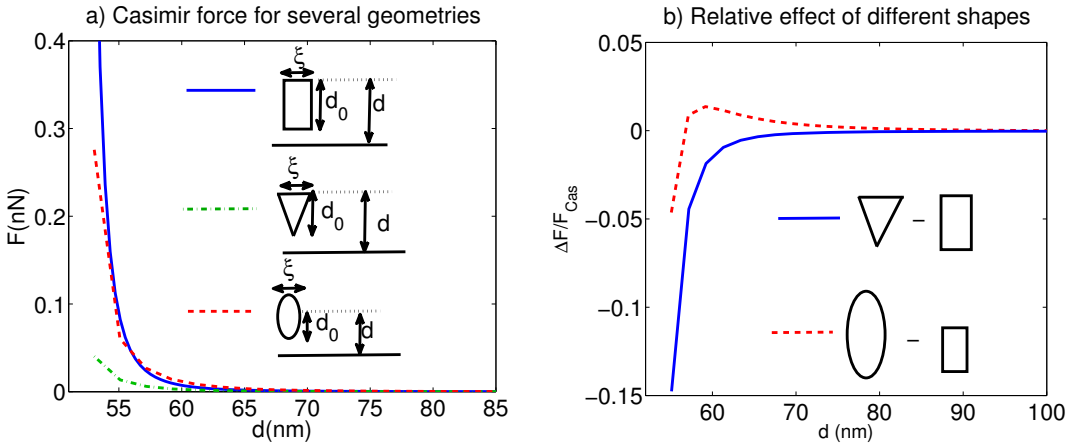

Figure 3.7: *Effect of the shape of the peaks for three different geometries. The case of flat peaks was calculated via the Lifshitz formula. The other two geometries were accounted for by FDTD. In each case, the lateral size is assumed to equal the correlation length ξ, and the height was d_0. Fig. (a) shows the absolute force and Fig. (b) shows the difference ΔF between the FDTD outputs (Eqs.* (3.29) *and* (3.30)*) and the result for flat peaks (Eq.* (3.31)*), relative to the total Casimir force $F_{Cas}(d)$ (from Eq.* (3.22)*)*

.

height $z = 0$ via the relation

$$r_0 = \frac{d_0 r_1}{\sqrt{d_0^2 - d_1^2}}, \tag{3.26}$$

where r_1 represents the (horizontal) radius at $z = d_1$.

With this information we can come to a probability distribution for the radii in the same way as it was done for the heights of the peaks. The probability density function for the radii is shown in Fig. 3.6b. Negative values of r are not allowed, which makes the width distribution $f(r)$ slightly nonsymmetric, with a skewness of 0.23. Still, $f(r)$ is to good approximation a normal distribution, unlike the height distributions in section 3.2.2, where significant deviations from normal distributions were found.

This distribution provides an estimate of the range of values of the lateral sizes of the peaks. The average of this distribution is 44 nm ($\approx 0.9 d_0$), which corresponds to the correlation length, and its standard deviation is 24 nm $\approx 0.5 d_0$. (See table 3.1). Therefore the choice of (half) spheroidal peaks is in this sense a suitable geometry to represent high asperities in this roughness model.

Similarly the radii for the case of conically shaped peaks at $z = 0$ are obtained from the data in Fig. 3.6a as follows:

$$r_0 = \frac{d_0 r_1}{d_0 - d_1}, \tag{3.27}$$

which means that the distribution in Fig 3.6b can still be used, but the variable r must be

replaced by $r \to \sqrt{(d_0+d_1)/(d_0-d_1)}r$. Consequently, this distribution is much broader than the one for the spheroidal case (Fig. 3.6b): the standard deviation is 49.9 nm $\sim d_0$. The mean radius is 90 nm in this setup, which deviates considerably from the value of the correlation length listed in table 3.1. This means that a cone is not a proper geometry to represent a peak in this model. Modeling the peaks as half spheroids seems preferable in this sense. However, we will still investigate the effect of a conical shape on the Casimir force, so that we might compare it to experimental results in Section 3.6.

The Casimir force between a plate and an ellipsoid or cone was calculated numerically. This was done with a finite-difference time-domain (FDTD) [103] program called Meep. [104] Recently it was established that FDTD can be used to calculate the Casimir force in arbitrary geometries . [71, 105, 106] FDTD is a method to numerically solve Maxwell's equations, and its approach for obtaining the Casimir force is similar to that of Ref. [1]. The main difference, of course, is that the Green function tensor is obtained numerically in an arbitrary configuration instead of analytically in the parallel plate geometry.

We start by separating a conductivity correction factor $C(d)$ from the Lifshitz formula (3.4):

$$F(d) = C(d)F_{pc}(d) \tag{3.28}$$

where $F_{pc}(d) = \hbar c\pi^3 R/360d^3$ is the Casimir force between a perfectly conducting plate and sphere in the PFA. Generally there is also a temperature correction factor, but this dependence can be ignored in this separation range. [16] Note that we have already established the correction factor $C(d)$ from permittivity data obtained via ellipsometry measurements (see Fig. 3.2). We now perform the calculation of the curvature effect for perfectly conducting bodies and apply the correction $C(d)$ afterwards, as it was done e.g. in Ref. [107]. Note that it is assumed here that the effects of the material properties and the shape are independent of each other. Generally, this is not true. [81] However, at the short separations considered here, the effect of this correlation appears to be small. [108] This approximation should suffice to estimate the error due to neglecting the shape of the peaks. In this approximation the Casimir force between a dielectric plate and a dielectric spheroid is determined as follows:

$$F_{EP}(d) \approx C(d)F_{EP,PC}(d), \tag{3.29}$$

and similarly for the cone-plate geometry

$$F_{CP}(d) \approx C(d)F_{CP,PC}(d), \tag{3.30}$$

where $F_{EP,PC}(d)$ and $F_{CP,PC}(d)$ represent the outputs of the FDTD simulation with perfectly conducting bodies. The fact that the bodies are perfect conductors and the rotational symmetry of the geometry both reduce the computation time considerably. [106]

The result of the FDTD simulations are shown in Fig. 3.7. They are compared to the

force between peaks with flat tips, which is calculated as follows:

$$F_{pp}(d) = -E'(d)\xi^2, \tag{3.31}$$

where $E'(d)$ is determined from the Lifshitz formula Eq. (3.1). This represents the contribution of a single peak in the PFA according to the model outlined in Section 3.3. The FDTD calculations were done at separations $d > d_0 +$ 2 nm. This is because the FDTD approach requires a surface over which the Maxwell stress tensor is integrated, which in turn requires a buffer between the bodies. [105, 106] In the case of curved peaks there is no need to get any closer since the PFA is recovered at short distances. Moreover, the uncertainty in the value of d_0 is comparable to 2 nm (see table 3.1). It is clear from Fig. 3.7a that, at short separations, the calculation for the spheroidal case is closer to the one for a flat tip than the force between a conically shaped peak and a plate. Fig. 3.7b shows that this is also true in a sense relative to the total force of Eq. (3.22): the maximum effect is almost 5% in the spheroidal case and about 15 % in the cone-plate geometry. In section 3.6 the relative effects of the shapes of the peaks will be compared to experimental results.

The calculations in this section were performed for the 1600 nm sample only. This sample has the highest value of the contact distance d_0 (See table 3.1). The experimental uncertainty in the Casimir force *decreases* with d (See section 3.6). The effect of the shape of the peaks is most likely to be significant in this case, because the highest value of d_0 will not allow lower values of d. Moreover, in the approximation of Eqs. (3.29) and (3.30) $C(d)$ is a monotonically increasing function, so that the total effect will be smaller for samples with a smaller value of d_0. In the case of perfect conductors Maxwell's equations are scale-invariant [109] and one can use the FDTD outputs for smaller values of d_0 as well.

3.5 Direct bonding and surface roughness

Since we have established the basics of our approach, we can demonstrate a prediction of the Casimir force in a technologically relevant case: that of relatively low ($<$ 2 nm) rms roughness. In this case the contact distance is also low ($<$ 10 nm) which allows the bodies to move closer to each other, which in turn can give rise to a higher Casimir force.

Our studies of the influence of roughness on the Casimir force at close surface proximity, i.e. at separations comparable to d_0 are also important for direct bonding technologies. [62,110] Indeed, direct bonding has also become known as van der Waals bonding: Bonding without glue is performed under ambient conditions. Such a bond can only be achieved under strict conditions: [62, 110] the geometrical shape of the elements must be optimally congruous; the smoothness of the mechanically finished surface (rms roughness) must be within the subnanometer range; in most cases, the chemical treatment of the surface must be optimum; the physical state of the surface must be defect free; and the subsurface

damage must usually be as small as possible. After annealing and other procedures, [62,110] the direct bond must become monolithic to guarantee a long life without decohesion of the bonded surfaces.

To be more specific: in order to achieve direct bonding the rms roughness w must be

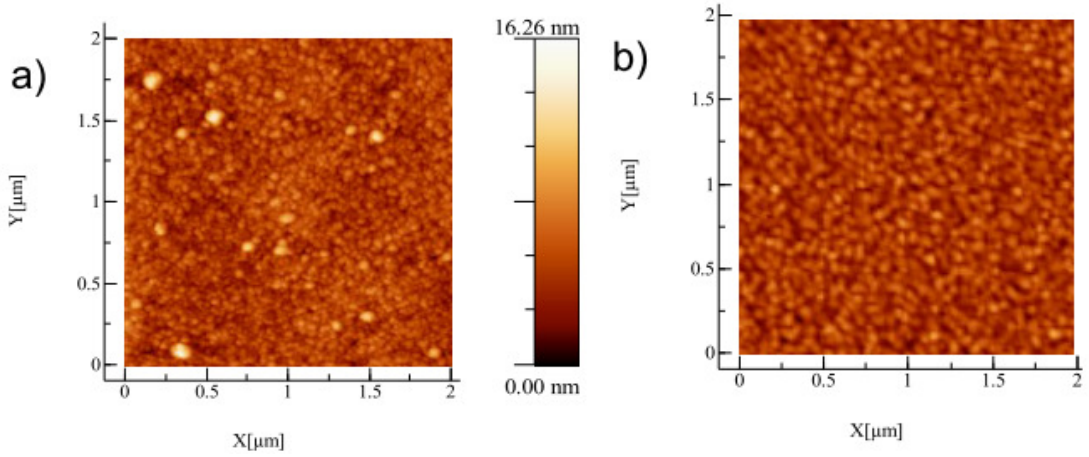

Figure 3.8: *AFM image used for the calculation of the Casimir force in section 3.5. Same conventions as in Fig. 3.3. Fig. (a) shows the profile of the sphere and Fig. (b) that of the plate. Both were scanned at a resolution of 512×512 pixels.*

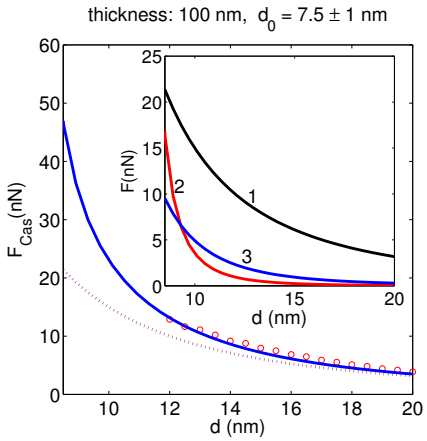

Figure 3.9: *Calculation of the Casimir force between a 100 nm thick sample with rms roughness $w = 1.3$ nm and a sphere with $w_{sph} = 1.8$ nm. The three curves in the inset are the three contributions to the solid curve in the main graph: curve 1 (black) is force without roughness from Eq. (3.4), curve 2 (red) is the peaks'contribution (Eq. (3.24)), and curve 3 (blue) is the perturbative part (second term of Eq. (3.23)). The contribution of the troughs is always negligible. The dotted line gives the result without roughness effects. The red circles denote experimental points. Measurements could not be performed below $d = 12$ nm due to jump to contact.*

< 2 nm and preferably even < 0.5 nm. [62,110] Such roughness parameter values, at least for the upper roughness limit, have also been obtained for gold films deposited by electron beam evaporation. [111] In this case, force measurements were only possible down to 12 nm separations due to jump to contact because of capillary forces, while the estimated distance upon contact via height histogram analysis from AFM images was determined to be $d_0 = 7.5 \pm 1$ nm. [111] In this case of low roughness the Casimir force starts to feel the roughness effect only at separations below 20 nm, as estimations from scattering theory indicated. However, proper analysis of the roughness effect must take into account the contributions of high peaks, especially below 10 nm separations as $d \sim d_0$. These results can be relevant for understanding stiction phenomena under dry conditions (excluding capillary bridge formation) of device components with nanoscale surface roughness, as well as for exploring possibilities of direct bonding phenomena between real surfaces with known optical properties.

As jump to contact due to capillary adhesion prevented measurements at separations below $d = 12$ nm, this calculation is a prediction for this range and not a direct comparison to measurements. The experimental data at separations > 12 nm can be reproduced by scattering theory. [111]

The radius of the sphere was 50 μm, and its rms $w_{sph} = 1.8$ nm. while the rms of the plate was $w = 1.3$ nm. The AFM scans of the sphere and the plate both had scan sizes of 6×6 μm^2 and 5×5 μm^2, respectively.

The results are shown in Fig. 3.5. Near contact, where $d \approx d_0$, there are considerable roughness effects: the Lifshitz formula, the "zeroth order" perturbative contribution, the black curve no. 1 in the inset, dominates at these short separations, but the contribution of the high peaks (the red curve no. 2 in the inset) is of the same order of magnitude there. The perturbative part (the blue curve no. 3 in the inset) is the smallest contribution, but it cannot be ignored further away from contact where the force was measured. The total Casimir force becomes approximately 46 nN near contact, which is an order of magnitude larger than what has been found for the rougher samples. [67] However, this estimate still needs experimental verification, because presently it is not trivial to measure the force at separations below 10 nm.

3.6 Results and Discussion

An important question now is: how accurately can we calculate the roughness corrections? The third order term in the Taylor expansion around $z = 0$ starting from Eq. (3.18), $-F'''(d)z^3/3!$, was neglected. In the separation range of interest (20 to 100 nm) the force between smooth surfaces $F(d)$ shows an approximate power law dependence of d: [100] $F(d) \sim C/d^\alpha$, where C is a constant and the value of the power α depends on the geometry:

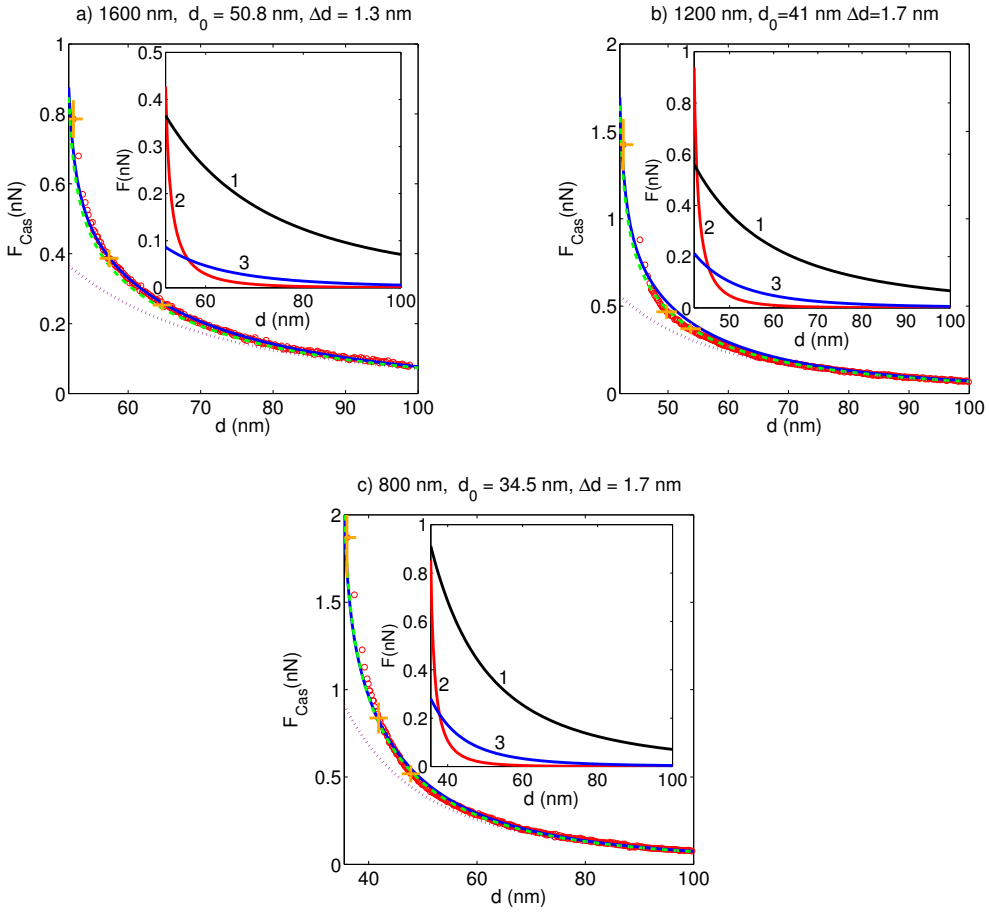

Figure 3.10: *Results of the roughness model (Eq.* (3.22)*, the solid (blue) line)compared to experimental data (from Ref. [67], the (red) circles) for three different gold samples. The (orange) crosses denote the errors in some of the data points. The dashed line is the result of naive application of the PFA via Eq.* (3.34)*. The dotted line is the force without roughness correction. For the insets, the same conventions as in Fig. 3.5 apply.*

in the parallel plate setup $\alpha \approx 3.5$; in the plate-sphere setup $\alpha \approx 2.5$ if $R \gg d$. Therefore the estimate of the error due to the use of perturbation theory is given by:

$$\Delta F_{PT}(d) \approx s\frac{\alpha(\alpha+1)(\alpha+2)}{3!}\left(\frac{w}{d}\right)^3 F(d), \tag{3.32}$$

where s denotes the skewness of the probability distribution, defined by:

$$s \equiv \frac{1}{w^3}\int_{-\infty}^{\infty} z^3 f(z)\mathrm{d}z.$$

The maximum value of s is 1.285 for the 1600 nm sample (see Fig. 3.4). In a parallel plate configuration, this leads to $\Delta F_{PT} \approx 18.55(w/d)^3 F(d)$. This means that the perturbative

contribution has meaning if $d > 4w$. The minimum separation distance d_0 depends on the scale L. It has turned out that even for small $L \approx 1\mu$m this condition is usually met. [98] Therefore it is justified to make the important statement that the perturbative contribution has physical meaning up to the point of contact between the interacting bodies.

The relative error due to the assumption that each peak contributes independently is determined by the condition of its applicability; the distance between the peaks must be sufficiently large: $l(d_1) \gg d$. This error is

$$\Delta F_{PFA} \approx (d/l) F_{PFA}. \tag{3.33}$$

As we mentioned before, d_1 must be chosen in such a way that $l \gg d$. One way to do this is $d_1 \equiv 3w$. This definition leads to the values of l listed in table 3.1. Similarly, we could define d_1' as $3w$. However, the contribution of the troughs, $F'_{PFA}(d)$, is always small. It is included only for the sake of generality.

In Fig. 3.10 the result of our approach (Eq. (3.22), the continuous (blue) line) is compared to measured force data (from Ref. [67], the open (red) circles), which were obtained with an AFM setup. The same figure includes the result for a smooth surface (Eq. (3.4), the dashed (purple) lines) and that of the PFA for the roughness correction. The latter is given simply by

$$\mathcal{F}_{PFA}(d) = \int_{-d_0'}^{d_0} \mathrm{d}z f(z) F(d-z), \tag{3.34}$$

the results of which are indicated by the dashed (green) lines in Fig. 3.10. Note that this expression is also singular at $d = d_0$.

In order to clarify the comparison between measured force data with errors and theoretical predictions as shown in Fig. 3.10, we would like to re-emphasize the distinction between the experimental and statistical error in d_0. The values Δd shown in Fig. 3.10 are the *experimental* uncertainties which account only for a *fixed lateral position of the surface profiles with respect to each other*. This is important because the error in d_0 dominates the error in the separation distance d, and at short separations it also dominates the uncertainty in the Casimir force. This is estimated from the relation

$$\Delta F_{Cas}(d) \approx F_{Cas} \sqrt{2.5 \left(\frac{\Delta d_0}{d}\right)^2 + \left(\frac{\Delta \kappa}{\kappa}\right)^2}. \tag{3.35}$$

The approximate factor 2.5 can be understood from the fact that $E(d)$ scales approximately as $E(d) \propto d^{-2.5}$. [100] The Casimir force was measured with an AFM setup. [67] The relative error in the spring constant κ of the cantilever beam is approximately $\Delta\kappa/\kappa \approx 3\%$. The

values for d_0 and their respective uncertainties have been established from electrostatic calibration and were taken from Ref. [98]. These uncertainties are denoted by error bars through some of the measurements in Fig. 3.10.

The insets of Fig. 3.10 show the different contributions to the solid lines in the main graphs: curve 1 (black) is force without roughness from Eq. (3.4) (the "zeroth order" perturbative contribution), curve 2 (red) is the peaks' contribution (Eq. (3.24)), and curve 3 (blue) is the second perturbative contribution (Eq.(3.23)). The contribution of the troughs, $F'_{PFA}(d)$ (Eq. (3.25)) is always several orders of magnitude smaller than the second smallest contribution, the second order term in $F_{PT}(d)$ in Eq. (3.23). Therefore it is not included in these plots.

In each of the three samples in Fig. 3.10, the dashed and the solid line overlap near contact ($d \sim d_0$), because the contribution of the peaks is evaluated with the PFA. This contribution decreases very fast with d, as the (red) curve labeled as 2 in the inset indicates. This is due to their small area of interaction. This is the dominant contribution near contact for the two roughest samples in Fig. 3.10a and 3.10b. For the other sample, the lower value of d_0 allowed the Lifshitz formula to dominate the other contributions. Still, also in this case the peaks contribute considerably near $d = d_0$. A few nm away from contact, the second order perturbative correction (represented by the (blue) curve labeled as number 3 in the inset) starts to become significant. The PFA corresponds to the low wavenumber limit in this contribution. [68, 69] Therefore it should always dominate the PFA at separations where the contribution of the peaks is negligible. It clearly does for the rougher samples: the solid (blue) line lies above the dashed (green) line in Figs. 3.10a and (b). For the 800 nm sample (Fig. 3.10c) the contribution from beyond the small wavenumber limit is the smallest; it is barely discernible on the graph.

The results of this model are in agreement with measurements for gold samples, unlike perturbation theory, which failed to explain the data. [67] On the other hand, naive application of the PFA via Eq. (3.34) also reproduces the the data from Ref. [67] within error. Scattering theory accounts for the non-additivity of the Casimir force and the PFA assumes that it is additive. This indicates that the experiment in Ref. [67] was not sensitive to the effect of the non-additivity. This is not to say that non-additivity effects are insignificant in general. Indeed, recently significant non-additivity effects have been reported in different contexts, see e.g. Ref. [112]

The theoretical and experimental results can also be presented in a different way: the absolute value of the relative difference is plotted in Fig. 3.11 and compared to the error. The open (red) circles represent the difference with the "naive PFA" of Eq. (3.34), and the blue asterisks show the difference with the model of Eq. (3.22). The solid (green) line represents the relative error from Eq. (3.35). In Fig. 3.11a, which shows the results for the 1600 nm sample, the result of our model , Eq. (3.22), seems closer to the experimental data than the naive PFA. However, the difference is less than two standard deviations.

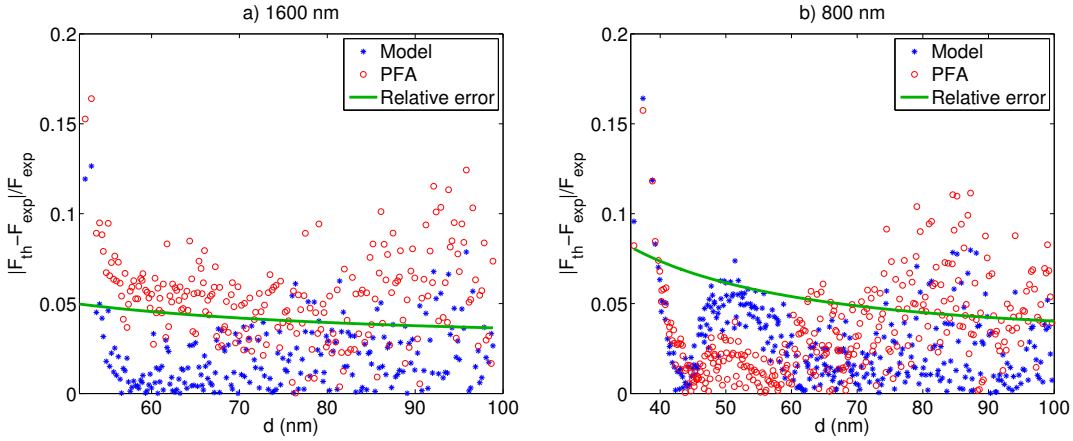

Figure 3.11: *Relative difference between theoretical and experimental results. The solid (green) line represents the relative experimental error from Eq.* (3.35)*. It is assumed that the sphere in the AFM setup has a* fixed *lateral position with respect to the plate. The (red) open circles are comparisons to the naive PFA of Eq.* (3.34)*, and the (blue) asterisks show the difference with the model of Eq.* (3.22)*.*

This difference is even less pronounced for the 800 nm sample, displayed in Fig. 3.11b. In both cases there is a difference of about 15% at short distances ($d \approx d_0$) which exceeds the vertical error. The apparent discrepancy can be accounted for by the horizontal error in Fig 3.10, Δd_0. It should be kept in mind that the force decreases rapidly near contact, so that a small horizontal shift can give rise to a fairly large difference in the vertical direction.

If the peaks are modeled as half spheroids, the effect of this shape ($\sim$ 5 %) is still within the experimental error. (See section 3.4). For conically shaped peaks the effect is 15 % which is not within the vertical error. This effect is compared to calculations in other geometries, where the value of d_0 is exactly the same in each case. Therefore it is independent of the experimental uncertainty in d_0, and most likely not responsible for the 15% difference in Fig 3.11a. Moreover, as we found in section 3.4, conically shaped peaks cannot be reconciled with both the AFM data and the known value of the correlation length. For this reason, cones can be ruled out as a geometry to describe peaks on gold surfaces. However, due to the uncertainty in d_0, the measurements of Ref. [67] by themselves do not entirely rule out a 15 % effect due to the shape of the peaks.

3.7 Conclusions

We have developed a reliable method to include roughness effects in estimations of the Casimir force at short separations, where perturbation theory fails. Statistical analysis of AFM topography scans has taught us that the surface's height fluctuations can be

asymptotically fitted to a Gumbel distribution. We have shown that the contribution of high peaks on a rough surface can be taken into account with the PFA. On the other hand, asperities of height $\sim w$ can be evaluated perturbatively. Because the peaks are sufficiently far apart on the scale of the separation, their contributions to the Casimir force are statistically independent.

It has been established that the peaks contribute significantly to the Casimir force, particularly near contact where $d \approx d_0$. The high peaks not only dominate the force, but they also shift the minimum separation distance from 0 to d_0. To a large extent this gives rise to the scaling of the force observed experimentally: the shift of the singularity in the Lifshitz formula makes both experimental and theoretical curves singular at $d \approx d_0$ and unphysical below d_0. The inclusion of contact between the bodies appears to be a crucial aspect of the roughness correction to the Casimir force.

We have presented detailed calculations of the influence of the curvature of the peaks by modeling them as half spheroids, but this has a marginal effect on the force as a whole. The reason for this is that their contribution is significant only near contact (where $d - d_0 \ll \xi$), and decreases rapidly with d due to their small area of interaction. In this near contact limit the PFA is valid, so that we can neglect the curvature of the peaks. On the other hand, modeling the peaks as cones cannot reproduce the correlation length from the information that the AFM data provides about the lateral sizes of the peaks. It can be concluded that cones are not a proper geometry to describe peaks on gold surfaces. Moreover, it produces an effect that does not seem to be well supported by experiment, even though it cannot be entirely ruled out either.

We have calculated the Casimir force between relatively smooth surfaces, which is potentially useful for direct bonding applications. It was found that the Casimir force is an order of magnitude higher than the force between rougher surfaces, because the lower value of the contact distance allowed lower separations. Possibly, higher Casimir forces could be achieved between congruous bodies. In such a case, this approach for the roughness correction could be combined with numerical methods (e.g. FDTD [105]) to account for the geometry of the system. Such a calculation would be computationally challenging, because it involves multiple scales.

It has also turned out that naive application of the PFA described by Eq. (3.34) gives a result close to that of our approach and hence is also in good agreement with the experiment. Perturbation theory accounts for the non-additivity of the Casimir force whereas the PFA assumes that it is additive. The experiment in Ref [67] was not sensitive to the effect of non-additivity, because of the uncertainties associated with contact mode measurements. (See Eq. (3.35)). Since this thesis is primarily concerned with the significance of the Casimir force at short separations for MEMS applications, the result of this chapter can be applied to implement the effect of surface roughness on the Casimir force in an experimentally relevant way. This will be done in the next two chapters.

Chapter 4

Dynamics of MEMS: the conservative case[1]

4.1 Introduction

In earlier investigations of the effect of the Casimir or van der Waals forces on the dynamical behavior of nanoscale electrostatic actuators, roughness was either ignored or only weak roughness was considered [46, 47]. In some cases tabulated optical data were taken into account. [48–50, 55, 65, 113] Advances made in the measurement and theoretical understanding of Casmir forces over the last 10 years allow today a more detailed study of MEMS made of real material surfaces. [9] In this chapter, we will explore the actuation dynamics of microswitches made of real materials (with a definite measured optical response [64, 99, 114] and characterized by some degree of nanoscale roughness). Both electrostatic and Casimir forces, which counteract an elastic restoring force (see Fig. 4.1a), will be included. The model from chapter 3 [102, 115] will be applied to account the effect of surface roughness on the Casimir force, and the same principle will be applied to electrostatic forces. Note that although electrostatic forces can be switched off if no potential is applied, Casimir forces will always be present to influence the actuation dynamics.

This chapter is organized as follows: after the introduction the model of chapter 3 will be applied to the electrostatic force. Next we will investigate Casimir actuated MEM systems with rough surfaces without the electrostatic force. Before the conclusions the electrostatic force will be included, which introduces the applied voltage as an independent parameter of the problem. Throughout this chapter it will be assumed that energy is conserved. The case where some energy loss and gain are allowed is treated in chapter 5.

It will be shown that a stable center equilibrium, around which periodic solutions exist, is accompanied by an unstable saddle equilibrium if the spring constant κ is large enough. However if κ is lowered, the center and saddle will merge into an unstable center-saddle equilibrium. The rougher the surface, the larger the value of κ at which this so called center-saddle bifurcation occurs. If the electrostatic force is included, the critical equilibria join in the limit of small voltages and large κ. As a function of the parameter values, this limit is reached faster in the rough case than in the flat case. This appears to be due to

[1] This chapter is based on W Broer, G Palasantzas, J Knoester, and V B Svetovoy *Significance of the Casimir force and surface roughness for actuation dynamics of MEMS* Phys. Rev. B **87,** 125413 (2013)

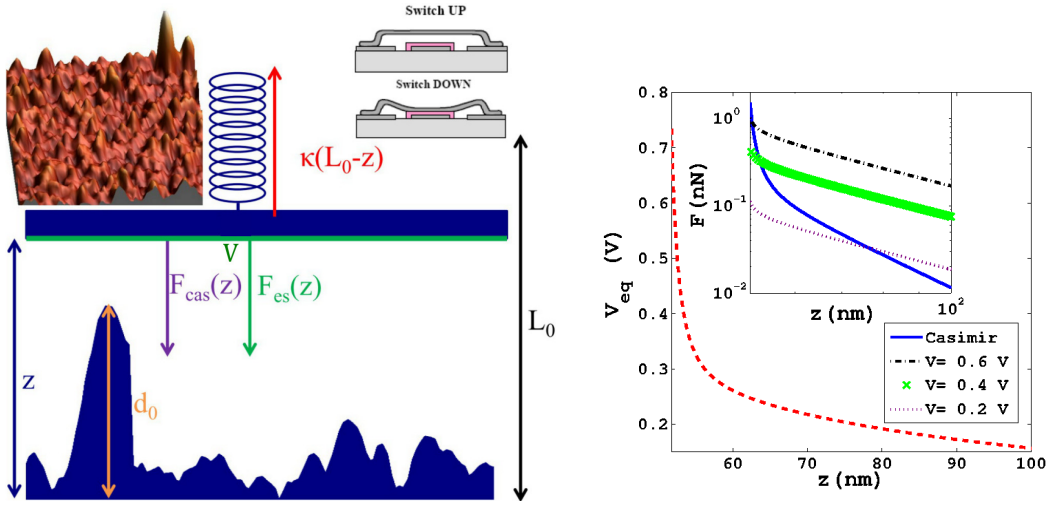

Figure 4.1: *(a) Schematic of the MEM system. The spring tries to move the oscillator toward the initial separation L_0. The contact distance d_0 is the maximum height of the asperities on a rough surface. (b) In the inset, the Casimir force from Eq.* (4.1) *for gold surfaces is compared to the electrostatic force between rough surfaces from Eq.* (4.6) *for several values of the applied voltage V. The quantity V_{eq} indicates to what voltage the Casimir corresponds after equating the Casimir force from Eq.* (4.1) *to the electrostatic force from Eq.* (4.6)*. In this case the r.m.s. $w = 10$ nm and the contact distance $d_0 = 50.8$ nm.*

the smaller interaction area of a rough surface.

4.2 Roughness correction to the electrostatic force

It has been shown [102,115] in chapter 3 that the disagreement between the experiment [67] and the theory describing roughness perturbatively [68, 69] can be resolved by taking into account rare high peaks on rough surfaces. These high peaks can be described by "extreme value statistics" as follows from a statistical analysis of AFM topography data for gold films. [98, 102, 115] Indeed, recently there has been more awareness of the importance of extreme value statistics for the analysis of rough surfaces. [116] The Casimir force between rough surfaces can be written as:

$$F_{Cas}(z) = F_{PT}(z) + F_{peaks}(z), \tag{4.1}$$

where z no longer denotes the random variable of the height fluctuations as in chapter 3, but rather the coordinate of the oscillator. The term $F_{PT}(z)$ in Eq. (4.1) denotes the Casimir force between rough surfaces from Ref. [68], which includes a "zeroth" order contribution corresponding to flat surfaces and a perturbative roughness correction $\sim (w/z)^2$, where w is the root-mean-square roughness. The term $F_{peaks}(z)$ represents the contribution of high

peaks, which is associated with the aforementioned extreme value statistics. It is important to note that $F_{Cas}(z)$ is singular at the distance upon contact, [98,102,115] ($z = d_0$) which is the real minimum separation due to surface roughness. (See chapter 3) It is assumed that the contributions of high peaks are independent of each other, an approximation justified by the large horizontal distance between them. This distance is large because such peaks are statistically rare events. [102, 115] The ellipsometry measurements for gold samples reported in Ref. [99] were used as optical data.

The roughness correction to the electrostatic force can be obtained in the same way as was done in chapter 3 for the Casimir force: the heights of the surface comparable to w can be taken into account perturbatively, whereas the contribution of high peaks can be approximated by treating each peak independently. This approximation is justified by the large distance between the high peaks, because such peaks are statistically rare events. The perturbative roughness correction to the electrostatic force is based on an analysis for isotropic roughness, [46, 47, 65] as is the case for the gold films considered here [99] which are grown under non equilibrium conditions. This correction starts by modeling the surfaces as a capacitor with capacitance:

$$\langle C(z)\rangle = \frac{A\varepsilon}{z}\Big\{1 + \frac{2(2\pi)^4}{A}\int_0^{k_c}\Big\langle|\tilde{h}(\mathbf{k})|^2\Big\rangle\big(k^2 + \frac{\pi}{z}\coth(kz)\big)\mathrm{d}\mathbf{k}\Big\} \tag{4.2}$$

where the first and second terms correspond to flat surfaces and a second order perturbative correction, respectively, and A denotes the surface area of each plate. The quantity k_c represents the wavenumber corresponding to a lower lateral roughness cutoff of the order of the inter-atomic distances ($\sim$ 4 Å for gold) . For power law or self affine random roughness a suitable model for the power spectrum $\Big\langle|\tilde{h}(\mathbf{k})|^2\Big\rangle$ to perform calculations with is given by [117]

$$\Big\langle|\tilde{h}(\mathbf{k})|^2\Big\rangle = \frac{A}{(2\pi)^5}\frac{w^2\xi^2}{(1+ak^2\xi^2)^{1+H}}. \tag{4.3}$$

Here ξ denotes the correlation length, a represents the self-affine roughness parameter which can be found by solving the algebraic equation: $a = 1/(2H)[1-(1+ak_c^2\xi^2)^{-H}]$. For the gold films considered here [99] the roughness exponent has the value $H = 0.9$.

The electrostatic force including the second order perturbative roughness correction can be written as

$$F_{pe}(z) = -\tfrac{1}{2}V^2\frac{\mathrm{d}\langle C(z)\rangle}{\mathrm{d}z}, \tag{4.4}$$

where the average capacitance $\langle C(z)\rangle$ is given by Eq. (4.2) and V denotes the applied voltage. Equipotential planes are expected to be a valid approximation at separations below 100 nm. Statistical deviations from this approximation, known as potential patches, typically play a role at separations of the order of a few hundred nanometers up to a few

micrometers. [39, 88, 118] Now the contribution of the high peaks in the surface can be approximated by a sum of separate contributions of each peak as it was done in chapter 3 for the Casimir force. For this purpose we start with the electrostatic force between flat surfaces:

$$F_e(z) \cong \frac{\varepsilon_0 A V^2}{2z^2}. \tag{4.5}$$

For the roughness statistics we can use the same AFM topography data with the same statistical analysis as in chapter 3. Therefore the electrostatic force between rough surfaces becomes

$$F_{es}(z) = F_{pe}(z) + \int_{d_1}^{d_0} f(d)[F_e(z-d) - F_e(z) + dF_e'(z) - \tfrac{1}{2}d^2 F_e''(z)]\mathrm{d}d \tag{4.6}$$

where $f(d)$ denotes the probability density function. The height $d_1 = 3w$ is the separation above which $f(d)$ can be fitted to a Gumbel distribution [102, 115] and d_0 is the height of the highest asperity (see Fig. 4.1a). It must be noted that the expression in Eq. (4.6) is also singular at $z = d_0$.

Figure 4.1b shows the relative strength of electrostatic and Casimir forces for various potentials between real nanoscale rough Au-Au surfaces. The Casimir force becomes significant for separations $z < 100$ nm and overcomes the electrostatic force rather rapidly as the applied potential drops below 1 V (a regime typical for MEMS) and separations close to distance upon contact due to surface roughness. Indeed, the potential $V_{eq}(z)$ where $F_{Cas}(z) = F_{es}(z)$ increases rapidly toward smaller separations, which shows that the Casimir force corresponds to increasing values of the applied voltage V. These results clearly show that below 100 nm Casimir forces can strongly influence the actuation dynamics.

4.3 Actuation dynamics of MEMS

Modeling a MEMS as a classical mass-spring system has been well established. [61] Let the separation z depend on time and satisfy the following differential equation:

$$m\frac{\mathrm{d}^2 z}{\mathrm{d}t^2} = \kappa(L_0 - z) - F(z), \tag{4.7}$$

where $F(z) = F_{Cas}(z) + F_{es}(z)$ represents the total surface force, κ is the spring constant, and L_0 is the distance between bodies if no external force is present, $F(z) = 0$. The effective mass m merely rescales the equation (4.7). For our calculations we used as an example a resonance frequency $\omega_0 \equiv \sqrt{\kappa/m} = 300 \cdot 2\pi$ krad/s which is typical for a wide

variety of commercial resonators, e.g. tapping mode AFM cantilevers and other doubly clamped beam MEMS [119]. This frequency is kept constant, whereas κ is varied and used as a control parameter. A parallel plate geometry with a surface area of $10\times$ 10 μm^2 was assumed for the computations of the Casimir and electrostatic forces.

The solutions of Eq. (4.7) can be investigated with a *phase portrait*, [120] i.e. a plot of z versus $z'(t)$. Studies of the influence of the Casimir force for nanoscale electrostatic actuators with flat, perfectly conducting electrodes showed that their phase portraits exhibit periodic orbits around a center equilibrium, and an orbit that passes through an unstable saddle point. [59,60] These studies were extended to the influence of weak roughness only. [46,47]

Consider first the case of zero electrostatic force, $F_{es}(z) = 0$. The goal is to find out under what conditions the oscillator described by Eq. (4.7) can return to its original position; i.e. for what parameter values periodic solutions exist. *The existence of periodic solutions indicates that the spring is strong enough to prevent stiction.* If the spring constant is large enough, the stable center around which periodic solutions exist will be accompanied by an unstable saddle point equilibrium. [57–60] If the spring constant becomes lower, the center and saddle point will merge into an unstable "center-saddle" point. For an even lower value of κ there are no equilibria at all. This is an example of what is known as a saddle-node bifurcation. [120]

In order to understand for what values of κ such equilibrium points are available we introduce the following bifurcation parameter

$$\lambda_{cas} \equiv \frac{F_L(L_0)}{\kappa L_0}, \tag{4.8}$$

where $F_L(L_0)$ denotes the Casimir force given by the Lifshitz formula [1,2] (for flat surfaces) at $z = L_0$. This ratio of the minimal Casimir force and the maximal elastic restoring force represents the relative importance of one force compared to the other. In an equilibrium the total force given by Eq. (4.7), is zero: $F_{tot}(z) = 0$. This case yields $\lambda_{cas} = (1 - z_s/L_0)F_L(L_0)/F_{cas}(z_s)$, where z_s denotes the locus of the stationary points.

The results are plotted in Fig. 4.2a. As one can see the rougher the sample (i.e. the higher the value of the contact distance [98] d_0), the higher the spring constant must be to get equilibria and periodic solutions. The maximum of λ_{cas} decreases with d_0. The *position* of this maximum changes only slightly under the influence of random roughness: from $0.78L_0$ for a flat surface to $0.81L_0$ for the roughest sample. This is because at these separations the roughness effect is small (perturbative) and does not drastically change the force. To clarify the meaning of Fig. 4.2a, the general solution, represented by the phase portrait, is plotted for three different values of the spring constant, for the roughest sample (with $d_0 = 50.8$ nm). Fig. 4.2b shows the case where the spring constant is large enough for the bifurcation parameter to be below its maximum value. In this case there

are two equilibria: the stationary point closest to L_0 is a (stable) center around which periodic solutions (closed curves) exist. Since the system considered here is conservative (Hamiltonian), the phase portraits can be obtained by plotting the level curves of the total energy. The solutions of Eq. (4.7) are periodic if the amplitude stays below a value of approximately $0.4L_0$. The shift of the minimum separation due to roughness from zero to d_0 prevents periodic motion if the total energy is too high. In Fig. 4.2c the value of κ has been chosen such that it corresponds to the maximum value of λ_{cas} in Fig. 4.2a. In this case there is only one equilibrium, known as a center-saddle point, [121] which are always unstable. There are no periodic solutions in this case. If the value of the spring constant is lowered further, no equilibria are available anymore. The spring is too weak to counterbalance the attractive Casimir force. The solution for this case is plotted in Fig. 4.2d.

Although neglecting the electrostatic force can provide some insight, this force must also be taken into account. If we consider the presence of the electrostatic force only, $F_{es}(z) \neq 0$ and $F_{Cas}(z) = 0$, we can define an additional bifurcation parameter for the electrostatic force:

$$\lambda_{es} \equiv \frac{\varepsilon_0 A V^2}{2\kappa L_0^3} = \frac{F_e(L_0)}{\kappa L_0}. \tag{4.9}$$

Similarly to the previous case, this is the ratio of the minimum electrostatic force and the maximum elastic force, which is a measure of the relative importance of one force compared to the other. In this case it holds that $\lambda_{es} = F_e(L_0)/F_{es}(z_s)(1 - z_s/L_0)$, which is obtained from the condition $F_{tot} = 0$. However, it must be stressed that this case is a rather artificial one, because the Casimir force cannot be shut down (since it stems from quantum mechanical uncertainty). Results for this case are qualitatively similar to the previous one, but the roughness effect is less pronounced because the electrostatic force depends more weakly on the separation distance than the Casimir force.

In the more general case $F_{es}(z) \neq 0$ and $F_{Cas}(z) \neq 0$, the stationary points z_s satisfy the following equation obtained from the condition $F_{tot} = 0$:

$$1 - \frac{z_s}{L_0} - \frac{F_{cas}(z_s)}{F_L(L_0)}\lambda_{cas} - \frac{F_{es}(z_s)}{F_e(L_0)}\lambda_{es} = 0, \tag{4.10}$$

where λ_{cas} and λ_{es} are defined by Eqs. (4.8) and (4.9) respectively. Eq. (4.10) is an implicit function of two variables, plotted in Fig. 4.3a for both the idealized case of flat surfaces and the roughest surface with $d_0 = 50.8$ nm. The graph for the case of flat surfaces encloses the one for the rough surface case. This indicates that, similarly to the previous case, surface roughness increases the minimum value of the spring constant required to compensate for both the electrostatic and Casimir forces. However in this case this value further increases with the value of the applied voltage V, as indicated by the contour plots for the rough case in Figs. 4.3b and 4.3c. The phase portraits are similar to those in Fig.

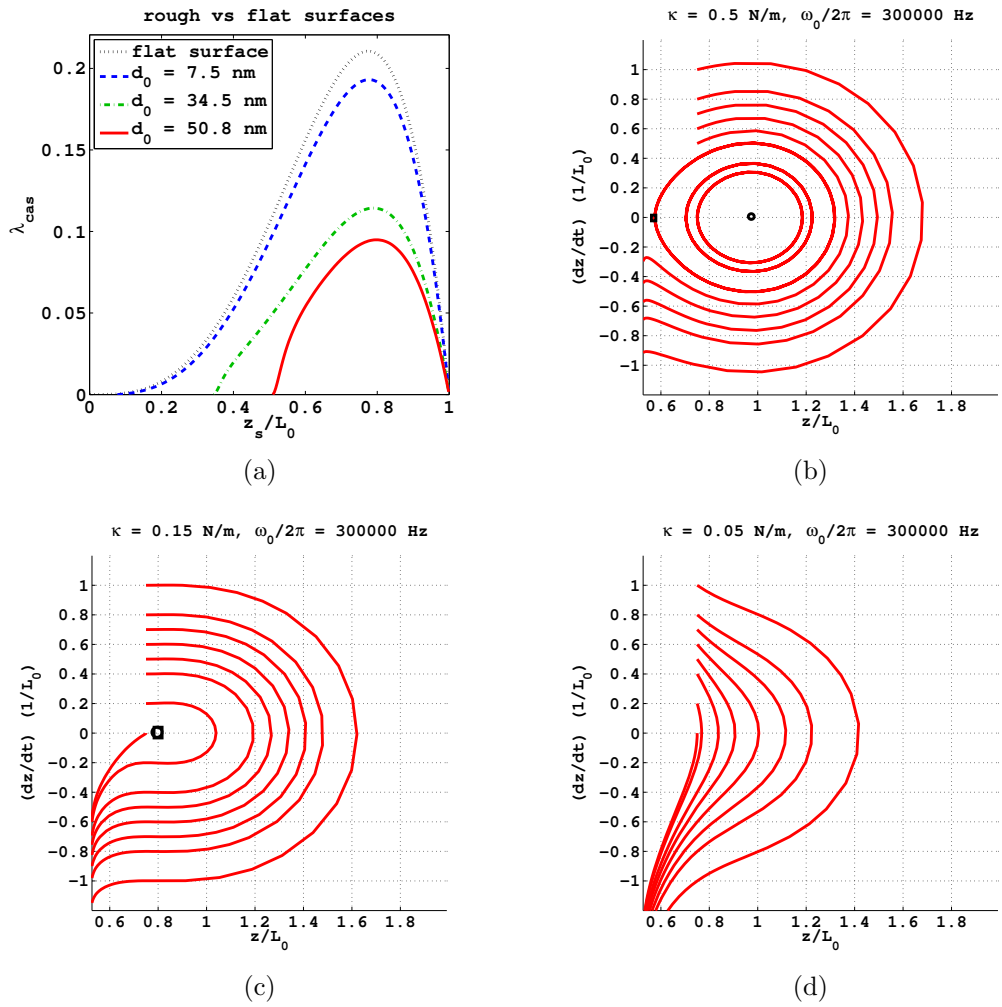

Figure 4.2: *(a) Bifurcation diagram of Casimir actuated MEMS for various rough surfaces, each of which is associated with a different value of the contact distance d_0. The value of the initial separation $L_0 = 100$ nm. (b) Phase portrait for the surface with $d_0 = 50.8$ nm. The (black) circle and the (black) square indicate the positions of the center and saddle point equilibria, respectively. In this case, the spring constant is high enough for periodic solutions to exist. (c) This phase portrait corresponds to the maximum of the solid (red) curve in Fig. 4.2a. In this case there is only one (unstable) equilibrium, and there are no periodic solutions. (d) Phase portrait corresponding to a point above the maximum of solid (red) curve in Fig. 4.2a. There are no equilibria in this case.*

4.2: the only difference is that the distance between the center and saddle point is smaller than in Fig. 4.2a, since $V \neq 0$ in this case. From Fig. 4.3b it can be concluded that this distance decreases with V since $\lambda_{es} \propto V^2$. The critical equilibrium points at which stiction occurs are characterized by the conditions $dU/dz = 0$ and $d^2U/dz^2 = 0$, where U denotes the total potential energy of the system (i.e. $F_{tot}(z) = -dU/dz$). See e.g. Refs. [57],

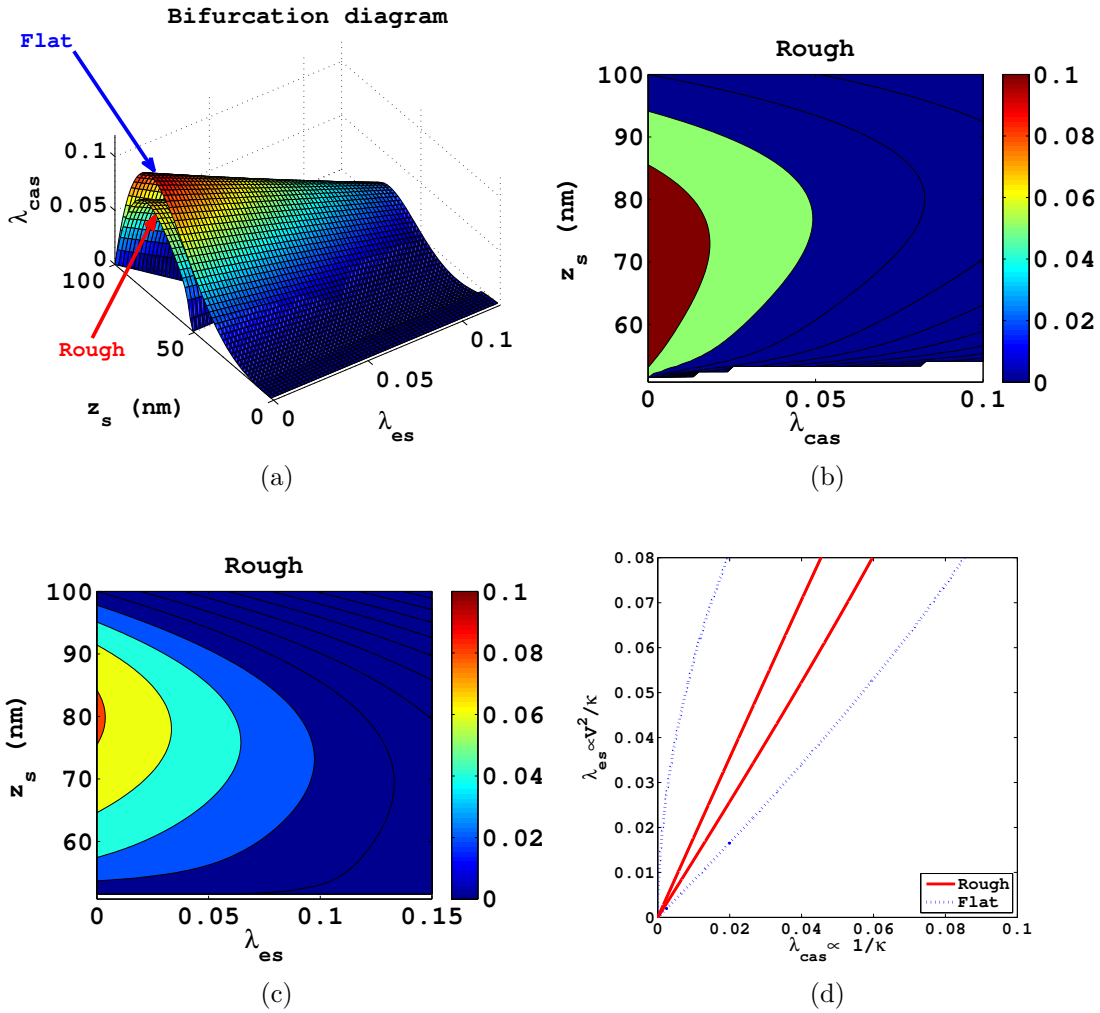

Figure 4.3: *(a) 3D Bifurcation diagram for a MEMS actuated by both Casimir and electrostatic forces for both a rough and a flat surface. The innermost graph represents the rough case. (b) Side view of the innermost graph of Fig. 4.3a (c) Top view of the innermost graph of Fig. 4.3a. (d) Two parameter bifurcation diagram under the conditions of Eqs.* (4.10) *and* (4.11)*. In the origin the equilibria join.*

[59], or [61]. Hence Eq. (4.10) must be combined with its derivative with respect to z at stationary point z_s, which is also set to zero:

$$-\frac{1}{L_0} - \frac{F'_{cas}(z_s)}{F_L(L_0)}\lambda_{cas} - \frac{F'_{es}(z_s)}{F_e(L_0)}\lambda_{es} = 0, \tag{4.11}$$

which corresponds to $d^2U/dz^2 = -dF_{tot}/dz = 0$. Eqs. (4.10) and (4.11) form a system of two equations with three unknowns. Note that Eqs. (4.11) and (4.10) can be considered a

system of linear equations with solutions

$$\lambda_{cas} = F_L(L_0)\frac{F_{es}(z_s) + (L_0 - z_s)F'_{es}(z_s)}{D(z_s)} \qquad (4.12)$$
$$\lambda_{es} = F_e(L_0)\frac{F_{cas}(z_s) + (L_0 - z_s)F'_{cas}(z_s)}{D(z_s)}$$

where $D(z_s)$ denotes the determinant

$$D(z_s) = L_0(F_{es}(z_s)F'_{cas}(z_s) - F_{cas}(z_s)F'_{es}(z_s)). \qquad (4.13)$$

Eliminating z_s from Eqs. (4.12) yields a relation between the bifurcation parameters λ_{cas} and λ_{es}. This relation is plotted in Fig. 4.3d. Since $\lambda_{es} \propto V^2/\kappa$ and $\lambda_{cas} \propto 1/\kappa$ the origin of this graph corresponds to high spring constants and low voltages, i.e. to the situation that the spring is strong and the device is shut down (i.e. V decreases such that $\lambda_{es} \ll 1$). In Fig. 4.3d it can be seen that the equilibria join in the origin both for the flat and the rough case. This corresponds to the ideal case where only periodic motion exists and stiction is of no concern. It turns out that this limit is reached *faster* as a function of the parameter values in the rough case than in the flat one. On the other hand, stable and unstable equilbria are closer in the rough than in the flat case. It should be kept in mind, however, that the rough case in Fig. 4.3d corresponds to the roughest sample available with $d_0 = 50.8$ nm. Presumably the optimum in terms of preventing stiction lies somewhere between these two cases (e.g. a contact distance between 20 nm and 30 nm).

4.4 Conclusions

It may seem surprising that a flat surface is not optimal in terms of preventing stiction, but the reason for this is that the shift of the minimum separation from zero to d_0 prevents both the Casimir and electrostatic forces from becoming too large. In other words, there is a trade-off between two effects: on one hand random surface roughness requires a higher spring constant for equilibria to exist and puts the stable and unstable equilibria closer together, and on the other hand it prevents the surfaces from reaching too short a separation, reducing both the Casimir and electrostatic forces.

Using measured material and surface properties and realistic device dimensions, we studied the effect of the Casimir-Lifshitz force on the actuation dynamics of MEMS. It has turned out that this force is equivalent to a voltage between 0.2 and 0.6 V at separations below 100 nm, which is comparable to the electrostatic force typically used to actuate MEMS. We have shown that random roughness has an overall strong effect on the availability of equilibria of MEMS oscillators: the rougher the surface, the lower the maximum values of the bifurcation parameters, and hence the higher the spring constant must be in

order for equilibria to exist. Finally, the shift of the minimum separation due to surface roughness moves the stable center curve closer to the unstable saddle point curve in the bifurcation diagram as a function of the stationary points. However, there is a trade-off: a MEMS of which the actuating components have rough surfaces benefits more from a strong spring constant than one with a flat surface. This is because surface roughness brings the two equilibrium points closer together in terms of the separation, but it prevents the surface forces that give rise to stiction from becoming too large. Most likely the optimum lies somewhere in between a flat surface (with $d_0 = 0$) and a very rough surface (with $d_0 \approx 50$ nm). Our analysis applies to motion in vacuum or dilute gases, where friction losses can be ignored. Qualitatively, the center equilibrium in Fig. 4.2b becomes an inward 'sink' spiral in the presence of friction. [122] A more detailed analysis of the effect of hydrodynamic drag forces [123–125] present in air will be presented in a future study. Apart from energy loss through e.g. friction or hydrodynamic forces, some energy gain can be introduced (e.g. in the form of periodic forcing). This case is theoretically more involved since the explicit time dependence introduces an additional degree of freedom. See chapter 5 for more details.

Chapter 5

Chaotic motion of a Casimir oscillator[1]

5.1 Introduction

At separation distances larger than 100 nm, the spatial gradient of the Casimir force can be measured very precisely with a MEMS oscillator within a linearization approximation. [126] However, at separations below 100 nm, the nonlinearity of the Casimir force has been experimentally demonstrated to have a qualitative effect on the motion of MEM systems. [38] Moreover, at these short separation ranges, the Casimir force is large enough to be a formidable obstacle to achieving stable actuation. In such a case, both the influence of the permittivities of the materials [2, 9, 12] and that of surface roughness [67] must be taken into account in order to come to a realistic evaluation of the Casimir force. This is crucial for further understanding and controlling the actuation dynamics of the system in order to prevent pull-in instabilities.

Earlier works on the actuation dynamics of MEMS under the influence of Casimir forces usually concern conservative systems (see chapter 4) [49,50,56–58,65,66,127] or autonomous systems with damping [122]. The non-autonomous case, which is closer to an experimental MEMS oscillator setup, is in the theoretical analysis typically treated for ideal metals [128], sometimes with an expansion of the Casimir force in the oscillator's coordinates. [38, 129] The higher order terms in such polynomial expansions give rise to additional zeros of the conservative force equation, which do not correspond to physical equilibria. [129] So far there has been no theoretical work that takes the optical response and surface roughness into account for forced Casimir oscillators. Explicit time dependence, e.g. through periodic forcing, constitutes an additional degree of freedom compared to the autonomous case.

A damped, driven oscillator with some form of nonlinearity is one of the simplest systems in which chaotic motion can occur. [130] Chaos or chaotic motion can be understood simply as sensitive dependence of the motion on its initial conditions. [131] The conservative system discussed in chapter 4 is nonlinear, but it does not have enough degrees of freedom to exhibit chaotic motion. This physically observable effect introduces a considerable risk of stiction, and therefore it is highly relevant for MEMS applications. Moreover,

[1] This chapter is based on W Broer, G Palasantzas, J Knoester, H Waalkens and V B Svetovoy, *Suppression of chaos assisted stiction in Casimir oscillators due to surface roughness*, in preparation

chaotic motion of MEMS components is undesirable, even if stiction could somehow be avoided.

In this chapter we investigate under which conditions chaotic motion occurs in a damped driven Casimir oscillator. The effects of both surface roughness and the optical response are included in an experimentally relevant way. More specifically, ellipsometry data of gold films were used as input for the force calculations, which is required for a quantitative evaluation of the Casimir force. [99] In order to account for the effect of surface roughness, the result of the model [102, 115] from chapter 3 was used.

5.2 The Melnikov method for a Casimir Oscillator

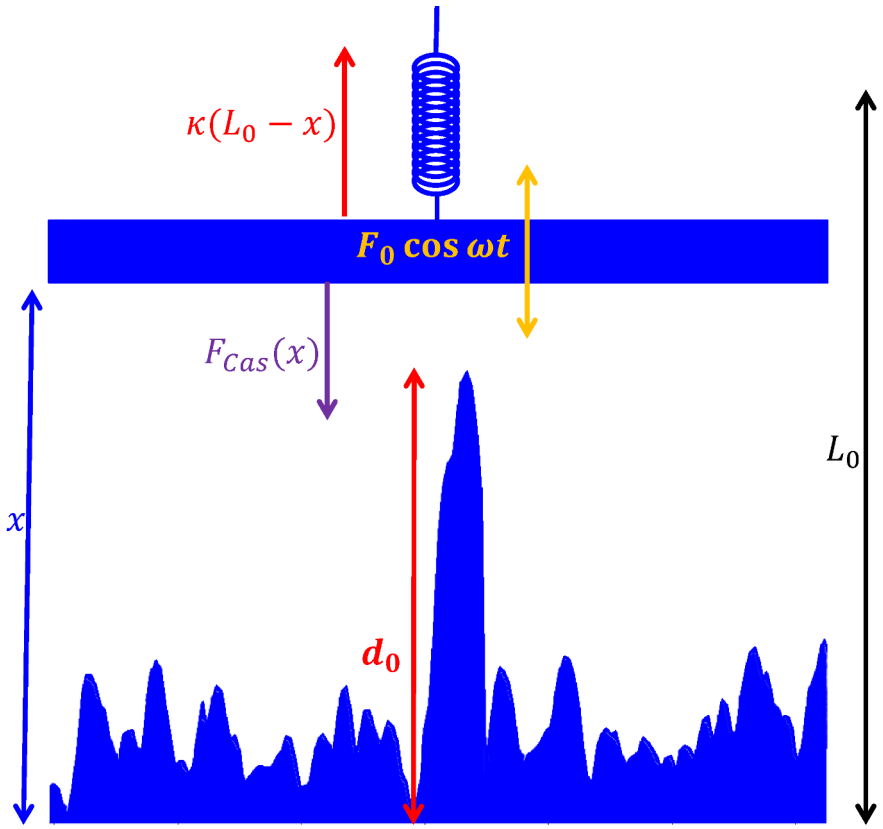

Figure 5.1: *Schematic of the system to clarify the meaning of the parameters. Some energy dissipation and gain are allowed through damping and driving, respectively.*

Modeling a MEMS/NEMS as a classical mass-spring system has been well established. [61] In the conservative case the equation governing the MEMS is

$$m\ddot{x} = \kappa(L_0 - x) - F_{Cas}(x), \tag{5.1}$$

where $F_{Cas}(x)$ denotes the Casimir force between rough surfaces [102, 115] and the coordinate of the oscillator must be beyond the contact distance d_0 [98], i.e. $x > d_0 \geqslant 0$. The case $d_0 = 0$ corresponds to flat surfaces. The other parameters in Eq. (5.1) are indicated in Fig. 5.1: m denotes the effective mass, κ is the spring constant and L_0 is the characteristic length scale of the problem. Throughout this chapter, the values we use for these parameters are: $L_0 = 100$ nm, m is known only implicitly through the natural frequency $\omega_0 \equiv \sqrt{\kappa/m} = 2\pi \cdot 300$ krad/s; and the spring constant $\kappa = 0.5$ N/m is large enough to prevent stiction for the conservative system even in the rough case, as was shown in chapter 4. [127] A parallel plate geometry is considered where the surface area of each plate is $10 \times 10\mu\text{m}^2$.

The Melnikov method introduces a perturbation on a conservative system. [130] In order to apply this method, Eq. (5.1) is written as a set of coupled first-order differential equations:

$$\begin{aligned} \dot{z_1} &= \tfrac{z_2}{\omega_0 L_0} \\ \dot{z_2} &= \tfrac{1}{\kappa L_0}(\kappa(L_0 - z_1) - F_{Cas}(z_1)), \end{aligned} \tag{5.2}$$

where Eq. (5.1) has been rescaled for numerical convenience. Eq. (5.2) can be written in short-hand notation as

$$\dot{z} = f(z), \tag{5.3}$$

where z and $f(z)$ are two-dimensional vectors. Now in the case of a damped driven oscillator Eq. (5.2) becomes

$$\begin{aligned} \dot{z_1} &= \tfrac{z_2}{\omega_0 L_0} \\ \dot{z_2} &= \tfrac{1}{\kappa L_0}(\kappa(L_0 - z_1) - F_{Cas}(z_1) - \epsilon\gamma z_2 + \epsilon F_0 \cos\omega t), \end{aligned} \tag{5.4}$$

where γ and F_0 denote the damping and driving coefficients, respectively, and ω denotes the frequency of the forcing. These parameters will be varied in the bifurcation analysis presented here. The formal parameter $\epsilon = 1$ is included to indicate which terms are part of the first-order perturbation of the conservative system. The quantity γ is inversely proportional to the quality factor Q of the cantilever: $\gamma = m\omega_0/Q$. Damping can be neglected for very high $Q \sim 10^5$, but for more typical values $\sim 10^2$ or $\sim 10^3$ it should be included. [122] It is assumed here that the MEM system operates in clean and dry conditions: only intrinsic energy dissipation, [119] where some of the kinetic energy of the oscillator is converted into heat is considered here. Since it is assumed that the motion takes place in clean, dry conditions, capillary and hydrodynamic forces, which are expected to dominate under ambient conditions, will be ignored here. Eq. (5.4) can be abbreviated as

$$\dot{z} = f(z) + \epsilon g(z, t), \tag{5.5}$$

where $g(z,t)$ contains all terms that break energy conservation. The errors of the first-order perturbation are $O(Q^{-1})$ for the damping and $O(F_0/\kappa L_0)$ for the forcing. The latter dominates for typical values of F_0 [119] and is $\sim 3\%$, which is of comparable accuracy to the roughness model of chapter 3 [102]. Moreover, Melnikov's method turns out to be valid even for relatively large perturbations. [132]

In the conservative case, a stable center equilibrium is accompanied by an unstable saddle if the spring constant κ is large enough (See chapter 4). [127] The orbit in phase space which passes through the saddle is known as the homoclinic orbit. This orbit separates qualitatively different solutions of Eq. (5.1): outside it, there is no periodic motion and stiction will occur, but inside the presence of periodic solutions indicates that stiction is avoided and stable actuation is established. The homoclinic orbit is not a particular solution of Eq. (5.1), because a set of initial conditions uniquely determines a solution and hence it will never intersect with itself. However it can be approximated as one from the inside: let the location of the saddle z_s be known by numerically determining the zero of the second equation of the set (5.2) via e.g. Newton's algorithm. Since z_s is an equilibrium point, it would be an ill choice of initial conditions of Eq. (5.1). However, a point slightly to the right of z_s, i.e. $z_s + \delta$ with $0 < \delta/L_0 \ll 1$ can be used as a set of initial conditions for a numerical solver of ordinary differential equations (ODEs), e.g. Runge-Kutta algorithm. A spline interpolates the numerical result of chapter 3 and serves as an input for the ODE solver. The smaller the value of δ, the better the approximation of the homoclinic orbit will be. However, choosing too small a value is not efficient: in such a case the ODE solver will spend a considerable part of the simulation time close to the saddle equilibrium where it will not compute any contribution to the homoclinic orbit. Of course choosing too large a value will not provide a good approximation of the homoclinic orbit. An optimal value can be determined through an iterative procedure. The result of this approximation of the homoclinic orbit is shown in Fig. 5.2.

As a first-order perturbation on a conservative system the so called Melnikov function can be introduced:

$$M(t_0) = \int_{-\infty}^{\infty} f(z_h(t-t_0)) \wedge g(z_h(t-t_0), t)dt, \tag{5.6}$$

where z_h denotes the homoclinic orbit and the symbol "$\wedge$" denotes the wedge-product $f_1 g_2 - f_2 g_1$. Now according to the Melnikov method chaotic motion will occur if $M(t_0)$ has simple zeros, i.e. $M(t_0) = 0, M'(t_0) \neq 0$. [130] The integration limits of Eq. (5.6) are formally at $\pm\infty$ because the homoclinic orbit passes through an equilibrium point, which will take an infinitely long time to escape from since energy is conserved. Since $F_0 \neq 0$, the equation of motion Eq. (5.4) can divided by F_0, which will rescale $f(z)$ and $g(z,t)$

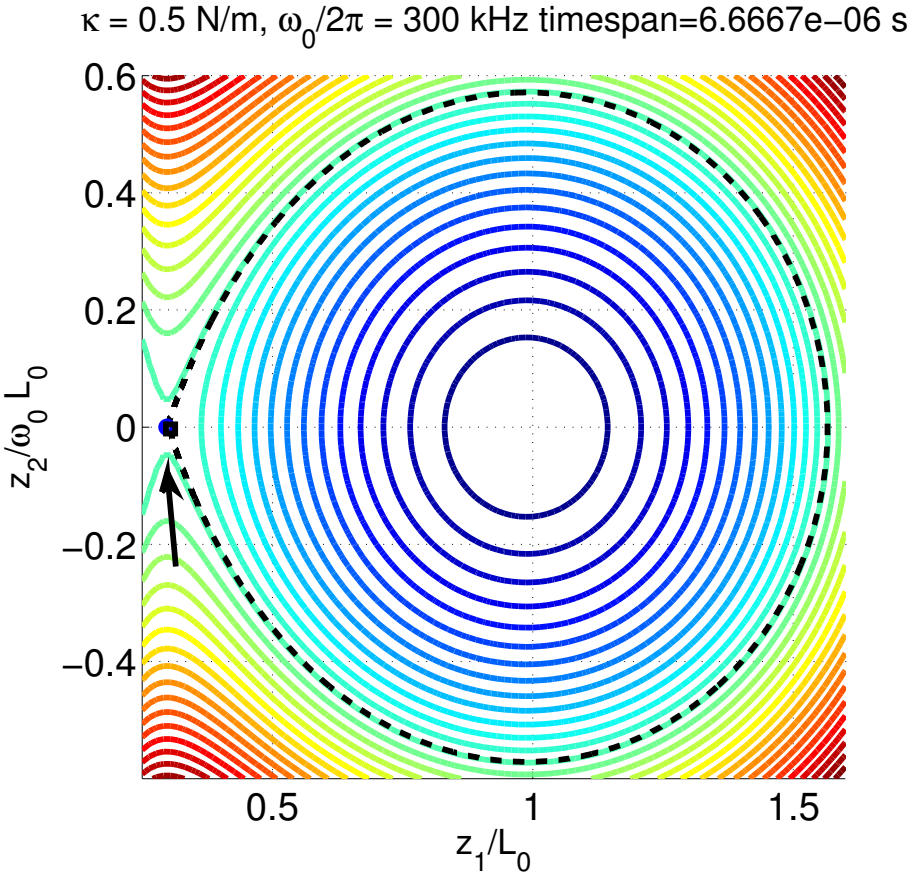

Figure 5.2: *Numerical approximation of the homoclinic orbit for the conservative system of Eq.* (5.1). *A point slightly to the right of the saddle,* $z_s + \delta$, *where* $\delta/L_0 = 2.5 \cdot 10^{-5}$, *is chosen as an initial condition for a Runge-Kutta solver, the output of which is displayed as (black) dashed line. The continuous (rainbow colored) lines are the energy level curves. The solver output lies quite close to a part of one of the energy level curves just outside the homoclinic orbit (indicated by the arrow). The exact homoclinic orbit lies somewhere in between.*

accordingly. For Eq. (5.4) the Melnikov function becomes

$$M(t_0) = \int_{-\infty}^{\infty} z_{2,h}(t)(\cos\omega(t+t_0) - \tfrac{\omega_0 L_0 \gamma}{F_0} z_{2,h}(t))dt, \tag{5.7}$$

where $z_{2,h}(t)$ denotes the second component of the homoclinic orbit. It can be shown that in this case the Melnikov function is a sinusoidal function of t_0 [133]:

$$M(t_0;\alpha) = -\alpha < z_{2,h}^2 > + A(\omega)\cos(\omega t_0 + \varphi(\omega)), \tag{5.8}$$

where the triangular brackets denote integration over the entire real axis, $\alpha \equiv \gamma\omega_0 L_0/F_0$, and $A(\omega)\cos(\omega t_0 + \varphi(\omega))$ is the real part of the Fourier transform of $z_{2,h}(t)$. (The functions

$A(\omega)$ and $\varphi(\omega)$ remain yet to be determined.) Hence instead of varying the parameters γ and F_0 independently, only the ratio between them needs to be considered: γ is kept fixed with $Q = 3000$ whereas F_0 is varied. Now the threshold condition for chaotic motion is $M(t_0) = 0, M'(t_0) = 0$, which is unaffected by the phase $\varphi(\omega)$. Only the envelope $A(\omega)$ in Eq. (5.8) determines for which values of α and ω this threshold condition is met. This envelope can be obtained by taking the absolute value of the Hilbert transform performed on $A(\omega)\cos(\omega t_0 + \varphi(\omega))$, which brings us to the following formulation of the threshold condition:

$$\alpha = \frac{|\mathcal{H}(\mathrm{Re}(\mathcal{F}(z_{2,h}(t))(\omega)))|}{< z_{2,h}^2 >}, \tag{5.9}$$

where $\mathcal{H}$ denotes a Hilbert transform and $\mathcal{F}$ denotes a Fourier transform. When performed on a function $a(t)$, the former is defined as:

$$\mathcal{H}[a(t)] \equiv \frac{1}{\pi} \int_{-\infty}^{\infty} a(\tau) \frac{1}{t-\tau} d\tau = a(t) * \frac{1}{t}, \tag{5.10}$$

which can be written as a convolution in the time domain.

Fig. 5.3 shows the result of Eq. (5.9) for both rough and flat surfaces. It is clear that a flat surface is more susceptible to chaotic motion than a rough one: for a fixed value of γ a higher value of F_0 is required for the motion to become chaotic. This is because the chaotic motion is associated with the nonlinearity of the Casimir force. The shift of the minimum separation distance due to roughness, [98,102] ensures that the Casimir force, i.e. the nonlinear part of Eq. (5.4) cannot become too large. Moreover, this shift appreciably reduces the range of motion of the oscillator, further diminishing the possibility of chaotic motion. This implementation of the Melnikov method can reproduce analytical results for a Duffing oscillator. (See appendix C)

5.3 Orbits of the perturbed system

The next step is to check the results of the Melnikov method presented in Fig. 5.3. The most rigorous way to do this is via a computation of stable and unstable manifolds in accordance with the Smale-Birkhoff homoclinic theorem. [130] (See appendix C.2 for more details and an example). Such manifold curves separate qualitatively different solutions in phase space. Their computation involves so called *Poincaré maps*, which transform a solution forward in time by exactly one period of the forcing, i.e. $2\pi/\omega$. Some solutions of the damped driven oscillator system are periodic with period $2\pi/\omega$. The initial conditions associated with such solutions are called *fixed points* of a Poincaré map. The computation of stable and unstable manifolds requires both the location of one of the fixed points and its associated periodic orbit.

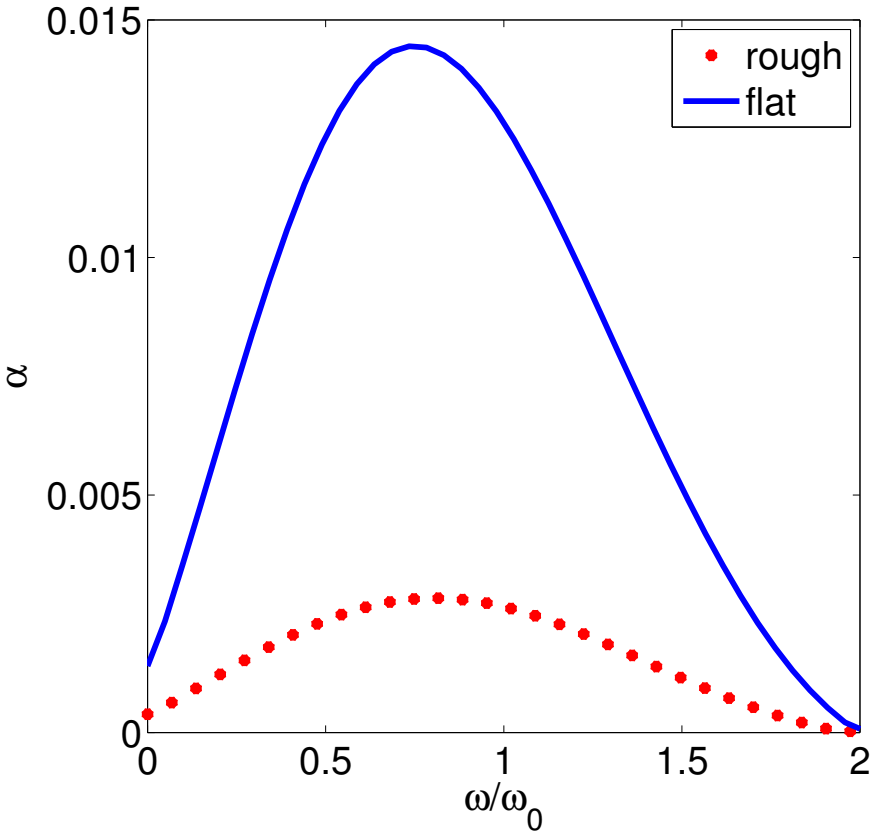

Figure 5.3: *Threshold curves based on Eq.* (5.9) *for both rough and flat surfaces. Chaotic motion can be expected for parameter values below each curve. Since* $\alpha \equiv \gamma\omega_0 L_0/F_0$*, a rough surface requires a larger value of* F_0 *than a flat surface (for a fixed value of* γ*).*

However, this computation is numerically very difficult. To understand this difficulty it is required to examine the so called *linearization* approximation [120]: the assumption that the equation of motion is approximately linear within a sufficiently small neighborhood of a point in phase space. (See appendix B for more details). The linearization approximation is quite generally valid with few exceptions for equations of motion involving terms exponential in the phase space variables. Most importantly it provides information about the nature and stability of equilibria (for autonomous systems) or fixed points (for periodically driven systems). It turns out that for Eq. (5.4) there are two fixed points: one unstable saddle and one stable sink. (See appendix B.2).

The difficulty in determining the manifolds arises from the degree of instability of the saddle: After a linearization the equation of motion in a sufficiently small neighborhood of the saddle is $\ddot{x} \approx \lambda^2 x$, where $\lambda = F'_{cas}(z_s)/\kappa$. The quantity λ can provide a measure of the degree of (in)stability of a fixed point of a Poincaré map (or an equilibrium). For

example, for the Duffing oscillator discussed in appendix C, $\lambda^2 \sim 1$ and the fixed point can be located without any problem. However, for the Casimir oscillator discussed here, $\lambda^2 \sim 10^3$, which makes it very difficult to find a spot in phase space that returns to a point close to itself after one period $2\pi/\omega$.

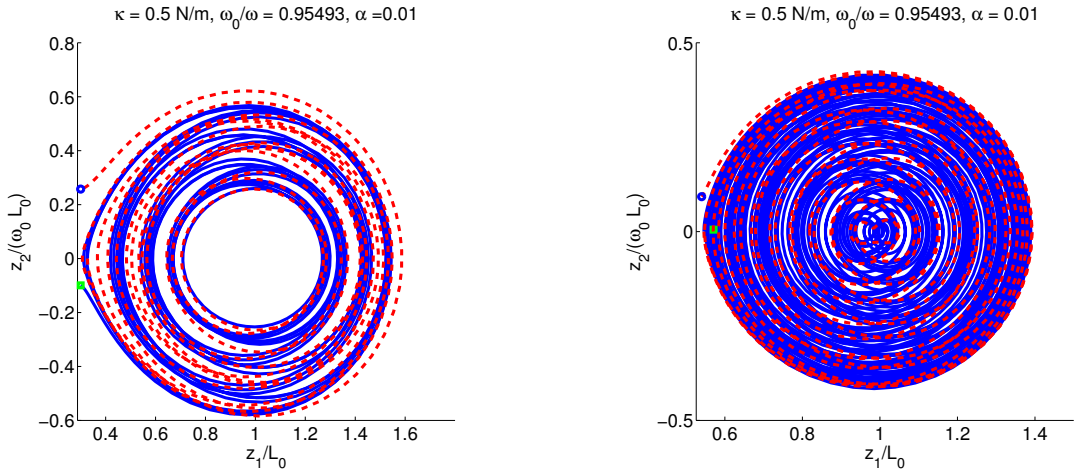

(a) (b)

Figure 5.4: *Orbits for: (a) A flat surface starting at* $((z_s + 3\ nm)/L_0, 0)$*, where* $z_s = 29.7\ nm$ *and (b) a rough surface starting at* $((z_s+1\ nm)/L_0, 0)$*, where* $z_s = 53.6\ nm$*. The ODE solver has run for 100 periods of the forcing in both cases, with the constraint that the oscillator remains at the right of* z_s*. The solid blue curve shows the result of the solver for time going forward, and the dashed red curve shows its output for* $t \to t' = -t$*. The blue circle marks the beginning of the motion and the green square indicates its ending.*

Instead we have computed orbits of Eq. (5.4) with the initial conditions close to the homoclinic orbit of the conservative case displayed in Fig. 5.2. The results are shown in Fig. 5.4. The outputs of the Runge-Kutta solver have been oppressed for values to the left of the saddle z_s of the unperturbed case, in which case stiction occurs. The values of $\alpha = 0.01$ and $\omega/\omega_0 \approx 0.95$ in Fig. 5.4 correspond to a point in parameter space below the solid blue threshold curve in Fig. 5.3, but it is above the dotted red curve. Hence for these parameter values chaotic motion is expected for the flat case, but not for the rough case. The blue curve in Fig. 5.4 shows the result of the solver for time going forward, and the red curve shows its output for $t \to t' = -t$. Chronologically this means that the motion begins at the end of the dashed red curve (marked by the blue circle), and that it ends at the end of the solid blue curve (marked by the green square). It is clear that within the simulation time of 100 periods of $2\pi/\omega$, the motion escapes from the sink fixed point and devolves to stiction in the flat case, contrary to the rough case. (Again, the simulation

was cut off once the oscillator moved to the left of the saddle). This is how "chaotic motion" can be interpreted in terms of MEMS applications: as the fading of the area in phase space where stable actuation can be distinguished from stiction. Indeed, this is quite contrary to e.g. the conservative case where the two phenomena are clearly demarcated by the homoclinic orbit. Again, this computation is not entirely conclusive, since it does not exclude the possibility that the motion of the oscillator escapes from the homoclinic orbit after a longer simulation time in the rough case. Moreover the orbits represent a solution for merely one initial condition. However, even after 1000 periods the oscillator won't escape from the sink in the rough case, whereas the oscillator cannot complete even 100 periods in the flat case. Moreover, the result in Fig. 5.4 is consistent with the evaluation of the Melnikov functions and their associated threshold curves. Therefore it is likely that this result is due to the transverse intersection of the separatrices.

We repeat that the Casimir force constitutes the nonlinearity of the equation of motion. Due to the shift of the minimum separation in the rough case, this nonlinearity cannot become too large, contrary to the flat case. This explains why a flat surface requires a smaller forcing amplitude to exhibit chaotic motion than a rough surface. After all, chaotic motion is associated with the nonlinearity of the equation of motion. Moreover, surface roughness considerably limits the range of motion of the oscillator, which further decreases its susceptibility to chaotic motion.

5.4 Concluding remarks

We have investigated under which conditions chaotic motion occurs in a damped driven Casimir oscillator. We have demonstrated that the nonlinearity of the Casimir force can give rise to chaotic motion of MEMS at separations below 100 nm. Surface roughness makes the MEM system less susceptible to this effect according to the Melnikov method. Due to the high degree of instability of the saddle fixed point, a calculation of stable and unstable manifolds based on the Smale-Birkhoff homoclinic theorem has not been performed. Despite of this, we believe that it is likely that the result of such a computation would be consistent with that of the Melnikov method. This is because an orbit with initial conditions close to the homoclinic orbit of the unperturbed system does not escape the sink in the rough case whereas it does in the flat case. This calculation was performed for parameter values above the threshold curve for rough surfaces and below it for flat surfaces. Hence the calculation of this orbit is consistent with the result of the Melnikov method.

The reason why a flat surface is more susceptible to chaotic motion than a rough one, is that roughness increases the minimum separation, thereby reducing the range of motion of the oscillator and the effective interaction area of the surfaces. Contact between two gold

asperities can be ruptured with a force in the order of 1.5 nN, [134] whereas the dispersion forces can be expected to be orders of magnitude larger for surfaces with $d_0 < 10$ nm, [115] as was shown in chapter 3.

Furthermore, it is worth emphasizing that the method used here does not require an analytical expression for the Casimir force, or for any other surface force one may want to consider. Approximations like perfect reflectors or polynomial expansions are not necessary. For example, it could accommodate theoretical roughness corrections to hydrodynamic [123, 125] and capillary forces [135–137] for devices operating under ambient conditions. Other future investigations may be focused on the correlation between the effects of material properties and roughness on the Casimir force.

Appendix A

Electrostatically actuated MEMS

This appendix examines the case of a purely electrostatically actuated MEM system, i.e. one where the Casimir force is ignored. In chapter 2 it was mentioned that the electrostatic force can also display non-additive properties. We investigate whether that is the case here. Next, a bifurcation diagram for an electrostatically actuated MEM system will be computed to check some of the more general results presented in chapter 4.

Let us consider the expression for the electrostatic force between rough gold surfaces:

$$F_{es}(z) = F_e(z) + F_{pe}(z) + \int_{d_1}^{d_0} f(h)[F_e(z-h) - F_e(h) + hF_e'(h) - \tfrac{1}{2}h^2F_e''(h)]\mathrm{d}h, \tag{A.1}$$

where d_1 denotes the height of the lowest 'peak', i.e. the height above which Gumbel distributions must be used to describe the height fluctuations of the surface [102, 115]. It is assumed that contributions of the peaks, given by the third term on the right hand side of Eq. (A.1), are independent of each other and are considered to be 'local' in this sense. The first two terms of Eq. (A.1), denoting the electrostatic force between flat surfaces and a second-order perturbative correction [117] respectively, actually take into account the interaction between contributions and are thus 'nonlocal' in the same sense. These two terms, $F_e(z)+F_{pe}(z)$, represent contributions due to roughness features which are typically within a distance of one root-mean-square (rms) from the average height (which is zero by definition).

The result of Eq. (A.1) is plotted in Fig. 2.2, indicated by the solid (black) line. This is compared to the result of simply taking the statistical average (indicated by the dashed (green) line):

$$F_{ePFA}(z) = \int_{-d_0'}^{d_0} f(h)F_e(h-z)\mathrm{d}h \tag{A.2}$$

which completely neglects nonlocal effects on the electrostatic force whereas Eq. (A.1) takes such effects into account for "regular roughness" i.e. the parts of the surface excluding high peaks or deep troughs. Eq. (A.2) is the analogue of what is known as the 'proximity

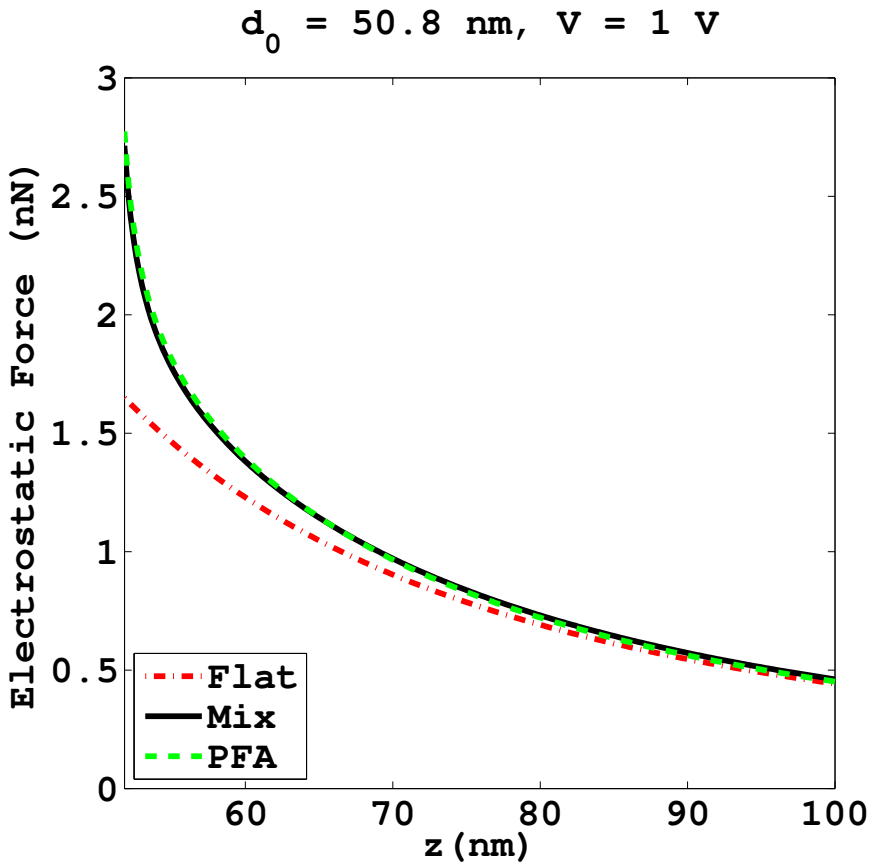

Figure A.1: *Electrostatic force between rough surfaces. The solid (black) line shows the result of Eq.* (A.1)*, the dashed (green) shows that of Eq.* (A.2)*. The dotted (red) line represents the electrostatic force without roughness correction.*

force approximation'(PFA) in the context of the Casimir effect. From Fig. A.1 it is clear that nonlocal effects for the electrostatic force are negligible: the inset shows the two contributions to the total electrostatic force corresponding to 'regular roughness'. Here the 'local' approximation is given by the integral in Eq. (A.2) within the interval $-d_1' < h < d_1$, whereas the 'nonlocal' contribution is given by the first two terms on the right hand side of Eq. (A.1). It is clear that these two results overlap; the slight difference possibly due to nonlocal effects does not exceed the numerical error. By the same token, the (very slight) difference between the solid (black) line and the dashed (green) line at short separations in Fig. 2.2 is entirely a numerical artifact due to the integration algorithms used. This paragraph is concerned with the case where $F_{cas}(z) = 0$, $F_{es}(z) \neq 0$ in Eq. (4.7) for the conservative system described in chapter 4. Since the Casimir force originates from quantum mechanical uncertainty this case is a rather artificial one. However if *both* the voltage V *and* the spring constant κ are large enough such that $\lambda_{cas} \ll \lambda_{es}$ then the Casimir force will be negligible compared to both the elastic restoring force and the electrostatic

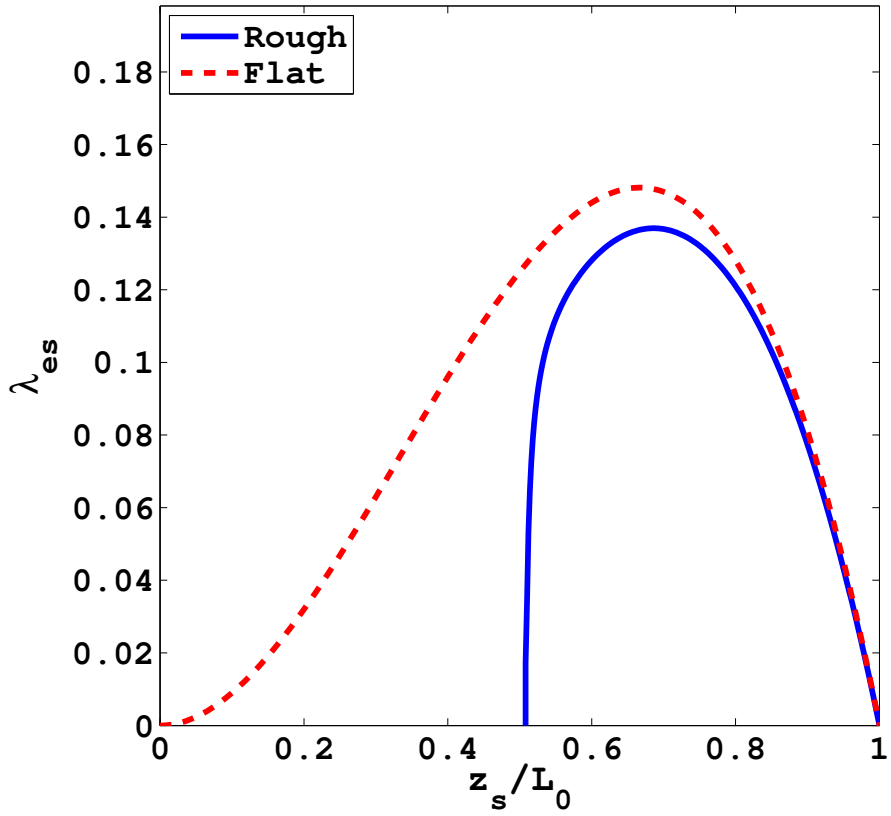

Figure A.2: *Bifurcation diagram for MEMS actuated only by the electrostatic force.*

force. The purpose of this calculation is to provide a check for the more general case in which neither surface force is zero. In an equilibrium the total force $F_{tot} = 0$, which leads to the relation $\lambda_{es} = F_e(L_0)/F_{es}(z_s)(1 - z_s/L_0)$, plotted in Fig. A.2. This case is qualitatively similar to that of a Casimir actuated MEMS, but the roughness effect is less pronounced because the distance dependence of the electrostatic force is weaker than that of the Casimir force. More importantly, the result plotted in Fig. A.2 is consistent with that for the case of two parameters, in particular Fig. 4.3b of chapter 4.

Appendix B

Linearization: equilibria and fixed points

B.1 Eigenvalues of the Jacobian

In chapter 4 it was mentioned that in a conservative (Hamiltonian) system, the phase portraits can be obtained by plotting the level curves of the total energy. Here an alternative method is presented, namely considering the eigenvalues of the Jacobian. This method, called linearization, works if the system behaves linearly in a sufficiently small neighborhood of the equilibrium points.

A well known and general property of an n^{th} order ODE is that it can can be decomposed into an n-dimensional system of first order ODEs. [120] Therefore the ODE considered here

$$m\frac{\mathrm{d}^2 z}{\mathrm{d}t^2} = \kappa(L_0 - z) - F(z) \tag{B.1}$$

can be written as

$$\begin{aligned} y &= \frac{\mathrm{d}z}{\mathrm{d}t} \\ \frac{\mathrm{d}y}{\mathrm{d}t} &= \tfrac{1}{m}(\kappa(L_0 - z) - F(z)), \end{aligned} \tag{B.2}$$

where $F(z) = F_{Cas}(z) + F_{es}(z)$. The nature of the equilibria can be determined from the eigenvalues of the corresponding Jacobian matrix in those equilibrium points. For a two dimensional system (like this one) the Jacobian is defined as

$$J \equiv \begin{pmatrix} \frac{\partial f_1(z,y)}{\partial z} & \frac{\partial f_1(z,y)}{\partial y} \\ \frac{\partial f_2(z,y)}{\partial z} & \frac{\partial f_2(z,y)}{\partial y} \end{pmatrix}, \tag{B.3}$$

where the functions $f_{1,2}(z, y)$ denote the system of first order ODEs. For Eq. (B.2) this is

$$J = \begin{pmatrix} 0 & 1 \\ \frac{-1}{m}(\kappa + F'(z)) & 0 \end{pmatrix}, \tag{B.4}$$

which has the eigenvalues $\lambda_{1,2} = \pm i/\sqrt{m}\sqrt{F'(z) + \kappa}$. Note that $\kappa > 0$ and $F'(z) < 0$. Let z_s be an equilibrium point. Depending on the eigenvalues, three cases can be distinguished:

1. $-F'(z_s) > \kappa$: The eigenvalues of the Jacobian in this point are real and distinct, which implies that z_s is an (unstable) saddle point equilibrium. Qualitatively, it is clear that $F(z)$ decreases fast for small z near the contact distance d_0. Hence this is where one may expect such saddle point equilibria to occur. Indeed this is consistent with the phase portraits in the chapter 4 which can be obtained by plotting the level curves of the energy.

2. $-F'(z_s) < \kappa$: The eigenvalues are purely imaginary and each other's complex conjugate. This condition typically holds for large values of z. In this case the nature of the equilibrium points cannot be determined analytically: it can be an (unstable) spiral source, a (stable) spiral sink, or a center equilibrium around which periodic solutions exist. However, in a sufficiently small neighborhood of this equilibrium the ODE is linear and must reproduce the case of the simple harmonic oscillator. Physically this corresponds to the surface forces being approximately linear for small enough amplitudes. In this case it is clear that periodic solutions to the equation of motion exist, which is also represented by the closed curves in the numerically obtained phase portraits. Therefore z_s is a center equilibrium in this case.

3. $-F'(z_s) = \kappa$: The only eigenvalue is zero: $\lambda_{1,2} = 0$. This is where the saddle point and the center equilibrium merge. Hence this case is known as the saddle-center equilibrium [121]. This equilibrium is also unstable. It corresponds to the maximum values of the bifurcation parameters in the bifurcation diagrams. This equilibrium occurs at separations of approximately 80 nm. This value changes only slightly for different degrees of roughness. (This point corresponds to the maxima in Fig. 4.2a)

Note that for sufficiently large κ both equilibria are stable at any physical value of $d_0 - z$, i.e. where this local separation exceeds the interatomic distances of the material. This case corresponds to joining of the equilibria shown in Fig. 3d of the main chapter 4, which becomes graphically visible when also the electrostatic force is present. Effectively it means there is only one (stable) equilibrium.

B.2 Monodromy matrix

Contrary to the conservative case, there is no such thing as an equilibrium in a periodically driven system. Rather, in such a case so called fixed points of Poincaré maps can be defined. A fixed point is a point (in phase space) that is invariant under a certain mapping. A Poincaré map transforms a solution forward in time by one period of the forcing, i.e. $2\pi/\omega$, where ω denotes the forcing frequency. A particular solution that is invariant under a Poincaré map is periodic with period $2\pi/\omega$. The set of initial conditions associated with such a solution is known as a *fixed point* of a Poincaré map.

By the same token as in the conservative case, in a sufficiently small neighborhood of a fixed point $z_0(t)$, the equation can be assumed to be approximately linear. However instead of calculating the Jacobian $J(z_0(t))$, the so called fundamental solution matrix Φ must be determined. This matrix satifies

$$\dot{\Phi} = J(z_0(t))\Phi \qquad \Phi(0) = I, \tag{B.5}$$

where I denotes the identity matrix. The fundamental solution matrix at time $t = 2\pi/\omega$ is known as the *monodromy matrix*. This matrix plays the same role as the Jacobian in the conservative case: the nature and the stability of a fixed point are directly related to the eigenvalues of the monodromy matrix in that point, and vice versa.

Note that the dimensionality of the phase space has not yet been specified in Eq. (B.5). In principle one could argue that since time is an independent variable, it will give rise to an additional phase space dimension. However, it will be shown here that only two dimensions need to be considered: Let $z_0(t)$ be a periodic solution of the system $z'(t) = h(z)$ with period $T = 2\pi/\omega$. The corresponding variational equation is

$$\dot{\delta z}(t) = J(z_0(t))\delta z(t).$$

We want to show that $\delta z(t)$ is a T-periodic solution of the variational equation. Taking the time derivative gives

$$\dot{\delta z} = J(z_0(t))\dot{z_0} = J(z_0(t))h(z_0(t)) = J(z_0(t))\delta z,$$

and $\delta z = h(z_0(t))$ is T-periodic. This implies that $\delta z(0) = h(z_0(0))$ is an eigenvector of the monodromy matrix with eigenvalue 1. Due to the periodicity of the explicit time dependence extending phase space by an extra dimension does not provide any additional information about the nature of the fixed point.

Therefore it suffices to consider the two other eigenvalues only. For example, a fixed point with real eigenvalues $|\lambda_1| < 1 < |\lambda_2|$ corresponds to an unstable saddle fixed point. Two complex conjugate eigenvalues with $|\lambda_{1,2}| < 1$ correspond to a stable sink. These eigenvalues, sometimes called Floquet multipliers, have been calculated for Eq. (5.4).

Not only the eigenvalues but also the eigenvectors of the monodromy matrix in a fixed point provide relevant information. The eigenvectors should be tangent lines of the homoclinic orbit in the saddle point. These vectors, starting from the position of the fixed point, provide the initial conditions for the numerical determination of the stable and unstable manifolds. [138] These manifolds play the same role as the homoclinic orbit in the conservative case: they are *separatrices*, i.e. they separate qualitatively different solutions. The Smale-Birkhoff homoclinic theorem states that chaotic motion will occur if and only if the stable and unstable manifolds intersect transversely. [130]

Appendix C

A test case: the Duffing oscillator

C.1 Melnikov method for Duffing oscillator

Here the numerical implementation of the Melnikov method from chapter 5 will be compared to an analytical result for a typical textbook case: the Duffing oscillator. In the conservative case, the equation of motion is

$$\begin{aligned} \dot{z_1} &= \tfrac{z_2}{\omega_0 L_0} \\ \dot{z_2} &= \tfrac{1}{\kappa L_0}(-\kappa(L_0 - z_1) + \kappa_3(L_0 - z_1)^3), \end{aligned} \tag{C.1}$$

where $\kappa_3 = \kappa$ and the other the parameter values are identical to those in chapter 5. This type of equation is typically used to model oscillations with large amplitudes, which give rise to deviations from the usual linear behavior. Specifically, Eq. (C.1) could describe an inverted pendulum with amplitudes that warrant a third order correction to Hooke's law. However, this physical interpretation is not the reason to choose negative linear stiffness in this case. Rather it is because the conservative case is more similar to that of the Casimir oscillator discussed in chapters 4 and 5 than the case of positive linear stiffness, as we will show. The case of positive linear stiffness results in two heteroclinic orbits [133], rather than homoclinic ones. (That is, two saddles are accompanied by one center instead of the other way around.)

The corresponding Hamiltonian is

$$H(z) = \tfrac{1}{2}mz_2^2 - \tfrac{1}{2}\kappa(L_0 - z_1)^2 + \tfrac{1}{4}\kappa_3(L_0 - z_1)^4. \tag{C.2}$$

The level curves of H are shown in Fig. C.1. There are two center equilibria at $(1/L_0 \pm 0.01/L_0, 0)$ and one saddle at $(1/L_0, 0)$. The two homoclinic orbits are symmetric around the line $z_1 = L_0$. Therefore the calculation of one of the homoclinic orbits is identical to that of the other.

The homoclinic orbit corresponds to the energy level $H = 0$. This gives rise to an implicit function relation for the homoclinic orbit as a function of time. The solution for the second component can be shown to be: [130]

$$z_{2,h}(t) = -\sqrt{2}\omega_0 L_0 \operatorname{sech}(\omega_0 t)\tanh(\omega_0 t), \tag{C.3}$$

which is plotted in Fig. C.2. Fig. C.2 shows that the expression of Eq. (C.3) is quite well reproduced by the approximation shown in Fig. C.1. The slight deviation near the end of the run time of the ODE solver is due to the fact that the solver does not return exactly to the saddle. The contribution here is close to zero and it will be shown that the end result of the Melnikov function is not greatly affected by this deviation. For the other homoclinic orbit, the sign of $z_{2,h}(t)$ in Eq. (C.3) should be reversed.

Next we allow for some energy loss and gain as in chapter 5:

$$\begin{aligned} \dot{z_1} &= \tfrac{z_2}{\omega_0 L_0} \\ \dot{z_2} &= \tfrac{1}{\kappa L_0}(-\kappa(L_0 - z_1) + \kappa_3(L_0 - z_1)^3 - \epsilon\gamma z_2 + \epsilon F_0 \cos\omega t). \end{aligned} \tag{C.4}$$

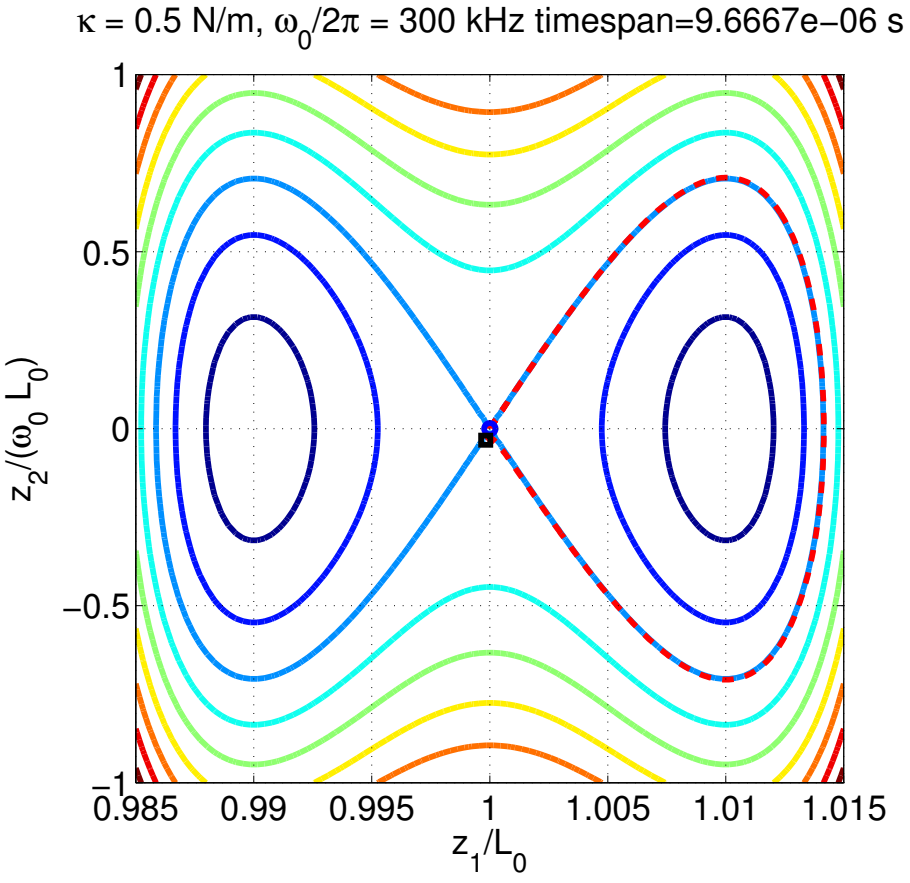

Figure C.1: *Phase portrait of a Duffing oscillator. The continuous lines are level curves of the Hamiltonian H in Eq. (C.2). The dashed line shows the output of a Runge-Kutta solver for initial conditions close to the saddle equilibrium inside the homoclinic orbit.*

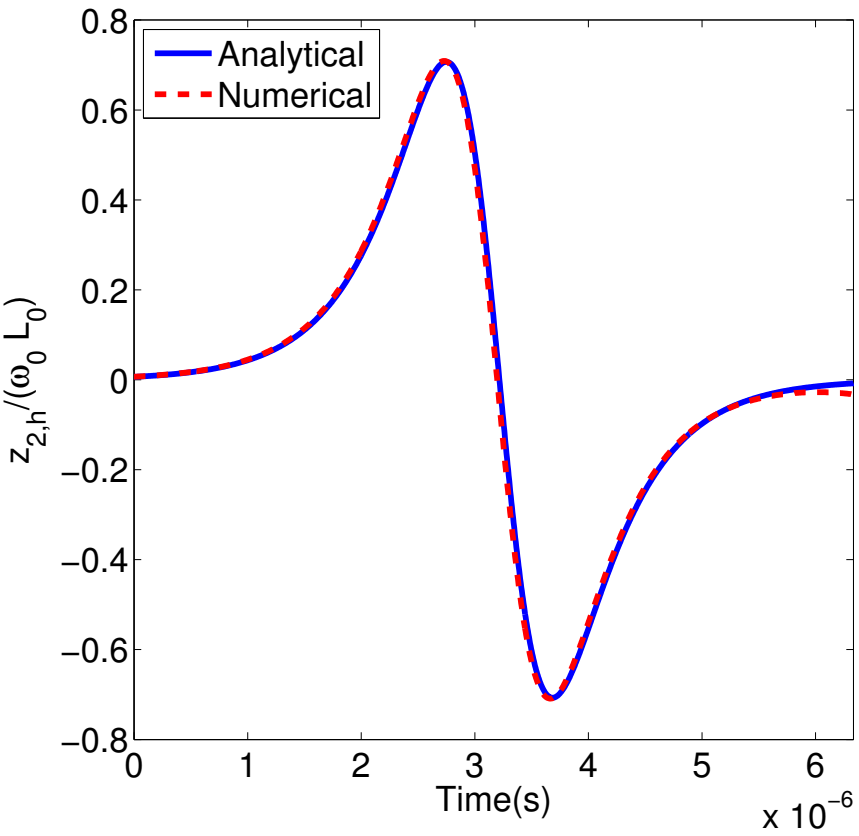

Figure C.2: *Second component of the homoclinic orbit as a function of time. The blue continuous line shows result of Eq.*(C.3)*, the dashed line shows the result of approximating the homoclinic orbit as a periodic solution inside it as shown in Fig. C.1.*

The Melnikov function is:

$$\begin{aligned} M(t_0) &= \int_{-\infty}^{\infty} z_{2,h}(t)(F_0 \cos\omega(t+t_0) - \gamma\omega_0 L_0 z_{2,h}(t))dt \\ &= -\sqrt{2}\omega_0 L_0 F_0 \int_{-\infty}^{\infty} \operatorname{sech}(\omega_0 t)\tanh(\omega_0 t)\cos\omega(t+t_0)dt \\ &\quad -2\omega_0^2 L_0^2 \gamma \int_{-\infty}^{\infty} \operatorname{sech}^2(\omega_0 t)\tanh^2(\omega_0 t)dt, \end{aligned} \tag{C.5}$$

where the first integral can be evaluated with Cauchy's residue theorem. The result is

$$M(t_0; F_0, \gamma, \omega) = -\frac{4\gamma L_0^2 \omega_0}{3} + \sqrt{2}\frac{\omega}{\omega_0}\pi L_0 F_0 \operatorname{sech}\left(\frac{\pi\omega}{2\omega_0}\right)\sin\omega t_0. \tag{C.6}$$

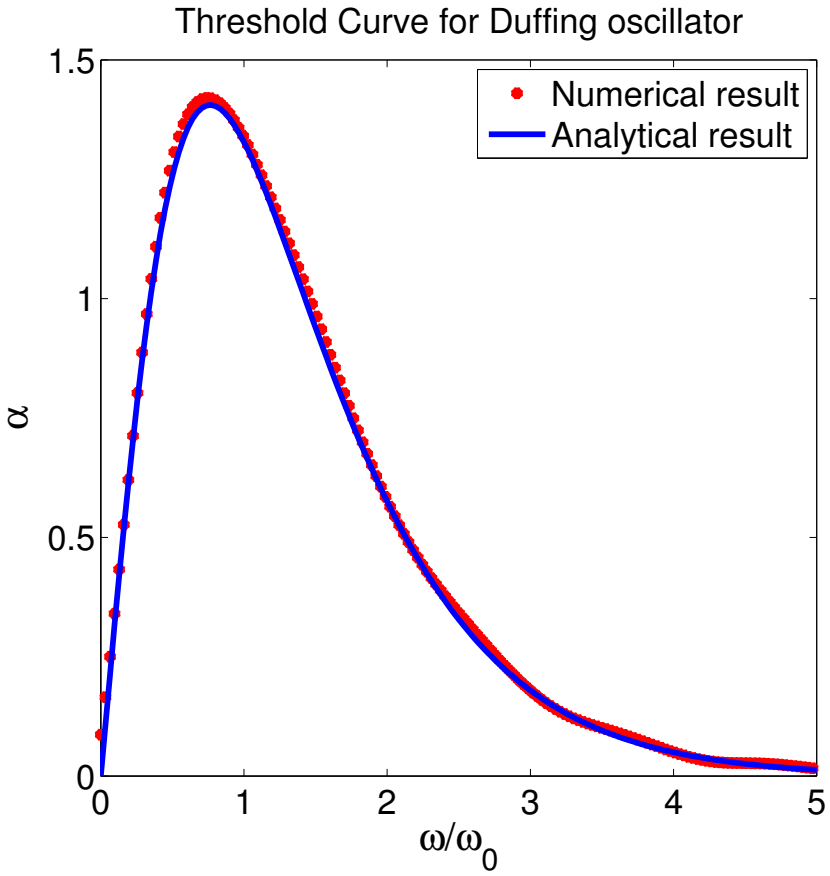

Figure C.3: *Threshold curve for a Duffing oscillator, where* $\alpha \equiv \gamma\omega_0 L_0/F_0$. *For parameter values below the curve chaotic motion can be expected. The blue continuous line corresponds to Eq.* (C.7) *and the red asterisks show the result of Eq.* (5.9)*, which needs to be multiplied by a factor of 2 to account for the two homoclinic orbits.*

Under what condition simple zeros ($M(t_0) = 0$, $M(t_0) \neq 0$) occur is determined by the following relation for the threshold curve:

$$\alpha = \frac{3\sqrt{2}\pi}{4}\frac{\omega}{\omega_0}\,\mathrm{sech}\left(\frac{\pi\omega}{2\omega_0}\right), \tag{C.7}$$

where $\alpha \equiv \gamma\omega_0 L_0/F_0$. In Fig. C.3 the result of Eq. (C.7) is compared to that of the numerical implementation of Eq. (5.9) for the Duffing oscillator of Eq. (C.4). The agreement is good, but the numerical curve cannot pass exactly through the origin (as it should) due to limitations of the finite Fourier transform (FFT) algorithm [139].From Fig. C.3 it is clear that a Duffing oscillator is far more susceptible to chaotic motion than a Casimir oscillator: the threshold values are an order of magnitude larger than in Fig. 5.3. This is because a Duffing oscillator has a significantly larger range of motion, resulting in two homoclinic orbits rather than one.

C.2 Computation of Separatrices

The next step is now to check the threshold values obtained from the Melnikov method. To this end the Smale-Birkhoff homoclinic theorem [130] should be applied. This theorem states that chaos will occur if and only if the stable and unstable manifolds intersect transversely. A general and precise definition of a manifold is difficult to provide, but in this particular context the manifolds fulfill the role of *separatrices*. That is, they separate qualitatively different solutions in phase space, like the homoclinic orbit does in the conservative case. Indeed if such separatrix curves intersect transversely, then it can be conceptually clear how it relates to "chaos" in the sense of slightly different initial conditions giving rise to qualitatively different solutions. [131]

The separatrices can be numerically determined as follows: [138] Let $v_s(z_s)$ be the eigenvector of the monodromy matrix (See appendix B.2) corresponding to the eigenvalue smaller than 1 and with the origin in the saddle z_s and length $\epsilon \ll 1$. Choose an array P_N of $N \gg 1$ equidistant points on v_s. Then the stable manifold $W^s(z_s)$ can be approximated by performing $M \gg 1$ iterations of a Poincaré map on the points P_N: $W^s(z_s) \approx \Sigma^M(P_N(v_s(z_s)))$, where Σ denotes a Poincaré map. Similarly, for the unstable manifold these iterations must be performed on the eigenvector $v_u(z_s)$ corresponding to the eigenvalue greater than 1. However, in addition the operation $t \to t' = -t$ must be performed for each iteration of the Poincaré map. So the unstable manifold is approximated by $W^u(z_s) \approx \Sigma^M(P_N(v_u(z_s)))|_{t'=-t}$. Now the smaller ϵ and the larger M and N, the better this approximation is, being first order in ϵ.

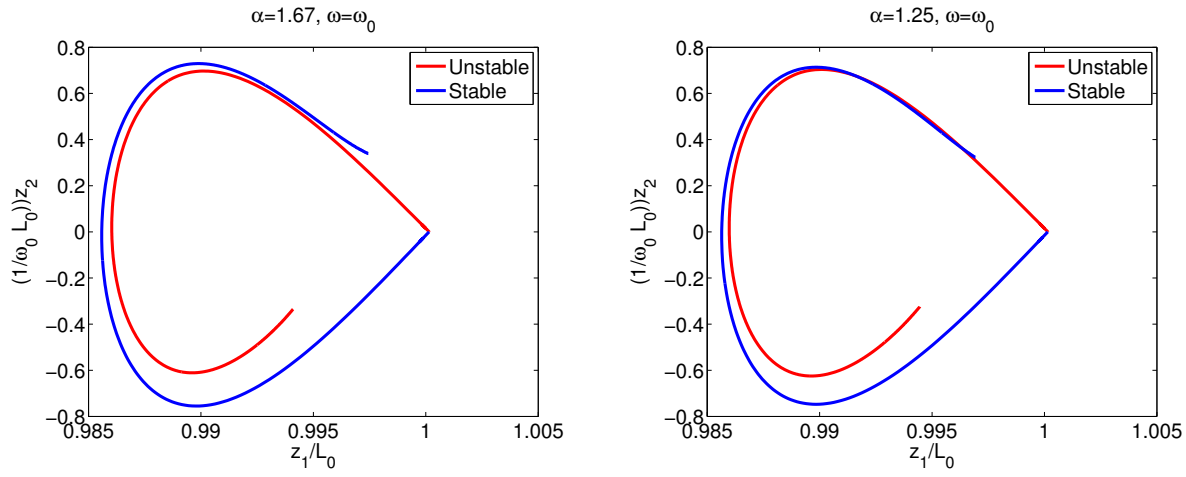

(a) (b)

Figure C.4: *Stable and unstable manifolds for a Duffing oscillator. (a) Parameter values lie above the threshold curve of Fig. C.3. (b) Parameter values lie below the threshold curve of Fig. C.3*

The result of such calculations of the separatrices for the Duffing oscillator are shown in Fig. C.4. The stable and unstable manifolds do not intersect in Fig. C.4a for values above the threshold curve in Fig. C.3. For parameter values below this threshold curve the manifolds do intersect transversely (See Fig. C.4b). This means that in this case the result of the Melnikov method is consistent with the Smale-Birkhoff homoclinic theorem. Note that the curves in Fig. C.4 appear continuous, but they are not: since the manifolds are Poinaré maps, the "curves" are really dots separated in time by intervals of $2\pi/\omega$. The motion at the curves is *almost* periodic with period $2\pi/\omega$; after one period of the forcing the Poincaré map returns to a position very close to the original one, so that the string of dots appears to be a continuous curve. For this reason it is required to obtain the periodic orbit associated with the saddle fixed point in order to calculate stable and unstable separatrices.

Samenvatting

In dit proefschrift komen twee onderwerpen aan de orde: ten eerste de Casimir-kracht op afstanden kleiner dan 100 nm, en ten tweede de gevolgen ervan voor de actuatiedynamica van micro- of nano-elektromechanische systemen (MEMS respectievelijk NEMS). De Casimir-kracht is een elektromagnetische dispersie-interactie tussen elektrisch neutrale oppervlakken zonder permanente dipolen, die voortkomt uit kwantummechanische en thermische fluctuaties. De bekendere van der Waalskracht komt overeen met de limiet van korte afstanden ten opzichte van de voornaamste absorptie-golflengte van de materialen, in welk geval retardatie te verwaarlozen is. Retardatie is de vertraging van een elektromagnetische interactie door de eindigheid van de lichtsnelheid. Een MEM systeem is een verzamelnaam voor apparaten met bewegende onderdelen die werken op een micrometer schaal. Voorbeelden hiervan zijn microschakelaars, versnellingsmeters, en cantileververeren. De actuatiedynamica is gewoonweg de dynamica van deze bewegende onderdelen. Zowel in MEMS toepassingen als in metingen van de Casimir-kracht kunnen bewegende onderdelen van het MEMS permanent aan elkaar vast gaan zitten. Dit is een fenomeen dat stictie wordt genoemd. Een deel van dit proefschrift richt zich op bijdrage van de Casimir-kracht aan stictie.

De gedachte bij het bestuderen van de invloed van dispersie-interacties is dat de Casimirkracht een fundamentele beperking oplegt aan MEMS toepassingen. Immers, een elektrostatische kracht kan worden beperkt door het voltage tussen de oppervlakken te verkleinen. De hydrodynamische wrijvingskracht en de capillaire interactie kunnen worden vermeden door de componenten te laten bewegen in een schone en droge omgeving. De Casimir-kracht kan echter niet zomaar worden uitgeschakeld als dat toevallig goed uitkomt, omdat zij voortkomt uit kwantummechanische onzekerheid. Daarom draagt de Casimir-kracht altijd bij aan stictie in MEMS. Op afstanden kleiner dan 100 nm is de Casimir-kracht groot genoeg om van enig praktisch belang te zijn voor MEMS toepassingen. Uit een experiment is echter gebleken dat de ruwheid van de oppervlakken de Casimir-kracht significant

beïnvloedt op deze afstanden. Daarom wordt in dit proefschrift een model geïntroduceerd om dit effect theoretisch te beschrijven. Dit model stelt ons vervolgens in staat om de invloed van de Casimir-kracht op de actuatiedynamcia van MEMS componenten op een realistische manier te beschrijven.

De theorie die later de Lifshitz-theorie is gaan heten vormt een belangrijke basis; niet alleen voor dit proefschrift, maar ook voor het vakgebied van de Casimir fysica in het algemeen. Deze theorie is een generalisatie van eerder werk van Casimir en Polder uit 1948. Zij ontdekten dat retardatie ervoor zorgt dat de van der Waalskracht één macht sneller afneemt als functie van de afstand tussen de oppervlakken dan in het niet-geretardeerde geval. In hetzelfde jaar ontdekte Casimir dat een identiek resultaat kan worden afgeleid uit kwantummechanische notie van het vacuüm, ook wel nulpuntsenergie geheten. Hierin wordt het bestaan van virtuele fotonen verondersteld. De oppervlakken leggen randvoorwaarden op aan deze virtuele fotonen ertussen, terwijl de fotonen aan de buitenkant niet aan deze randvoorwaarden hoeven te voldoen. Dit leidt tot een netto aantrekkingskracht. Dit werk beperkte zich tot ideale reflectoren, met andere woorden oppervlakken die *alle* elektromagnetische straling zonder verlies reflecteren, onafhankelijk van de frequentie ervan.

In echte materialen hangt de hoeveelheid straling die zij absorberen en reflecteren af van de frequentie. Dit fenomeen heet dispersie. Later, in 1954, slaagde Lifshitz erin het resultaat van Casimir te generaliseren via de fluctuatie-dissipatie stelling. Deze stelling legt een verband tussen de absorptie van het elektromagnetische veld door de materialen en de schommelingen in de beweging van de ladingen aan het oppervlak. Hieruit bleek hoe de Casimir-kracht afhangt van de permittiviteit (de diëlektrische functie) van de materialen van de oppervlakken. Ook werd duidelijk hoe de kracht van de temperatuur afhangt. Bovendien beperkt de Lifshitz-theorie zich niet tot slechts de geretardeerde of niet-geretardeerde limieten, maar is zij ook geldig op alle afstanden daartussenin. De enige beperking is dat de afstand veel groter moet zijn dan de typische afstand tussen de atomen in het materiaal, omdat zij het systeem macroscopisch beschrijft. In 1959 hebben Dzyaloshinskii, Lifshitz, en Pitaevskii de theorie opnieuw geformuleerd in termen van de thermische Green functie. Dit stelde hen in staat om te zien hoe de Casimir-kracht verandert als er zich tussen de oppervlakken een vloeistof bevindt.

Zoals al opgemerkt, op afstanden kleiner dan 100 nm kan de ruwheid van de oppervlakken een significante invloed hebben op de Casimir-kracht. Deze ruwheid houdt in dat er onvoldoende informatie is over de precieze vorm van het oppervlak en bijgevolg ook over de afstand tussen de oppervlakken. Vanwege dit gebrek aan informatie is moet dit probleem statistisch worden benaderd. Het is echter onjuist om de Casimir-kracht gewoonweg statistisch te middelen omdat de Casimir-kracht niet optelbaar is. Met andere woorden, de bijdragen aan dit gemiddelde zijn in het algemeen niet onafhankelijk van elkaar en kunnen niet zomaar bij elkaar worden opgeteld. Een manier om de invloed van ruwheid theoretisch

te beschrijven is een benadering, waarin een ruw oppervlak wordt beschouwd als een kleine afwijking van een vlak oppervlak. Dit is vergelijkbaar met een Taylor-ontwikkeling van de verhouding tussen root-mean-square (r.m.s.) ruwheid en de gemiddelde afstand. Deze benadering heeft een aantal voordelen: ten eerste houdt zij rekening met het feit dat de Casimir-kracht niet optelbaar is, en ten tweede is zij makkelijk te schatten. In een experiment zijn de voorwaarden voor een dergelijke benadering echter niet noodzakelijk geldig. Dit blijkt in het bijzonder uit metingen van de Casimir-kracht tussen ruwe goudlaagjes, waarin het resultaat van deze benadering in sommige gevallen meer dan 100 % afweek van de data.

Om deze discrepantie op te lossen is een model ontwikkeld dat is gebaseerd op een statistische analyse van reliëfdata van een atoomkrachtmicroscoop (AFM). Hieruit is gebleken dat er behalve hoogte-fluctuaties die binnen de r.m.s. waarde liggen, er ook aanzienlijk hogere oneffenheden zijn die niet aan een normaalverdeling gefit kunnen worden. Dit soort oneffenheden vereist extreme waarden statistiek, in het bijzonder kunnen zij worden gefit aan een Gumbel-verdeling. In het model wordt aangenomen dat de bijdragen van dit soort oneffenheden onafhankelijk van elkaar zijn, met andere woorden dat zij in dit geval wel optelbaar zijn. De reden hiervoor is de statistische zeldzaamheid ervan: hierdoor is de horizontale afstand ertussen relatief groot zodat de interactie tussen de bijdragen verwaarloosbaar is. Dit geldt *niet* voor de bijdragen van de andere oneffenheden die typisch binnen de r.m.s. waarde liggen en die wél aan een normaalverdeling kunnen worden gefit. Op de bijdrage van deze oneffenheden wordt de eerdergenoemde Taylor-achtige methode toegepast. Dit laatste is gerechtvaardigd omdat de minimale afstand tussen de oppervlakken juist vanwege de ruwheid niet gelijk aan nul is, maar aan de contact afstand. Dit is de maximale hoogte binnen een gegeven realisatie van een ruw oppervlak. Dit maximum maakt deel uit van de oneffenheden die aan een Gumbel-verdeling gefit kunnen worden. De waarde van deze belangrijke parameter ligt typisch tussen 3 en 5 maal de r.m.s. waarde, wat een Talyor-achtige expansie voor de overige oneffenheden mogelijk maakt. De verschuiving van de minimum afstand wegens ruwheid zorgt ook voor het singuliere gedrag van de Casimir-kracht nabij de contactafstand, dat ook experimenteel is waargenomen.

Dit model slaagt erin de metingen tussen ruwe goudlaagjes theoretisch te reproduceren. Dezelfde benadering met dezelfde ruwheidsstatistiek kan worden toegepast op de elektrostatische kracht. In dit geval is er een analoge Taylor-achtige benadering voor de oneffenheden die typisch binnen de r.m.s. waarde liggen. Op afstanden kleiner dan 100 nm blijkt de Casimir-kracht overeen te komen met een voltage van tussen de 0.2 V en 0.6 V.

Dit brengt ons tot het tweede onderwerp van dit proefschrift: de invloed van de Casimir-kracht op componenten van MEMS op korte afstanden. De actuatie-dynamica van een MEMS wordt gemodelleerd als een klassiek massa-veer systeem. De effectieve massa is onderhevig aan zowel de Casimir-kracht als aan de elekrostatische kracht. Dit klassieke

systeem wordt onderworpen aan een bifurcatie-analyse, met andere woorden er wordt onderzocht hoe de oplossingen van de bewegingsvergelijking kwalitatief afhangen van de waarden van de parameters. In eerste instantie wordt het conservatieve geval beschouwd. Het fenomeen stictie komt hierin overeen met de afwezigheid van periodieke oplossingen. Als de veerconstante groot genoeg is zijn er twee evenwichtspunten: een stabiel centrum en een onstabiel zadelpunt. Om het centrum-evenwicht bevinden zich periodieke oplossingen en kan stictie -met de juiste beginvoorwaarden - worden gemeden. Als echter de waarde van de veerconstante wordt verlaagd dan zullen het centrum en het zadelpunt in elkaar overgaan in een onstabiel centrum-zadel evenwicht. Ruwheid verhoogt de waarde van de veerconstante waarbij dat gebeurt. Bovendien verkleint ruwheid de afstand tussen het centrum en het zadelpunt. Hier staat tegenover dat ruwheid voorkomt dat de oppervlakken te dicht bij elkaar komen en dat de Casimir-kracht te groot wordt. Dit laatste wordt duidelijk als de elektrostatische kracht ook in beschouwing wordt genomen. Mochten de oppervlakken in contact komen, dan kan dit worden doorbroken met een externe belasting in de orde van enige nN.

Een conservatief MEM systeem is een eerste stap naar een realistischer scenario. De Melnikov methode introduceert bijvoorbeeld aandrijving en demping als storingen van een conservatief systeem. In 2001 werd al experimenteel aangetoond dat de gebruikelijke linearisatiebenadering van de Casimir-kracht faalt op afstanden kleiner dan 100 nm. Om de invloed van de Casimir-kracht op de actuatie-dynamica van MEMS op deze afstanden goed in te schatten, moet het volledige niet-lineaire probleem worden opgelost. Een aangedreven, gedempte oscillator met één of andere vorm van niet-lineariteit kan onder bepaalde omstandigheden chaotisch gedrag vertonen. Onder chaotisch gedrag wordt verstaan, dat de oplossingen van de bewegingsvergelijking gevoelig afhangen van de beginvoorwaarden. In termen van MEMS toepassingen betekent dit dat het moeilijker te bepalen is voor welke beginvoorwaarden er stictie of stabiele actuatie optreedt. Volgens de Melnikov methode is een vlak oppervlak gevoeliger voor chaotisch gedrag dan een ruw oppervlak. Dit is consistent met berekeningen van banen in de faseruimte voor relevante waarden van de parameters. De reden is dat de Casimir-kracht het niet-lineaire deel van de bewegingsvergelijking uitmaakt, en dat dit groter kan worden in het vlakke geval doordat ruwheid de minimale afstand verschuift.

Dankwoord

Firstly I would like to thank my supervisors Jasper Knoester and George Palasantzas. George, your enthusiasm has been inspirational and contagious. Moreover, you were always ready to help when needed. This thesis has been a collaboration between theorists and experimentalists. Such a thing would of course have been impossible without experimental input and motivation, and the measurements you performed together with Peter van Zwol. Furthermore I wish to thank you for introducing me to the fascinating field of dispersion forces and to the community of Casimir physicists.

Jasper, ondanks jouw drukke agenda als decaan van de faculteit heb je steeds de tijd kunnen vinden om met mij te praten. Dit heb ik altijd zeer gewaardeerd. Ondanks dat dit niet helemaal je vakgebied is, had je meestal aan een paar zinnen genoeg om er iets zinnigs over te zeggen of te vragen. Jouw scherpe en kritische blik heeft voortdurend bijgedragen aan onmisbare feedback.

Next my thanks go to my 'informal supervisor' Vitaly Svetovoy. Vitaly, while George's contribution represented the experimental viewpoint, yours has been on the theoretical side. For example, your knowledge of the Lifshitz theory has been invaluable for this project. Initially we were planning to tackle the roughness problem purely numerically. In retrospect that was never going to work. You came up with the idea to develop a model based the statistics of rough surfaces, which turned out to be very successful. Without this model, the second part of this thesis about the actuation dynamics of MEMS would not have been possible.

My gratitude also extends to Holger Waalkens. Holger, your input on nonlinear dynamics has been indispensable. Without this, the final chapter of this thesis would not have been possible.

I also gratefully acknowledge the members of the assessment committee, Hans de Raedt, Caspar van der Wal, and Stephan Scheel for spending their valuable time on reading this thesis. Linda en Niels, hartelijk dank dat jullie mij als paranimfen willen bijstaan.

Scientific endeavors cannot take place without an environment that offers pleasant interactions that are not research related. This is why I would like to thank the members of the

research group Theory of Condensed Matter, including but not limited to Erik Bloemsma, Niels van der Vegte, Thomas la Cour Jansen, Andrea Scaramucci, Robert Broos, Anna Stradomska-Szymczak, Niels Jelsma, Frank Haverkort, Victor Malyshev, Dennis Visser, Andrey Leonov, Chungwen Liang, Roel Tempelaar, Maxim Mostovoy, Jasper Compaijen, Santanu Roy, Sergey Artyukhin, Bas Vlaming, Ana Cunha, Alessio Pozzi, Kasper Duivenvoorden, Olexander Shvets, Bintoro Nugroho, Michiel van der Vegte, Tenzin Kunsel, and Arsalan Ghashghaaee. Ook wil ik hier de secretaresses Annlien Blanksma en Iris de Roo-Kwant bedanken. I also appreciate useful and pleasant discussions with Mehdi Sedighi, Bart Kooi, Gert ten Brink, Igor Hoveijn, Alef Sterk and Vladimir Krajñák. Mijn dank gaat hier in het bijzonder uit naar Bernhard Hoenders, die mij heeft geënthousiasmeerd voor de wetenschap.

Natuurlijk ben ik ook mijn ouders zeer erkentelijk voor hun financiële en morele steun. Daarzonder had dit project waarschijnlijk nooit kunnen plaatsvinden. Mijn vader heeft mij bovendien in contact gebracht met leden van zijn onderzoeksgroep, wat van groot belang is geweest voor het tweede deel van dit proefschrift.

Bibliography

Bibliography

[1] E. M. Lifshitz, "The theory of molecular attractive forces between solids", *Sov. Phys. JETP*, vol. 29, pp. 94–110, 1955.

[2] I. E. Dzyaloshinskii, E. M. Lifshitz, and L. P. Pitaevskii, "General theory of van der Waals' forces", *Adv. Phys.*, vol. 10, pp. 165–209, 1961.

[3] E. M. Lifshitz and L. P. Pitaevskii, *Statistical Physics Part 2*, vol. 9 of *Landau and Lifshitz Course of Theoretical Physics*, Butterworth-Heinemann, 1980.

[4] H. B. G. Casimir, "On the attraction between two perfectly conducting plates", *Proc. Kon. Nederland. Akad. Wetensch.*, vol. B51, pp. 793, 1948.

[5] J. N. Israelachvili, *Intermolecular and Surface Forces*, Elsevier, Amsterdam, 2011.

[6] F. London, "The general theory of molecular forces", *Trans. Faraday Soc.*, vol. 33, pp. 8b–26, 1937.

[7] J. Mahanty and B. W. Ninham, *Dispersion Forces (Colloid science)*, Academic Press Inc, 1977.

[8] V. Adrian Parsegian, *Van der Waals Forces*, Cambridge University Press, 2006.

[9] A. W. Rodriguez, F. Caspasso, and S. G. Johnson, "The Casimir effect in microstructured geometries", *Nat. Photon.*, vol. 5, pp. 211–221, 2011.

[10] A. Lambrecht, "The Casimir effect: a force from nothing.", *Phys. World*, vol. 15, pp. 29–32, Sept. 2002.

[11] M. Kardar and R. Golestanian, "The friction of vacuum, and other fluctuation-induced forces", *Rev. Mod. Phys.*, vol. 71, pp. 1233–1245, 1999.

[12] S. K. Lamoreaux, "The Casimir force: background, experiments, and applications.", *Rep. Prog. Phys.*, vol. 68, pp. 201–236, 2005.

[13] S. K. Lamoreaux, "Casimir forces: Still surprising after 60 years", *Phys. Today*, vol. 60, pp. 40–45, 2007.

[14] P. W. Milonni, *The Quantum Vacuum. An Introduction To Quantum Electrodynamics*, Academic Press Inc., 1994.

[15] K. A. Milton, *The Casimir Effect: Physical Manifestations of Zero-Point Energy.*, World Scientific, 2001.

[16] K. A. Milton, "The Casimir effect: recent controversies and progress", *J. Phys. A: Math. Gen.*, vol. 37, pp. R209, 2004.

[17] R. Onofrio, "Casimir forces and non-newtonian gravitation", *New J. Phys.*, vol. 8, pp. 237, 2006.

[18] G. Plunien, B. Muller, and W Greiner, "The Casimir effect.", *Phys. Rep.*, vol. 134, pp. 87–193, 1986.

[19] L. Spruch, "Long-range (Casimir) interactions", *Science*, vol. 272, pp. 1452–1455, 1996.

[20] Alejandro W. Rodriguez, J. D. Joannopoulos, and Steven G. Johnson, "Repulsive and attractive Casimir forces in a glide-symmetric geometry", *Phys. Rev. A*, vol. 77, pp. 062107, Jun 2008.

[21] M. Miri and R. Golestanian, "A frustrated nanomechanical device powered by the lateral Casimir force", *Appl. Phys. Lett.*, vol. 92, pp. 113103, 2008.

[22] C. Genet, A. Lambrecht, and S. Reynaud, "The Casimir effect in the nanoworld", *Eur. Phys. J. Spec. Top.*, vol. 160, pp. 183, 2008.

[23] G. Bressi, G. Carugno, R. Onofrio, and G. Ruoso, "Measurement of the Casimir force between parallel metallic surfaces", *Phys. Rev. Lett.*, vol. 88, no. 4, pp. 041804, Jan 2002.

[24] J. D. van der Waals, *Over de Continuïteit van den Gas- en Vloeistoftoestand*, PhD thesis, Universiteit Leiden, 1873.

[25] F. London, "Zur Theorie und Systematik der Molekularkräfte", *Z. Physik*, vol. 63, pp. 245, 1930.

[26] H. C. Hamaker, "The London-van der Waals attraction between spherical particles", *Physica*, vol. 4, pp. 1058, 1937.

[27] R. J. Hunter, *Foundations of colloid science*, Oxford University Press. Oxford; New York, 2001.

[28] J. H. de Boer, "The influence of van der Waals' forces and primary bonds on binding energy, strength and orientation, with special reference to some artificial resins", *Trans. Faraday Soc.*, vol. 32, pp. 10, 1936.

[29] R. Loudon, *The Quantum Theory of Light*, Oxford University Press, Oxford, UK, 2000.

[30] C. C. Gerry and P. L. Knight, *Introductory Quantum Optics*, Cambridge University Press, Cambridge, UK, 2005.

[31] H. B. G. Casimir and D. Polder, "The influence of retardation on the London-van der Waals forces", *Phys. Rev.*, vol. 73, pp. 360–372, 1948.

[32] M.J. Sparnaay, "Measurements of attractive forces between flat plates", *Physica*, vol. 24, no. 6-10, pp. 751 – 764, 1958.

[33] Peter H. G. M. van Blokland and J. Theodoor G. Overbeek, "van der Waals forces between objects covered with a chromium layer", *J. Chem. Soc., Faraday Trans. 1*, vol. 74, pp. 2637–2651, 1978.

[34] S. K. Lamoreaux, "Demonstration of the Casimir force in the 0.6 to 6 μm range", *Phys. Rev. Lett.*, vol. 78, pp. 5–8, 1997.

[35] Thomas Ederth, "Template-stripped gold surfaces with 0.4-nm rms roughness suitable for force measurements: Application to the Casimir force in the 20–100-nm range", *Phys. Rev. A*, vol. 62, no. 6, pp. 062104, Nov 2000.

[36] U. Mohideen and Anushree Roy, "Precision measurement of the Casimir force from 0.1 to 0.9μm", *Phys. Rev. Lett.*, vol. 81, pp. 4549–4552, Nov 1998.

[37] R. S. Decca, D. López, E. Fischbach, and D. E. Krause, "Measurement of the Casimir force between dissimilar metals", *Phys. Rev. Lett.*, vol. 91, pp. 050402, Jul 2003.

[38] H. B. Chan, V. A. Aksyuk, R. N. Kleiman, D. J. Bishop, and Federico Capasso, "Nonlinear micromechanical Casimir oscillator", *Phys. Rev. Lett.*, vol. 87, pp. 211801, Oct 2001.

[39] R. O. Behunin, F. Intravaia, D. A. R. Dalvit, P. A. Maia Neto, and S. Reynaud, "Modeling electrostatic patch effects in Casimir force measurements", *Phys. Rev. A*, vol. 85, pp. 012504, Jan 2012.

[40] Ronald J. Adler, Brendan Casey, and Ovid C. Jacob, "Vacuum catastrophe: An elementary exposition of the cosmological constant problem", *Am. J. Phys.*, vol. 63, pp. 620, 1995.

[41] Julian Schwinger, Lester L DeRaad Jr., and Kimball A Milton, "Casimir effect in dielectrics", *Annals of Physics*, vol. 115, no. 1, pp. 1 – 23, 1978.

[42] R. L. Jaffe, "Casimir effect and the quantum vacuum", *Phys. Rev. D*, vol. 72, pp. 021301, Jul 2005.

[43] R. Maboudian and R. T. Howe, "Critical review: Adhesion in surface micromechanical structures", *J. Vac. Sci. Technol. B*, vol. 15, pp. 1, 1997.

[44] P Ball, "Fundamental physics: Feel the force.", *Nature*, vol. 447, pp. 772–774, 2007.

[45] F. Capasso, J.N. Munday, D. Iannuzzi, and H.B. Chan, "Casimir forces and quantum electrodynamical torques: Physics and nanomechanics", *Selected Topics in Quantum Electronics, IEEE Journal of*, vol. 13, no. 2, pp. 400 –414, march-april 2007.

[46] G. Palasantzas and J. Th. M. DeHosson, "Phase maps of microelectromechanical switches in the presence of electrostatic and Casimir forces", *Phys. Rev. B*, vol. 72, pp. 121409, Sep 2005.

[47] G. Palasantzas and J. Th. M. De Hosson, "Pull-in characteristics of electromechanical switches in the presence of Casimir forces: Influence of self-affine surface roughness", *Phys. Rev. B*, vol. 72, pp. 115426, Sep 2005.

[48] E. Buks and M. L. Roukes, "Metastability and the Casimir effect in micromechanical systems", *Europhys. Lett.*, vol. 54, no. 2, pp. 220, 2001.

[49] F. Michael Serry, Dirk Walliser, and G. Jordan Maclay, "The role of the Casimir effect in the static deflection and stiction of membrane strips in microelectromechanical systems (MEMS)", *J. Appl. Phys*, vol. 84, pp. 2501, 1998.

[50] F. Michael Serry, Dirk Walliser, and G. Jordan Maclay, "The anharmonic Casimir oscillator - the Casimir effect in a model microelectromechanical system", *J. Microelec. Sys.*, vol. 4, pp. 193–205, 1995.

[51] F. W. DelRio, M. P. de Boer, J. A. Knapp, E. D. Reedy Jr., P. J. Clews, and M. L. Dunn, "The role of van der Waals forces in adhesion of micromachined surfaces", *Nature Mater.*, vol. 4, pp. 629, 2005.

[52] P. M. Osterberg, *Electrostatically actuated micromechanical test structures for material property measurement*, PhD thesis, MIT, Cambridge, MA, 1995.

[53] Ofir Bochobza-Degani and Yael Nemirovsky, "Modeling the pull-in parameters of electrostatic actuators with a novel lumped two degrees of freedom pull-in model", *Sensors and Actuators A: Physical*, vol. 97-98, no. 0, pp. 569 – 578, 2002, Selected papers from Eurosenors XV.

[54] Ofir Bochobza-Degani, Eran Socher, and Yael Nemirovsky, "On the effect of residual charges on the pull-in parameters of electrostatic actuators", *Sensors and Actuators A: Physical*, vol. 97, no. 0, pp. 563, 2002, Selected papers from Eurosenors XV.

[55] L. X. Zhang, J. W. Zhang, Y. P. Zhao, and T. X. Yu, "Failure modes of doubly supported capacitive RF MEMS switches", *Int. J. Nonlinear Sci. Numer. Simul.*, vol. 3-4, pp. 353–356, 2002.

[56] W. H. Lin and Y. P. Zhao, "Dynamics behaviour of nanoscale electrostatic actuators", *Chin. Phys. Lett.*, vol. 20, no. 11, pp. 2070, 2003.

[57] R Esquivel-Sirvent, L Reyes, and J Bárcenas, "Stability and the proximity theorem in Casimir actuated nano devices", *New Journal of Physics*, vol. 8, no. 10, pp. 241, 2006.

[58] R Esquivel-Sirvent, M A Palomino-Ovando, and G H Cocoletzi, "Pull-in control due to Casimir forces using external magnetic fields", *Appl. Phys. Lett.*, vol. 95, pp. 051909, 2009.

[59] W. H. Lin and Y. P. Zhao, "Nonlinear behavior for nanoscale electrostatic actuators with Casimir force", *Chaos, Solitons and Fractals*, vol. 23, pp. 1777, 2005.

[60] W. H. Lin and Y. P. Zhao, "Casimir effect on the pull-in parameters of nanometer switches", *Microsystem Technologies*, vol. 11, pp. 80, 2005.

[61] John A. Pelesko and David H. Bernstein, *Modeling MEMS and NEMS*, Chapman & Hall/CRC, Boca Raton, FL, 2003.

[62] Jan Haisma, Nico Hattu, J. T. C. M. Pulles, Esther Steding, and Jan C. G. Vervest, "Direct bonding and beyond", *Appl. Opt.*, vol. 47, pp. 6793–6803, 2007.

[63] A. K. Geim, S. V. Dubonos, I. V. Grigorieva, K. S. Novoselov, A. A. Zhukov, and S. Yu. Shapoval, "Microfabricated adhesive mimicking gecko foot-hair", *Nature Materials*, vol. 2, pp. 461 – 463, 2003.

[64] G. Torricelli, P. J. van Zwol, O. Shpak, C. Binns, G. Palasantzas, B. J. Kooi, V. B. Svetovoy, and M. Wuttig, "Switching Casimir forces with phase-change materials", *Phys. Rev. A*, vol. 82, pp. 010101, Jul 2010.

[65] Y.-P. Zhao, G.-C. Wang, T.-M. Lu, G. Palasantzas, and J. Th. M. De Hosson, "Surface-roughness effect on capacitance and leakage current of an insulating film", *Phys. Rev. B*, vol. 60, pp. 9157 – 9164, Sep 1999.

[66] R. Esquivel-Sirvent and R. Pérez-Pascual, "Geometry and charge carrier induced stability in Casimir actuated nanodevices", *Eur. Phys. J. B*, vol. 86, pp. 467, 2013.

[67] P. J. van Zwol, G. Palasantzas, and J. Th. M. De Hosson, "Influence of random roughness on the Casimir force at small separations", *Phys. Rev. B*, vol. 77, no. 7, pp. 075412, Feb 2008.

[68] C. Genet, S. Reynaud, and A Lambrecht, "The Casimir force between rough metallic plates", *Europhys. Lett.*, vol. 62, pp. 484, 2003.

[69] Paulo A. Maia Neto, Astrid Lambrecht, and Serge Reynaud, "Casimir effect with rough metallic mirrors", *Phys. Rev. A*, vol. 72, no. 1, pp. 012115, Jul 2005.

[70] S. M. Rytov, Y. A. Kravtsov, and V. I. Tatarskii, *Principles of Statistical Radiophysics, Vol. 3: Elements of Random Fields.*, Springer, Berlin, 1989.

[71] Alejandro Rodriguez, Mihai Ibanescu, Davide Iannuzzi, Federico Capasso, J. D. Joannopoulos, and Steven G. Johnson, "Computation and visualization of Casimir forces in arbitrary geometries: Nonmonotonic lateral-wall forces and the failure of proximity-force approximations", *Phys. Rev. Lett.*, vol. 99, no. 8, pp. 080401, Aug 2007.

[72] H. B. Callen and T. A. Welton, "Irreversibility and generalized noise", *Phys. Rev.*, vol. 83, pp. 34, 1951.

[73] L. D. Landau and E. M. Lifshitz, *Statistical Physics, Part 1*, Butterworth-Heinemann, 3rd. edition, 1980.

[74] Mauro Antezza, Lev P. Pitaevskii, Sandro Stringari, and Vitaly B. Svetovoy, "Casimir-Lifshitz force out of thermal equilibrium", *Phys. Rev. A*, vol. 77, pp. 022901, 2008.

[75] G. S. Agarwal, "Quantum electrodynamics in the presence of dielectrics and conductors. I. electromagnetic-field response functions and black-body fluctuations in finite geometries", *Phys. Rev. A*, vol. 11, pp. 230, 1975.

[76] W. Eckhardt, "Macroscopic theory of electromagnetic fluctuations and stationary radiative heat transfer", *Phys. Rev. A*, vol. 29, pp. 1991, 1984.

[77] Robert N. C. Pfeifer, Timo A. Nieminen, Norman R. Heckenberg, and Halina Rubinsztein-Dunlop, "Momentum of an electromagnetic wave in dielectric media", *Rev. Mod. Phys.*, vol. 79(4), pp. 1197–1216, 2007.

[78] John David Jackson, *Classical Electrodynamics*, John Wiley & Sons, Inc. Hoboken NJ, third edition, 1999.

[79] L. P. Pitaevskii, "On the problem of van der Waals forces in dielectric media", in *"Casimir Physics", Lecture Notes in Physics Series*. Springer, 2010.

[80] M. S. Tomaš, "Casimir force in absorbing multilayers", *Phys. Rev. A*, vol. 66, pp. 052103, Nov 2002.

[81] Antoine Canaguier-Durand, Paulo A. Maia Neto, Ines Cavero-Pelaez, Astrid Lambrecht, and Serge Reynaud, "Casimir interaction between plane and spherical metallic surfaces", *Phys. Rev. Lett.*, vol. 102, no. 23, pp. 230404, Jun 2009.

[82] V. B. Svetovoy and R. Esquivel, "Nonlocal impedances and the Casimir entropy at low temperatures", *Phys. Rev. E*, vol. 72, pp. 036113, Sep 2005.

[83] V B Svetovoy and R Esquivel, "The Casimir free energy in high- and low-temperature limits", *Journal of Physics A: Mathematical and General*, vol. 39, no. 21, pp. 6777, 2006.

[84] Giuseppe Bimonte, "Bohr-van Leeuwen theorem and the thermal Casimir effect for conductors", *Phys. Rev. A*, vol. 79, pp. 042107, Apr 2009.

[85] J. M. Obrecht, R. J. Wild, M. Antezza, L. P. Pitaevskii, S. Stringari, and E. A. Cornell, "Measurement of the temperature dependence of the Casimir-Polder force", *Phys. Rev. Lett.*, vol. 98, pp. 063201, Feb 2007.

[86] Mauro Antezza, Lev P. Pitaevskii, and Sandro Stringari, "Effect of the Casimir-Polder force on the collective oscillations of a trapped Bose-Einstein condensate", *Phys. Rev. A*, vol. 70, pp. 053619, Nov 2004.

[87] D. M. Harber, J. M. Obrecht, J. M. McGuirk, and E. A. Cornell, "Measurement of the Casimir-Polder force through center-of-mass oscillations of a Bose-Einstein condensate", *Phys. Rev. A*, vol. 72, pp. 033610, Sep 2005.

[88] A. O. Sushkov, W. J. Kim, D. A. R. Dalvit, and S. K. Lamoreaux, "Observation of the thermal Casimir force", *Nature Physics*, vol. 7, pp. 230–233, 2011.

[89] G. Palasantzas, V. B. Svetovoy, and P. J. van Zwol, "Influence of ultrathin water layer on the van der Waals/Casimir force between gold surfaces", *Phys. Rev. B*, vol. 79, pp. 235434, Jun 2009.

[90] A Lambrecht and S. Reynaud, "Casimir force between metallic mirrors", *Eur. Phys. J. D*, vol. 8, pp. 309, 2000.

[91] M.S. Tomaš, "Casimir force between dispersive magnetodielectrics", *Physics Letters A*, vol. 342, no. 56, pp. 381 – 388, 2005.

[92] C. Henkel and K. Joulain, "Casimir force between designed materials: What is possible and what not", *EPL (Europhysics Letters)*, vol. 72, no. 6, pp. 929, 2005.

[93] F. S. S. Rosa, D. A. R. Dalvit, and P. W. Milonni, "Casimir-Lifshitz theory and metamaterials", *Phys. Rev. Lett.*, vol. 100, pp. 183602, May 2008.

[94] Pablo Rodriguez-Lopez, "Casimir repulsion between topological insulators in the diluted regime", *Phys. Rev. B*, vol. 84, pp. 165409, Oct 2011.

[95] J. van Bree, J. Poulis, B. Verhaar, and K. Schram, "The influence of surface irregularities upon the van der Waals forces between macroscopic bodies", *Physica (Amsterdam)*, vol. 78, no. 1, pp. 187–190, 1974.

[96] B. V. Derjaguin, "Untersuchungen über die Reibung und Adhäsion", *Kolloid Z.*, vol. 69, pp. 155, 1934.

[97] G. L. Klimchitskaya and Y. V. Pavlov, "The corrections to the Casimir forces for configurations used in experiments: The spherical lens above the plane and two crossed cylinders", *Int. J. Mod. Phys. A*, vol. 11, pp. 3723–3742, 1996.

[98] P. J. van Zwol, V. B. Svetovoy, and G. Palasantzas, "Distance upon contact: Determination from roughness profile", *Phys. Rev. B*, vol. 80, no. 23, pp. 235401, Dec 2009.

[99] V. B. Svetovoy, P. J. van Zwol, G. Palasantzas, and J. Th. M. De Hosson, "Optical properties of gold films and the Casimir force", *Phys. Rev. B*, vol. 77, no. 3, pp. 035439, Jan 2008.

[100] G. Palasantzas, V. B. Svetovoy, and P. J. van Zwol, "Optical properties and kinetic roughening influence on dispersive Casimir and van der Waals forces", *Int. J. Mod. Phys. B*, vol. 24, pp. 6023, 2010.

[101] E. J. Gumbel, *Statistics of Extremes*, Dover Publications Inc., 2004.

[102] Wijnand Broer, George Palasantzas, Jasper Knoester, and Vitaly B. Svetovoy, "Roughness correction to the Casimir force beyond perturbation theory", *EPL (Europhys. Lett.)*, vol. 95, no. 3, pp. 30001, 2011.

[103] Allen Taflove and Susan C. Hagness, *Computational Electrodynamics: The Finite-Difference Time-Domain Method*, Artech House London and Boston, 2005.

[104] Ardavan F. Oskooi, David Roundy, Mihai Ibanescu, Peter Bermel, J. D. Joannopoulos, and Steven G. Johnson, "MEEP: A flexible free-software package for electromagnetic simulations by the FDTD method", *Comp. Phys. Comm.*, vol. 181, pp. 687–702, January 2010.

[105] Alejandro W. Rodriguez, Alexander P. McCauley, John D. Joannopoulos, and Steven G. Johnson, "Casimir forces in the time domain: Theory", *Phys. Rev. A*, vol. 80, no. 1, pp. 012115, Jul 2009.

[106] Alexander P. McCauley, Alejandro W. Rodriguez, John D. Joannopoulos, and Steven G. Johnson, "Casimir forces in the time domain: Applications", *Phys. Rev. A*, vol. 81, no. 1, pp. 012119, Jan 2010.

[107] Cyriaque Genet, Astrid Lambrecht, and Serge Reynaud, "Temperature dependence of the Casimir effect between metallic mirrors", *Phys. Rev. A*, vol. 62, no. 1, pp. 012110, Jun 2000.

[108] A. Canaguier-Durand, *Multipolar scattering expansion for the Casimir effect in the plane-sphere geometry*, PhD thesis, Labaratoire Kastler Brossel, 2011.

[109] John D. Joannopoulos, Steven G. Johnson, Joshua N. Winn, and Robert D. Meade, *Photonic Crystals: Molding the Flow of Light*, Princeton University Press, 2008.

[110] J. Haisma and G. A. C. M. Spierings, "Surface-related phenomena in the direct bonding of silicon and fused-silica wafer pairs", *Philips J. Res*, vol. 49, pp. 47 –63, 1995.

[111] G. Palasantzas, P. J. van Zwol, and J. T. M. de Hosson, "Transition from Casimir to van der Waals force between macroscopic bodies", *Appl. Phys. Lett.*, vol. 93, pp. 121912, 2008.

[112] H. B. Chan, Y. Bao, J. Zou, R. A. Cirelli, F. Klemens, W. M. Mansfield, and C. S. Pai, "Measurement of the Casimir force between a gold sphere and a silicon surface with nanoscale trench arrays", *Phys. Rev. Lett.*, vol. 101, no. 3, pp. 030401, Jul 2008.

[113] E. Buks and M. L. Roukes, "Stiction, adhesion energy, and the Casimir effect in micromechanical systems", *Phys. Rev. B*, vol. 63, no. 3, pp. 033402, Jan 2001.

[114] Gauthier Torricelli, Peter J. van Zwol, Olex Shpak, George Palasantzas, Vitaly B. Svetovoy, Chris Binns, Bart J. Kooi, Peter Jost, and Matthias Wuttig, "Casimir force contrast between amorphous and crystalline phases of AIST", *Adv. Funct. Mater.*, 2012.

[115] Wijnand Broer, George Palasantzas, Jasper Knoester, and Vitaly B. Svetovoy, "Roughness correction to the Casimir force at short separations: Contact distance and extreme value statistics", *Phys. Rev. B*, vol. 85, pp. 155410, Apr 2012.

[116] P. Lu and S. J. O Shea, "Mechanical contact between rough surfaces at low load", *J. Phys. D: Appl. Phys.*, vol. 45, pp. 475303, 2012.

[117] George Palasantzas, "Roughness spectrum and surface width of self-affine fractal surfaces via the k-correlation model", *Phys. Rev. B*, vol. 48, pp. 14472–14478, Nov 1993.

[118] R. O. Behunin, Y. Zeng, D. A. R. Dalvit, and S. Reynaud, "Electrostatic patch effects in Casimir-force experiments performed in the sphere-plane geometry", *Phys. Rev. A*, vol. 86, pp. 052509, Nov 2012.

[119] Ricardo García and Rubén Peréz, "Dynamic atomic force microscopy methods", *Surf. Sci. Rep.*, vol. 47, pp. 197–301, 2002.

[120] Morris W. Hirsch, Stephen Smale, and Robert L. Devaney, *Differential Equations, Dynamical Systems, and an Introduction to Chaos*, Elsevier Academic Press, San Diego (CA), 2004.

[121] Heinz Hanßmann, *Local and Semi-Local Bifurcations in Hamiltonian Dynamical Systems*, Springer, Berlin Heidelberg, 2007.

[122] M. Sedighi, W. H. Broer, G. Palasantzas, and B. J. Kooi, "Sensitivity of micromechanical actuation on amorphous to crystalline phase transformations under the influence of Casimir forces", *Phys. Rev. B*, vol. 88, pp. 165423, Oct 2013.

[123] Elmar Bonaccurso, Hans-Jürgen Butt, and Vincent S. J. Craig, "Surface roughness and hydrodynamic boundary slip of a newtonian fluid in a completely wetting system", *Phys. Rev. Lett.*, vol. 90, pp. 144501, Apr 2003.

[124] Olga I. Vinogradova and Gleb E. Yakubov, "Dynamic effects on force measurements. 2. lubrication and the atomicforce microscope", *Langmuir*, vol. 19, no. 4, pp. 1227–1234, 2003.

[125] Olga I. Vinogradova and Gleb E. Yakubov, "Surface roughness and hydrodynamic boundary conditions", *Phys. Rev. E*, vol. 73, pp. 045302, Apr 2006.

[126] R.S. Decca, D. Lopez, E. Fischbach, G.L. Klimchitskaya, D.E. Krause, and V.M. Mostepanenko, "Precise comparison of theory and new experiment for the Casimir force leads to stronger constraints on thermal quantum effects and long-range interactions", *Ann. Phys. (NY)*, vol. 318, no. 1, pp. 37 – 80, 2005.

[127] Wijnand Broer, George Palasantzas, Jasper Knoester, and Vitaly B. Svetovoy, "Significance of the Casimir force and surface roughness for actuation dynamics of MEMS", *Phys. Rev. B*, vol. 87, pp. 125413, Mar 2013.

[128] T. Emig, "Casimir-force-driven ratchets", *Phys. Rev. Lett.*, vol. 98, pp. 160801, Apr 2007.

[129] Michele Bonnin, "Horseshoe chaos and subharmonic orbits in the nanoelectromechanical Casimir nonlinear oscillator", *International Journal of Circuit Theory and Applications*, vol. 41, no. 6, pp. 583–602, 2013.

[130] John Guckenheimer and Philip Holmes, *Nonlinear Oscillations, Dynamical Systems, and Bifurcations of Vector Fields*, Springer-Verlag New York Berlin Heidelberg Tokyo, 1986.

[131] Henk W. Broer and Bernd Krauskopf, "Chaos in periodically driven systems", *AIP Conference Proceedings*, vol. 548, no. 1, pp. 31–53, 2000.

[132] F. H. Ling, "A numerical study of the applicability of Melnikov's method", *Phys. Lett. A*, vol. 9, pp. 447, 1987.

[133] F. H. Ling and G. W. Bao, "A numerical implementation of Melnikov's method", *Phys. Lett. A*, vol. 122, no. 8, pp. 413–417, 1987.

[134] Sriharsha V. Aradhya, Michael Frei, Mark S. Hybertsen, and L. Venkataraman, "Van der Waals interactions at metal/organic interfaces at the single-molecule level", *Nat Mater*, vol. 11, pp. 872, 2012.

[135] F. W. DelRio, M. L. Dunn, L. M. Phinney, C. J. Bourdon, and M. P. de Boer, "Rough surface adhesion in the presence of capillary condensation", *Appl. Phys. Lett.*, vol. 90, pp. 163104, 2007.

[136] B. N. J. Persson, "Capillary adhesion between elastic solids with randomly rough surfaces", *J. Phys.: Condens. Matter*, vol. 20, no. 315007, 2008.

[137] P. J. van Zwol, G. Palasantzas, and J. Th. M. De Hosson, "Influence of roughness on capillary forces between hydrophilic surfaces", *Phys. Rev. E*, vol. 78, no. 3, pp. 031606, Sep 2008.

[138] H. W. Broer and F. Takens, *Dynamical systems and Chaos*, Epsilon Uitgaven, Utrecht, 2009.

[139] William H. Press, Saul A. Teukolsky, William T. Vetterling, and Brian P. Flannery, *Numerical Recipes*, Cambridge University Press, third edition, 2007.